THE EFFECT OF CGI MICROSTRUCTURE ON FRACTURE AND MACHINING

THE EFFECT OF COMPACTED GRAPHITE IRON MICROSTRUCTURE ON FRACTURE AND MACHINING

By

WALID M. MOHAMMED EL SABAGH

Submitted to the School of Graduate Studies in Partial Fulfillment

of the Requirements for the Degree of

Doctor of Philosophy

DOCTOR OF PHILOSOPHY — McMaster University

(Mechanical Engineering) — Hamilton, Ontario

TITLE:	THE EFFECT OF COMPACTED GRAPHITE IRON MICROSTRUCTURE ON FRACTURE AND MACHINING
AUTHOR:	WALID M. MOHAMMED EL SABAGH
SUPERVISOR:	PROF. MOHAMED ABDEL AZIZ ELBESTAWI, P.ENG
CO-SUPERVISOR:	Dr. Eu-Gene NG
NUMBER OF PAGES:	xix, 202

Abstract

Cast irons are characterized by their wide range of achievable mechanical and physical properties, in addition to their competitive prices compared to other materials in most industries. Cast irons, in general, consist of an iron matrix (pearlite, ferrite, austenite, etc.) and graphite, as well as smaller percentages of other additives. The morphology of graphite whether it is flaky, compact, or nodular, has a significant impact on the mechanical (and physical) properties of cast iron.

The graphite structure in compacted graphite iron (CGI) is more coral-like and interconnected only within each eutectic cell. The irregular surface of the graphite-matrix interface has blunt edges which results in the intimate adhesion of the graphite particles to the metal matrix producing more resistance to crack initiation and more vermicular paths arrest crack propagation. Furthermore, the coral-like graphite particles, which are characterized with round edges, also do not promote crack propagation and serve as crack arrestors once cracks are initiated. This unique morphology of graphite in CGI, thereafter, pays off in a higher tensile strength and modulus of elasticity while possessing reasonable thermal conductivity. This useful combination of double the ultimate strength, reasonable thermal conductivity, high modulus of elasticity, and superior crack initiation/propagation resistance in CGI as compared to gray cast iron (GCI), as well as the greater resistance to distortion and better thermal conductivity as compared to ductile (nodular) cast iron (SGI), all result in a valuable overall performance.

However, the same mechanical properties of compacted graphite iron (CGI) that

contribute to higher performance than gray iron and aluminum alloys that are currently used in automotive and locomotive industries, make it relatively difficult to machine. Current approaches to deal with the relatively poor machinability of CGI have led to significant compromises. Despite the many efforts to improve the machinability of CGI at a practical level, it is evident that much work needs to be invested to reach current production and cost targets based on operations using gray cast iron.

This work is divided into two phases. The first phase establishes a foundation of a microstructure modeling technique which will be then applied to model CGI in machining. Modeling is being done to shift the approach away from trial and error as is currently being done to a more physics based approach. As machining is conceptually a controlled fracture process, this stage comprehensively studies and models the initiation and propagation of fracture in compacted graphite iron.

Very little research to date has been directed to the study of CGI's mechanics under different loading scenarios. The absence of a comprehensive foundation to assist with the understanding of CGI's mechanics under different loading scenarios motivates the initiation of this phase. One effective methodology to establish this comprehensive foundation is by utilizing the finite element method approach that is validated by metallurgical investigations. Most crack initiation and propagation investigations are performed as after-the-event procedures, thus the application of finite element method makes it possible to better understand the effect of graphite morphology on crack initiation and propagation. In addition, the finite element modeling of CGI crack initiation and propagation can exclude most of the complex interacting variables to make it possible

to understand the inherently complex fracture phenomena which take place during machining.

The second phase serves as an application of the previously built model to capture the more complex scenario involving machining of CGI at different cutting speeds and feeds. The finite element modeling of CGI in machining provides an as of yet unavailable procedure on which future optimization techniques can be performed. The study of chip formation, cutting insert wear, and force measurements are performed in parallel with the modeling process and are employed as means to validate the FE model. Validation of both work phases has been completed to support the model developed in this thesis that captures the critical aspects of machining CGI under different operating scenarios.

Acknowledgements

I would like to express my sincere indebtedness to my supervisor Dr. M.A. Elbestawi. I cannot find the adequate words to express my appreciation to his continuous guidance, support, and encouragement since the first day. I will always be grateful to the man who made all this work possible (and worth doing). Thank you Dr. Elbestawi.

I would like to thank Dr. Ng for his endless support and guidance. Dr. Ng's endless "*brain-poking*" remarks surely stimulated my creativity and perseverance during the progress of this work. Special thanks to my committee members; Dr. Stephen Veldhuis, Dr. Philip Koshy, and Dr. Hatem Zurob, for their helpful comments and discussions throughout the progress of this work. Their comments have enriched my work and made it more meaningful.

I would like to acknowledge the financial support from NSERC – Canadian Network for Research and Innovation in Machining Technology (CANRIMT).

Many thanks to the Mechanical Engineering and MMRI workshops team; Mr. R. Lodewyks, Mr. Mark Mackenzie, Mr. Jim McLaren, Mr. J.P. Talon, and Mr. Terry Wagg. You were always available to help me during my experimental work.

Special thanks to my wonderful wife; Fadua, for her unconditional love, support, and incredible patience during the course of this work. Together we will achieve all we always dreamed of. My special thanks to my delightful creative "*buddy*"; Mostafa, and my little intelligent twin daughters, Noura and Youmna for their love and support. You always inspire me to continue.

Dedications

To my ever living wonderful memory, the memory of my father, I have fulfilled my promise. To my mother, to whom I owe my existence.

To my unconditionally supportive beloved wife, *Fadua*, without you this would have never been achieved. I owe you my success.

To my lovely kids, Mostafa, Noura, and Youmna, you are the light of my sight.

"رب أوزعنى أن أشكر نعمتك التى أنعمت علي وعلى والدي وأن أعمل صالحا ترضاه وأدخلنى برحمتك فى عبادك الصالحين"

Contents

List of Figures

List of Tables

List of Symbols

R_m	Tensile strength
K_a	The graphite shape calculated as ratio of tensile strength to hardness
G	Amount of eutectic graphite
CE	Carbon equivalent
D	Damage criterion
D_c	Critical damage criterion (scalar)
$\varepsilon^f, \varepsilon_f$	General fracture strain, Johnson-Cook fracture strain
σ_i	Principal stress in the i_{th} direction
σ_m, σ_{eq}	Hydrostatic stress, von Mises equivalent stress
T_n, T_t	Interface normal and tangential traction components
u_n, u_t	Interface normal and tangential displacement components
δ_{max}, δ_f	Maximum traction displacement
$\delta_{init}, \delta_{eff}$	Interface fracture initiation displacement, effective interface displacement
A,B,C,n,m	Johnson-Cook material constants
$d_1..d_5$	Johnson-Cook material damage constants

CHAPTER 1 INTRODUCTION

1.1 Motivation

The effect of the CGI microstructure on fracture and machining, in particular, is the main aim of the current work. For the last few decades, most of the industry resources have been exclusively dedicated to improving the production of compacted graphite iron to achieve commercial high volume production quality. Surprisingly, little effort has been devoted to produce a comprehensive study of the effect of the microstructure of CGI on fracture and machining to date.

The superior performance of CGI makes it as a promising alternative to commonly used materials like gray iron and aluminum alloys. CGI has proven to better withstand fracture and maintain reasonable strength at elevated temperature and provide pressure limits in engine applications which exceed the range achievable using gray iron and aluminum alloys. Due to CGI's superior performance in automotive and locomotive industries, most relevant manufacturers have considered it to be an attractive material in such fields. The only hindering factor to more broadly using CGI in industry is its relatively poor machinability as compared to gray iron and aluminum alloys. In pursuit of a solution to CGI's poor machinability, most efforts to date have been limited to iterative trials and documentation of observations without a deep understanding of the underlying material-related mechanisms which drive such observations. Some researchers have tried complicated multi-insert tool configurations [1], the use of LASER to assist machining [2], and chemically based machining solutions [3].

The current work furnishes a scientifically based foundation to study the superior properties of CGI. Since CGI will be functioning as a substitutive production material, its performance in service should be understood. In addition, to efficiently produce an alternative new material at a comparative cost, machining of CGI should, as well, be understood. Therefore, both the fracture properties and machining performance of compacted graphite iron should be comprehensively studied.

In light of the aforementioned, the motivations of the current work can be briefly listed as follows:

1. Compacted graphite iron possesses superior performance in many applications due to its unique graphite morphology.
2. The lack of a comprehensive understanding of the role of the microstructure of compacted graphite iron in establishing it characteristic superior performance and its limited machinability.
3. Difficulties and enormous costs associated with experimental and analytical methods required to better understand CGI material performance and to pursue a solution to its relatively poor machinability.
4. The advantage in terms of cost and resources associated with the numerical modeling and simulation of material mechanical-physical behaviors. This is made possible due to the enormous development in digital resources and reasonably sufficient physical-mathematical models necessary to describe some critical aspects of the behavior of CGI.
5. Establishment of a modeling technique which will include the microstructure

aspects CGI, and can be adopted for the modeling and simulation of other similar materials at reasonable accuracy.

6. No academic/industrial publication, to date, could comprehensively explain the effect of the microstructure of compacted graphite iron on fracture and machining despite the promising performance of the material to date.

1.2 Scope of the Current Work

The scope of the current work is to develop a finite element model which can be applied to multi-constituent materials considering the effect of their microstructures on performance. As the overall performance of a multi-constituent material is contingent upon the inter-constituent reactions, the current work introduces the newly developed numerical technique; cohesive zone elements, to account for the two intimately interacting phases associated with the matrix and graphite interface decohesion. The introduction of the cohesive zone elements technique is based on mathematical and physical foundations [4]. Metallurgical investigations of the decohesion phenomenon have been performed to accurately implement such decohesion criterion. The current work has chosen compacted graphite iron as an application material to the proposed model for a number of reasons; 1) compacted graphite iron, despite its promising performance in industry, has significantly lacked a comprehensive study to adequately explain its superior performance, 2) compacted graphite iron represents a challenging application to the proposed model due to its complex microstructure, and 3) the study of compacted graphite iron will positively impact industry leading to improved engine performance and fuel economy.

From there, two important venues have been studied in the current work, namely; fracture and machining. The importance of studying fracture of compacted graphite iron is to understand the behavior, capabilities, and limitations of CGI if adopted as a new material for a challenging application. The study of compacted graphite iron machining is crucial to the application of the already existing technology to minimize future new material manufacturing costs and configuration.

1.3 Thesis Outline

This thesis is comprised of eight chapters, from which the current chapter presents the motivations, scope of current work, and a general outline of the thesis contents. As compacted graphite iron is considered for its advantageous properties compared to gray and ductile irons, chapter (2) presents an essential overview of the properties of the three related cast irons with a detailed overview of compacted graphite iron properties, production techniques, and relevant topics. In addition, a brief overview on the graphite growth mechanism is provided to highlight the role of compacted graphite structure on CGI's unique properties.

Chapter (3) is part of the literature review providing an overview on the machining of compacted graphite iron challenges and deficiencies. This chapter discusses the recent works performed in pursuit of an improved process for machining compacted graphite iron. Since the major bulk of research performed to date is limited to experimentation with different cutting tools and documentation of the observed findings without deep elaboration on the underlying factors, the chapter focuses on these findings. The only

exception is with the work performed by Dr. Dawson [1] which provides a relatively interesting study of CGI's machinability.

Chapter (4) complements the literature review and briefly covers the different methods used to model metal cutting. In addition, chapter (4) highlights the different chip formation types and techniques, in real machining and in numerical techniques furnishing a foundation to the main contributions outlined in this thesis.

Chapter (5) stands as the theoretical core of the present work. It comprehensively describes the proposed modeling technique of compacted graphite iron microstructure. The chapter explains the proposed technique and briefly includes the complementing experimental procedures relevant to the specific topic. In this chapter, the experimental procedures are kept to the minimum in order to adequately emphasize the theory part in the current work. The majority of the Abaqus finite element terms are present in other commonly used preprocessing/processing finite element packages.

Chapter (6) provides a comprehensive description to the experimental work done throughout the course of the current work. Material testing, metallurgical investigation, and machining procedures are all presented for the purpose of replication and/or continuation.

Chapter (7) presents the results of the current work accompanied by the author's discussion and reasoning. The chapter presents the fracture tests and simulation results as well as the machining tests and simulation results. Validation of both models and a discussion of the relevant findings are presented.

Chapter (8) concludes the present work drawn from the experimental and simulated results in addition to all relevant findings. The chapter explicitly lists the major contributions of the current work and future work recommendations.

CHAPTER 2

Literature Review

2.1 Introduction

Cast iron is one of the most important materials in industry worldwide. Out of the total world tonnage of castings produced, about 70% are made out of various types of cast irons [5]. This is attributed to cast iron's versatile achievable mechanical and thermal properties with its competitive prices. Cast iron can be defined as a Fe–C alloy. The three basic constituents of cast irons can be primarily identified as Iron with 2-4 wt-% Carbon (in the form of either graphite or carbide), and a percentage ranging from 1 to 3% of Silicon [6]. Variation of the percentage of the three main constituents, in addition to melting temperature, casting procedure, and heat treatment, are the key elements associated with changing the properties of cast iron.

2.2 Cast Irons

Classification of the different types of cast irons can be based on different criteria. Historically, the first classification of cast irons was based on its fracture characteristics. Two types of irons were initially classified; *White iron*, which exhibits a "white", crystalline fracture surface as fracture occurs along the iron carbide plates, and *Gray iron*, which exhibits a gray surface due to the occurrence of fracture in the embedded graphite phase in the metal matrix. A more recent classification is based on the microstructural

features of cast irons. One classifies cast irons based on the graphite morphology present in the matrix; lamellar (*flake*) graphite iron (FGI), spheroid (*nodular*) graphite iron (SGI), compacted graphite iron (CGI), and temper graphite iron (TGI). A metal matrix classification of cast irons is as follows; ferritic, pearlitic, martensitic, and bainitic (austempered) cast irons. In addition to the above different classifications of cast irons, cast irons are commercially classified into five main types of irons; gray, ductile, malleable, compacted graphite, and white iron. The first four aforementioned types of irons possess a common microstructure which consists of the graphite phase embedded in either ferritic, pearlitic, bainitic, tempered martensitic, or combinations thereof iron matrix. In addition, these four irons are classified according to the morphology of the graphite phase in each. In white cast iron, carbon is not present in its free phase (graphite). Carbon in molten iron does not form graphite, but remains combined with iron in the form of carbide. The following table summarizes the different classifications of cast irons by commercial designation, microstructure, and fracture [7].

Table 1 Classification of cast irons by commercial designation, microstructure, and fracture

Commercial Designation	Carbon-rich phase	Matrix[1]	Fracture	Final structure after
Gray iron	Lamellar graphite	P	Gray	Solidification
Ductile iron	Spheroidal graphite	F, P, A	Silver-gray	Solidification or heat treatment
Compacted Graphite iron	Vermicular graphite	F, P	Gray	Solidification
White iron	Fe_3C	P, M	White	Solidification and heat treatment[2]
Mottled iron[3]	Lamellar Gr+Fe_3C	P	Mottled	Solidification
Malleable iron	Temper graphite	F, P	Silver-gray	Heat treatment
Austempered ductile iron	Spheroidal graphite	At	Silver-gray	Heat treatment

The matrix composition in all cast irons classifications plays one prime role in the mechanical and thermal properties of cast iron. Nevertheless, the role of the carbon phase is as important in determining the mechanical and thermal properties of cast iron.

The American Society for Testing and Materials (ASTM) has classified graphite into seven types, as shown in the following table, defined in ASTM A247. Classification of

[1] F: ferritic, P: pearlitic, A: austenitic, M: martensitic, At: austempered (bainite).

[2] White irons are not usually heat treated, except for stress relief and to continue austenite transformation.

[3] This type of iron is not intentionally produced as it results from a transition between gray and white iron in a casting, and is not necessarily a desirable material.

the different graphite types is based on the graphite shape, morphology, and structure. The classifications of graphite is listed in **Table 2**

Table 2 Summary and description of ASTM and equivalent ISO classification of graphite shapes in cast iron

ASTM Type	Equivalent ISO form[4]	Description
I	VI	Nodular (spheroidal) graphite
II	VI	Nodular (spheroidal) graphite, imperfectly formed
III	IV	Aggregate, or temper carbon
IV	III	Quasi-flake graphite
V	II	Crab-form graphite
VI	V	Irregular or "open" type nodules
VII[5]	I	Flake graphite

Considering the classification of cast irons based on the morphology of graphite, three general types of cast irons are of interest to us; gray iron or *flake graphite iron* (FGI), ductile iron or *spheroidal graphite iron* (SGI), and *compacted graphite iron* (CGI). The characteristic morphologies of graphite structures in the different cast irons are shown in **Figure 1,** [1]**.**

[4] As defined in ISO/R 945-1969 (E).

[5] Divided into five subtypes; uniform flakes, rosette grouping, superimposed flake size, interdendritic, random orientation, interdendritic, preferred orientation.

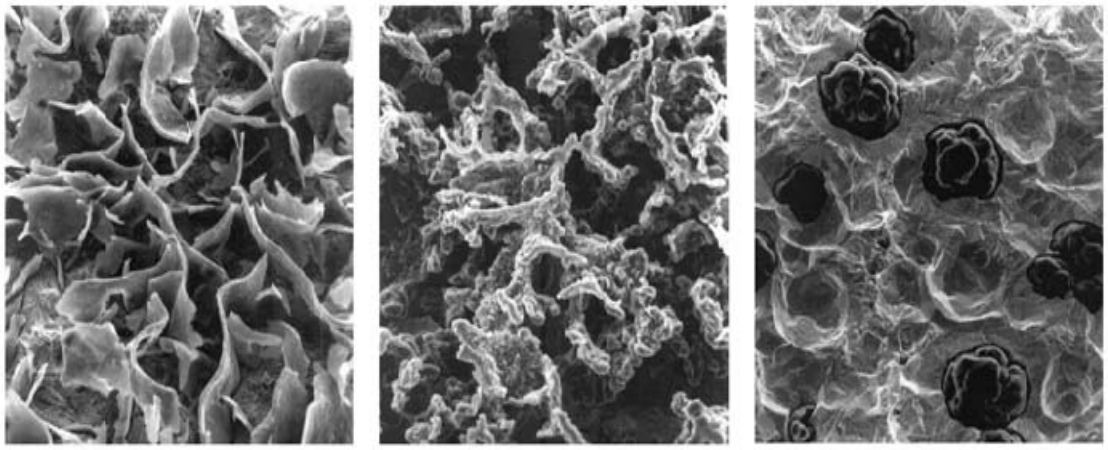

a) Flake graphite. b) Compacted graphite. c) Spheroidal graphite.

Figure 1 Different graphite morphologies in flake, compacted, and spheroidal irons

2.3 Gray Iron (Flake Graphite Iron)

Gray iron is always used to refer to a broad class of ferrous casting alloys normally characterized by its flake graphite microstructure in a ferrous matrix. Gray iron or flake graphite iron (FGI) is known for its lamellar graphite morphology. In flake graphite iron (FGI), graphite grows in an interconnected lamellar form within the eutectic cell and the lamellae are usually oriented randomly throughout the material. Although the particles are highly oriented, the overall material behavior is still isotropic in nature.

Large graphite flakes are associated with irons having high carbon equivalent and slow cooling rate. Graphite flakes sizes are usually determined by comparison with standard sizes prepared jointly by the AFS (*American Foundrymen's Society*) and the ASTM (*American Society for Testing and Materials*). The measurements are made based on the lengths of the largest graphite flakes in an un-etched section of the gray iron at 10x [8].

Large graphite flakes interrupt the continuity of the pearlitic matrix causing reduction in the iron's strength and ductility. Rapid solidification and hypoeutectic irons generally exhibit small, short flakes. The chemical composition of flake graphite iron (FGI) can be broken down, for simplicity, into three categories; 1) the major elements, 2) the minor elements, and 3) trace elements categories. The first category consists of the major elements; iron, carbon, and silicon. Most gray irons are produced with total carbon levels ranging from 2.5 to 3.6% with silicon levels normally vary from 1.7 to 2.5%. Most gray irons' mechanical properties are related to the combined percentage of carbon and silicon. The minor elements category usually includes phosphorus, manganese, and sulfur. Phosphorus is rarely added intentionally but is usually introduced to the melt from pig iron or scrap. The presence of phosphorus at low levels would increase fluidity during casting but at high levels can promote shrinkage porosity [9]. Thus it is of significant importance to control the phosphorus percentage and keep it within 0.02 to 0.1% for gray iron. Sulfur is very important in the nucleation of graphite in gray iron. Sulfur levels in gray iron should be in the range of 0.05 to 0.12% approximately. It is important that sulfur content be balanced with the manganese to promote the formation of manganese sulfide. The formation of manganese sulfide prevents the formation of brittle iron sulfide that would form at the grain boundaries. The trace elements category includes small percentages of elements which are added intentionally to control the nature and properties of gray iron. Such trace elements are tin, Vanadium ($\leq$ 0.08%), and copper which promote pearlite formation, and elements such as Boron ($\leq$0.02%) which promotes carbides formation [10].

The graphite particles in gray iron are interconnected and widespread throughout the iron matrix. Thus, gray iron breaks readily on impact with a brittle fracture exhibiting a gray fracture surface due to the presence of graphite on the fractured surface. Gray iron is characterized by a curved stress-strain relation with limited elongation [11]. A transverse (bending) test on gray iron is usually used to determine the yield strength, elongation, and reduction of area. Gray iron strength in compression is typically 3 to 3.5 times higher than in tension [11]. Accordingly, gray iron castings are usually used in machinery bases, pressure applications such as cylinder blocks, manifolds, pipe, pipe fittings, and fly wheels. The machinability of gray iron is superior to that of most other cast irons of equivalent hardness, and almost all steels. Gray iron's chip is discontinuous thus cutting inserts do not need chip breakers.

2.4 Ductile Iron (Spheroidal Graphite Iron)

Ductile iron, also known as spheroid [6] iron (or nodular) graphite iron, represents about 20 to 30% of the cast iron production [12]. Ductile iron has a structure containing graphite particles in the form of small, round, spheroid nodules in the metal matrix. The continuity of the matrix in ductile iron is much higher than in gray and compacted graphite irons. This results in superior mechanical properties. Nodular iron possesses superior strength compared to flake and compacted graphite irons due to the characteristic nodular morphology of the graphite which works as effective crack arrestors in the metal matrix. The addition of spheroidizing elements such as magnesium (about 0.04 to 0.06%) promotes the formation of graphite in this morphology. Magnesium, which reacts with

[6] The terms nodular and spheroidal are used interchangeably throughout this work.

sulfur and oxygen in the molten iron, precipitates out carbon in the form of small spheres (nodules). Elements such as lead, antimony, titanium, and bismuth should be avoided as they promote non-spheroid graphite formation.

The characteristic nodular morphology of graphite controls the mechanical and physical properties of ductile iron. Any deviation from this characteristic morphology will cause a deviation in the ductile iron's properties. Properties such as tensile strength, fatigue, and ductility will degrade as the percentage of non-nodular graphite increases. Production of greater than 90% nodular graphite is common practice. However, no flake graphite formation in the metal matrix is acceptable. Visual methods are used to estimate the percentage of nodularity and to give a rough guide of ductile iron properties. Graphite nodularity affects the modulus of elasticity, which can be measured by resonant frequency and ultrasonic velocity measurements. Such measurements are therefore often a better guide to nodularity and its effects on other properties [13]. Spheroidal graphite iron has the lowest thermal conductivity, damping, and thermal expansion as compared to gray and compacted graphite irons thus its use in engine block applications is limited. The machinability of spheroid graphite iron is the most difficult with tool wear being the highest as compared to the other two irons. However, spheroidal graphite iron has the highest modulus of elasticity, strength, and elongation thus it is well suited to applications requiring high strength.

2.5 Compacted Graphite Iron (CGI)

Compacted graphite[7] iron (CGI) is characterized by its unique intermediate mechanical and physical properties which lie between flake and nodular graphite irons. This is attributed to its unique morphology of graphite within the metal matrix. Graphite particles in (CGI) are short, stubby, with round edges, and are in the form of interconnected clusters within the eutectic cells. The term “vermicular” has been used to describe the graphite shape in compacted graphite iron. However, the term “compacted” has always been preferred because it is more descriptive of the three-dimensional structure and embraces all the varying degrees of compaction which has been referred to. In addition, the term “vermicular” has been used to refer to a fine worm-like graphite structure which is quite different than compacted graphite and is present in irons of very low sulfur content, which have been caused to solidify fairly rapidly. Vermicular graphite has been well described and illustrated by *Lux* [14]. The following table classifies the different types of vermicular graphite;

[7] Also known as quasi-flake, pseudo-nodular, semi-ductile, compacted-flake graphite, and upgraded iron

Table 3 Classification of vermicular graphite irons

	Dimensional characteristics of graphite			Mechanical properties of CGI			Remarks
Type of V. Graphite.	Max. length (l) μm	Max. thickness (t) μm	$\frac{l}{t}$	Tensile strength MPa	% elongation	BHN	
Type I	20	10	2-4	300-450	2-5	150-240	Similar to ASTM-D form
Type II	150	50	2-5	350-500	3-9	150-240	Similar to ASTM-M form
Type III	150	20	3-10	300-450	1-3.5	150-250	Similar to ASTM-P form

A comparison between the microstructures of compacted and vermicular graphite has been made in BCIRA[8]Broadsheet No. 138 [15], which emphasizes their quite different natures. The true nature of the structure of graphite can be fully appreciated by examining deeply etched samples under a scanning electron microscope as shown in **Figure 1**. Graphite particles in CGI are classified as type IV ASTM A247, as listed in **Table 2**.

2.5.1 Production of Compacted Graphite Iron

The first recognition of compacted graphite iron was not until the work of *Morrogh* and *Williams* of *BCIRA* in 1947 [16]. A patent was filed by *Millis et al.* for nodular graphite and compacted graphite irons simultaneously in 1948 [17]. The addition of magnesium (or calcium) to the melt in low percentage concentration was found to be insufficient to produce ductile iron but was found to sufficiently influence the graphite formation that was generated in the solidified cast. Further research by *Morrogh* and *Williams* using

[8] British Cast Iron Research Association

mischmetal (an alloy containing about 49% cerium, added to low sulfur iron) produced nodular and compacted graphite iron. *Lindsay* and *Shames* reported in 1952 that the greatest increase in tensile strength of compacted graphite iron was achieved with up to 19% nodular graphite particles [18]. Compacted graphite was also observed in irons of increased nitrogen content in 1953 by *Dawson* and others [19]. The presence of graphite, compacted to varying extents, has been widely reported in high nitrogen irons, especially those of large as-cast section size in which well-developed structures can occur[20]. Compacted graphite iron usually contains a percentage of graphite in the nodular form.

Addition of magnesium alone can be used to produce well compacted graphite, however, it requires a very narrow range of magnesium percentage making such a procedure so difficult to control that it is considered to be impractical. Exceeding this concentration of magnesium will render the graphite nodular, and too little magnesium will generate flake graphite. In a patented technique by *Shelleng* [21], it was reported that adding inhibiting nodular graphite using non-spheroidal elements such as titanium was successful at producing compacted graphite [22]. The effect of titanium on the formation of compacted graphite was later investigated by *Dawson* and *Evans* [23]. *Dawson* and *Evans* concluded in their investigation that the production of compacted graphite could only occur within a narrow band of magnesium addition (0.015 to 0.02%). However, the addition of 0.08 - 0.1% titanium extended the upper limit of magnesium to at least 0.03%, and the presence of cerium was found to be necessary to produce a fully compacted graphite structure [24]. Additional work was performed by *Evans*, *Dawson*, and *Lalich* in 1977 to produce compacted graphite iron by a single addition of a ferrosilicon containing magnesium,

titanium, and cerium to low sulfur base iron [25].

Currently, some manufacturers eliminate the addition of titanium due to its adverse effect on machining. One example is *Elkem AS*, where they developed a new alloy, called *CompactMag*™, for production of compacted graphite iron which is free from titanium and yet retains a good production window [26]. The composition of this alloy is shown in **Table 4**. The alloy contains 5 – 6% magnesium and 5.5 – 6.5% Rare Earth (RE) in a normal ferrosilicon base alloy. Elkem AS claimed that the addition of Mg+RE alloy in the rate of 0.3 – 0.45% as either a ladle or in-the-mould treatment will produce a good compacted graphite iron structure in commercial scale [26].

Table 4 CompactMag 5503 composition by Elkem AS

	%Si	%Mg	%RE	%Ca	%Al
CompactMag™ 5503 Alloy	44-48	5.00-6.00	5.50-6.50	1.80-2.30	1.0 Max

To summarize, three primary methods are used to manufacture compacted graphite irons, in addition to other less widely spread methods. The first and most common method is by the treatment of the liquid iron with alloys containing both nodularizing elements (Magnesium and RE elements) and denodularizing elements (Titanium or Aluminum) in US, UK, and Romania [27-28]. The second primary method which is based on the treatment of liquid iron with RE elements is mainly used in Australia, Russia, and Germany. The third primary method is based on extensive desulphurization of cast iron with rapid casting solidification cooling rate and possibly inoculation with Zr [29]. Also, by balanced magnesium and RE elements treatment of conventionally high sulfur content

grey cast irons [30]. Other common production techniques such as extensive desulphurization and by controlling the nitrogen content to produce compacted graphite are summarized in more detail in the literature with comparisons being made between the different techniques [31-32].

2.5.2 Classification Techniques of Compacted Graphite Iron

An acceptable compacted graphite iron should contain at least 80% compacted graphite and a maximum of 20% spheroid graphite with no flake graphite particles present [33]. Compacted graphite irons are classified based on the length to thickness ratio (aspect ratio) of graphite. This is better known as vermicularity of graphite. The vermicularity of graphite can also be related to the nodularity based on the following relationship:

$$\%\, vermicularity = 100 - \%\, nodularity \qquad (\mathbf{2.1})$$

One of the most important variables influencing the mechanical and physical properties of compacted graphite iron is the percentage of nodularity. As nodularity increases, compacted graphite iron's tensile strength and elongation percentage increase and will lean more towards nodular cast iron [34]. Nodularity of compacted graphite iron is determined as the ratio of the number of both type I and type II graphite particles (defined according to ASTM A-247) to the total number of graphite particles [35]:

$$\%\, nodularity = \left(\frac{No.of\ graphite\ types\ I\ \&\ II}{No.\ of\ graphite\ types\ I, II, III\ \&IV}\right) \times 100\% \qquad (\mathbf{2.2})$$

Despite the simplicity of the above formula and its practical advantage in production conditions, this method neglects the fact that several compacted graphite may belong to

more than one type introducing an error in measurement [36]. **Table 5** lists some mechanical and thermal properties of different grades of CGI. As shown in the table, both the strength and the elongation increase with increasing percentages of nodularity. This is due to the fact that nodular graphite morphology participates in crack evolution delay. This provides the material more ductility. However, the thermal conductivity of the material drops with increasing nodularity due to the resulting decrease of graphite interconnectivity within the matrix and the specific growth mechanism of nodular graphite. More details about the characteristic growth mechanisms of the different graphite structures in cast iron will be provided in the next section.

Regardless of that the classification in **Table 5** shows compositions with nodularity higher than 20%, nodular graphite contents up to 30% is expected in thin sections of the casts.

Table 5 Properties of CGI as a function of nodularity

Nodularity %	Tensile strength		Elongation%	Thermal cond. W/(m.k)	Shrinkage %
	MPa	ksi			
10 – 20	320 – 380	46 – 55	2 – 5	50 – 52	1.8 – 2.2
20 – 30	380 – 450	55 – 65	2 – 6	48 – 50	2.0 – 2.6
40 – 50	450 – 500	65 – 73	3 – 6	38 – 42	3.2 – 4.6

Several methods have been known to evaluate the compacted graphite structure, one of which is the nodularity of compacted graphite, as mentioned above. Another semi-empirical method which is used in industry due to its ease of reproduction, relates the

shape of the graphite particles to the ratio of tensile strength R_m to the hardness (HB) [37]. In this method, the graphite shape is expressed using the factor K_a, which is calculated using the following model:

$$K_a = \frac{1}{G}\left(1 - \frac{R_m}{3.5HB}\right) \quad (\mathbf{2.3})$$

where, G is the amount of eutectic graphite, expressed as:

$$G = CE + 2.1 = \left(C + \frac{Si}{4} + \frac{P}{2}\right) + 2.1 \quad (\mathbf{2.4})$$

For compacted graphite iron, K_a ranges from 0.18 to 0.23, for spheroid graphite iron K_a ranges from 0.02 to 0.07, and flake graphite iron K_a ranges from 0.32 to 0.38

2.5.3 Compacted Graphite Growth Mechanisms

The aim of this section is to establish a foundation on which the mechanical and physical properties of compacted graphite can be deduced for the finite element model. The reason for the intermediate properties of compacted graphite iron between flake and spheroid graphite irons of the same matrix structure is mainly due to the unique morphology and growth mechanism of compacted graphite [38-39]. The growth mechanism of graphite in the iron matrix is influenced by the type and amount of the alloying elements [38, 40-41].

Two nucleation scenarios of graphite formation in compacted graphite iron are proposed. The first scenario suggests that graphite nucleates in a flake-like shape then develops into a compacted-like structure. The second scenario is based on the fact that graphite initially nucleates in a spherical-like shape then it degenerates into a compacted-like graphite structure. Nevertheless, it is more accepted today that the spheroid shape is the ideal

growth behavior of graphite in liquid iron, and formation of flake graphite is a modified formation where the modifier agents could be sulfur and oxygen [42]. This is based on the fact that graphite would normally grow in a pure cast iron melt and solidifies in the form of spheroid shape. Accordingly, the preferred growth of graphite in an ideal environment would result in a nodular formation [43-44]. On the other hand, in the presence of impurities as the general case in the iron industry, untreated cast iron will normally contain flake graphite. Heterogeneous nucleation theory, which is one theory that is used to describe the nucleation of graphite in cast iron, is based on that graphite would nucleate on a pre-existing inclusion in the melt [45]. Using a focused ion-beam tomography, an inclusion of a second phase is observed in the middle of the investigated compacted graphite particle. Using EDX[9] analysis on cross-sections of the same sample, it was found that the inclusions consist of Magnesium-Sulfide (MgS) particles as these inclusions serve as nucleation sites for the compacted graphite particle [46].

The crystallographic lattice of graphite is of a hexagonal structure with two main axes; A-axis is in the basal plane direction and the C-axis is normal to the basal plane (the prismatic direction) as shown in **Figure 2**. Growth of graphite in the A-axis direction will dominate as a result of minute impurities such as oxygen and sulfur. These impurities, among others, will be absorbed on the prism face of the hexagonal graphite lattice and will cause the graphite to grow in the A-axis direction [44], forming flake graphite. The addition of alloying elements such as magnesium or Rare Earth (RE) metals (commonly cerium) to the iron melt will neutralize the impurities and, will deoxidize and desulfurize

[9] Energy-dispersive X-ray spectroscopy analysis.

the melt promoting balanced growth in both axes [47]. Exceeding these levels of magnesium or RE metals will promote the formation of spheroid graphite leading to nodular graphite iron [48]. Therefore it is important to have close control over the amounts of magnesium or RE metals in order to successfully produce compacted graphite iron.

In flake graphite the growth along the A-axis direction is dominant, while the growth in the C-axis direction is dominant in the nodular (spheroid) graphite [49]. As compacted graphite is a transitional structure, characterized by growth in the basal as well as the prismatic directions, with different growth rates occurring along the A-axis and along the C-axis due to changes in the minute surface active impurities. These impurities explain the branching and twisting of the graphite [50-51] .

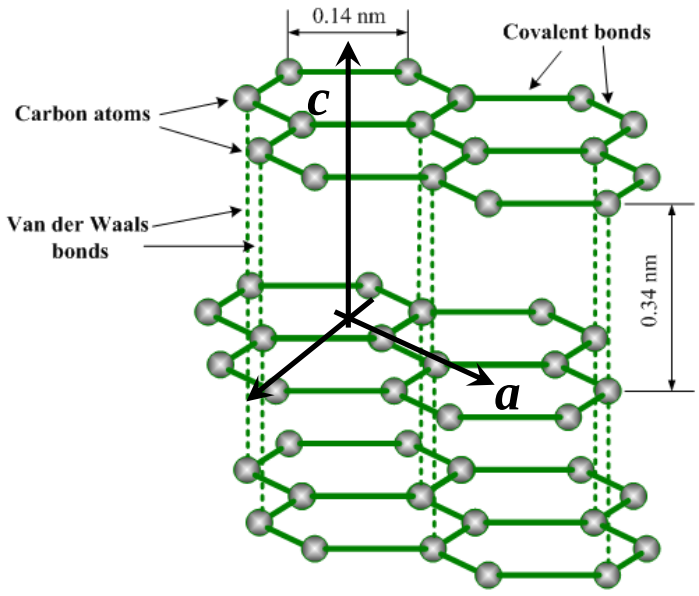

Figure 2 Crystallographic structure of graphite

The crystalline structure of graphite as shown previously consists of parallel layers of carbon atoms bonded covalently (in the range of 100-120 kcal/mole) together forming the basal plane of the hexagonal lattice [52]. Weaker Van der Waal's forces (in the range of 1-2 kcal/mole) hold basal planes, relatively widely spaced, together in the c-direction and are responsible for the beneficial lubricating behavior of the parallel basal planes. These two unequal bonding forces reflect the anisotropic nature of graphite and specifically its anisotropic elastic and thermal properties. Thermal conductivity parallel to the basal plane (a-direction) is one-hundred times more than it is in the perpendicular plane (c-direction) [44]. *Bushong et al*. (1964) reported that the thermal expansion behavior of graphite single crystals in the c-direction is one order of magnitude higher than it is in the a-direction [53]. As elasticity is correlated with the bonding forces, similar to thermal expansion, it is quite right to state that elasticity is inversely proportional to the thermal expansion coefficient and to the lattice distance at room temperature. Hence, one should expect a higher modulus of elasticity in the a-direction of the graphite lattice and a lower one in the c-direction. Such anisotropy in the elastic behavior can be confirmed experimentally on samples with known crystallographic preferred orientations (such as in carbon fiber based materials) [54].

Since graphite is one primary player in the determination of cast iron's mechanical and physical properties [55], it is useful to consider its strong crystalline anisotropic nature. Considering the coordinate axes shown in **Figure 2**, where subscripts 2&3 are in the basal

plane, then the stiffness tensor[10] C^*_{ijkl} will have five independent constants;

$C^*_{1111}, C^*_{2233}, C^*_{2222} = C^*_{3333}, C^*_{1122} = C^*_{1133}, C^*_{2233}, C^*_{1212} = C^*_{1313}$.

The values of C^*_{ijkl} are given in reference [56] and outlined in the following equation:

$$C^*_{ijkl} = \begin{bmatrix} C^*_{1111} & C^*_{1122} & C^*_{1133} \\ C^*_{1122} & C^*_{2222} & C^*_{2233} \\ C^*_{1133} & C^*_{2233} & C^*_{3333} \end{bmatrix} = \begin{bmatrix} 3.7 & 1.5 & 1.5 \\ 1.5 & 106 & 18 \\ 1.5 & 18 & 106 \end{bmatrix} \times 10^4 \text{ MPa} \qquad (\mathbf{2.5})$$

The term C^*_{2323} is not independent and is equal to: $(C^*_{2222} - C^*_{2233})/2$

From the above values of stiffness coefficients, it can be deduced that the strong basal (in-plane) bonding forces (covalent bonding forces) and the weakest bonding forces (Van der Wall's) are consistent with the high values of C^*_{2222} & C^*_{3333}, and the lowest value $C^*_{1212} = 0.018 \times 10^4$MPa , respectively. These stiffness coefficients are representatives of the anisotropic nature of the graphite crystal.

Despite the anisotropic nature of both the mechanical and thermal properties of the graphite crystals, the behavior of the polycrystalline graphite deviates significantly from those of perfect crystals. Crystallographic (a/c)-directions can no longer be used for the description of the mechanical and thermal properties of polycrystalline graphite in compacted graphite iron. However, this anisotropic nature associated with the interchanging growth directions of graphite supports the intermediate mechanical and thermal properties of compacted graphite iron between flake and spheroid graphite irons.

As graphite (free carbon) is several orders of magnitude more thermally conductive than the iron matrix, thus the thermal conductivity of cast iron is strongly influenced by the

[10] The fourth-rank stiffness tensor or elastic stiffness tensor are used interchangeably

amount, morphology, and distribution of graphite [57]. The interconnected graphite particles in flake and compacted graphite irons enhance their thermal conductivity compared to the isolated graphite nodules in ductile irons. As graphite works more like conduits within the metal matrix, the thermal conductivity of the bulk material varies with the type of graphite; flake, compacted, or spheroidal. In flake graphite iron, the dominating graphite growth is in the a-direction (basal plane) of the hexagonal lattice structure of graphite. Thermal conductivity in the *a-direction* of the hexagonal lattice of graphite is considerably higher than along the *c-direction* [58]. Since graphite growth in compacted graphite iron alternates between both “c” and “a” directions the thermal conductivity of compacted graphite is lower when compared to flake graphite, where the growth of graphite is not always in the higher conductivity plane [39]. To conclude, the thermal conductivity of compacted graphite iron is lower than in flake graphite iron due to the effect of the particular growth mechanism of the compacted graphite and the wider matrix bridges which already have a lower thermal conductivity than graphite [59].

The growth mechanism of graphite in spheroid graphite iron is in the lowest conductivity crystallographic plane, associated with isolated graphite particles within the eutectic cell. In addition, nodular graphite particles in spheroid iron are associated with wider matrix bridges leading to inferior thermal conductivity compared to compacted graphite iron.

2.5.4 Properties of Compacted Graphite Iron

2.5.4.1 Introduction

For a fairly fixed metal matrix composition, the mechanical and physical properties of compacted graphite iron are intermediate between those of flake and spheroidal graphite irons [38, 60]. The round edges combined with the irregular boundaries of the compacted graphite particles highly enhance the crack arrest resistance within the matrix and facilitates the good adhesion at the graphite-matrix interface, respectively. In addition, compacted graphite provides better thermal conductivity due to its interconnected formation within the matrix, and due to its growth structure when compared to nodular graphite.

The mechanical and physical properties of cast irons are influenced by the metal matrix composition (pearlite to ferrite ratio), the graphite morphology (nodularity and graphite shape), and the section size. Higher pearlitic compacted graphite iron is characterized by its higher strength, while ferritic compacted graphite iron is known for its ductility and lower strength. The pearlite to ferrite ratio can be changed by either the addition of alloying elements such as nickel, copper, or molybdenum, or by heat treatment. However, it should be recalled that for the compound to be compacted graphite iron, its nodularity must not exceed 20% and uncontrolled addition of these elements may increase the nodularity percentage. As nodularity increases, both strength, elongation, and accordingly fracture toughness will increase [33].

Compacted graphite iron strength is sensitive to cooling rate, thus the section size plays

an important role in establishing the material properties. The strength of compacted graphite iron will decrease the section size increases. An increased cooling rate will promote the formation of pearlite and increase the graphite nodularity percentage. The behavior is similar in flake graphite iron formation, however, the sensitivity of the tensile strength to wall thickness is substantially lower for the compacted graphite iron than it is for the flake graphite iron [44, 61].

Advantages of compacted graphite iron over flake graphite iron are [33]:

- Higher tensile strength at the same carbon equivalents and matrix composition,
- Higher tensile strength to hardness ratio,
- Higher ductility and toughness providing better crack resistance/fracture,
- Higher graphite-matrix interface strength.

Compared to ductile iron, compacted graphite iron has the following advantages:

- Lower coefficient of thermal expansion,
- Higher thermal conductivity and better resistance to thermal shock,
- Higher damping capacity,
- Better castability,
- Improved machinability.

Compacted graphite iron should be free of any flake graphite particles. The presence of a low percentage of flake graphite in compacted graphite iron will have a significant influence on its modulus of elasticity. Unlike in flake graphite iron where graphite particles are profusely interconnected and widespread in the iron matrix exhibiting a

stress-strain curvature at low stress levels, compacted graphite irons are expected to behave relatively more elastically over a wider range of stress. In addition, the modulus of elasticity of compacted graphite iron remains constant in the presence of applied tensile stress and elevated temperatures, until a certain temperature-dependent stress limit is reached [62-63]. The practical significance is that the actual elastic modulus of dynamically loaded compacted graphite iron components can be 50-75% higher than flake graphite iron of the same matrix structure [64-65]. However, compacted graphite iron's limit of proportionality is lower than that of nodular graphite iron.

Classification of compacted graphite iron based on the minimum tensile strength by ASTM is outlined in **Table 6**:

Table 6 Properties of CGI per ASTM A 842

Grade	Min. tensile strength MPa	Min yield Stgth MPa	Elongation in 50 mm. (2 in.)%	Hardness HB	BID[11] mm.
250[12]	250	175	3.0	179 max	4.5 min
300	300	210	1.5	143-207	5.0-4.2
350	350	245	1.0	163-229	4.7-4.0
400	400	280	1.0	197-255	4.3-3.8
450[13]	450	315	1.0	207-269	4.2-3.7

Several standardization bodies have different standards and codes for compacted graphite iron. **Table 7** lists the compacted graphite iron standards issued by other standard bodies:

[11] Brinell impression diameter (BID) is the diameter of the impression of a 10 mm. diameter ball at load of 3000 kgf.
[12] Grade 250 is a ferritic grade.
[13] Grade 450 is a pearlitic grade, usually produced without heat treatment with addition of certain alloys to promote pearlite as a major part of the matrix.

Table 7 Summary of CGI standards

Country	Issuing Body	Number	Year
International	ISO	ISO 16112	2006
International	SAE	J 1887	2002
Germany	VDG	W 50	2002
China	JB	4403-87	1987
Romania	STAS	12443-86	1986

Fang et al. compared the tangent modulus of elasticity of the three cast irons. A plateau in the tangent modulus of elasticity vs. stress was almost absent in the flake graphite iron compared to the nodular graphite iron. Compacted graphite iron exhibited an intermediate performance compared to other cast irons as shown in **Figure 3**. The presence and length of such plateau in **Figure 3** is due to the relatively extended elastic deformation zone presented by compacted graphite iron compared to gray iron. The curves in **Figure 3** are more described further in reference [66].

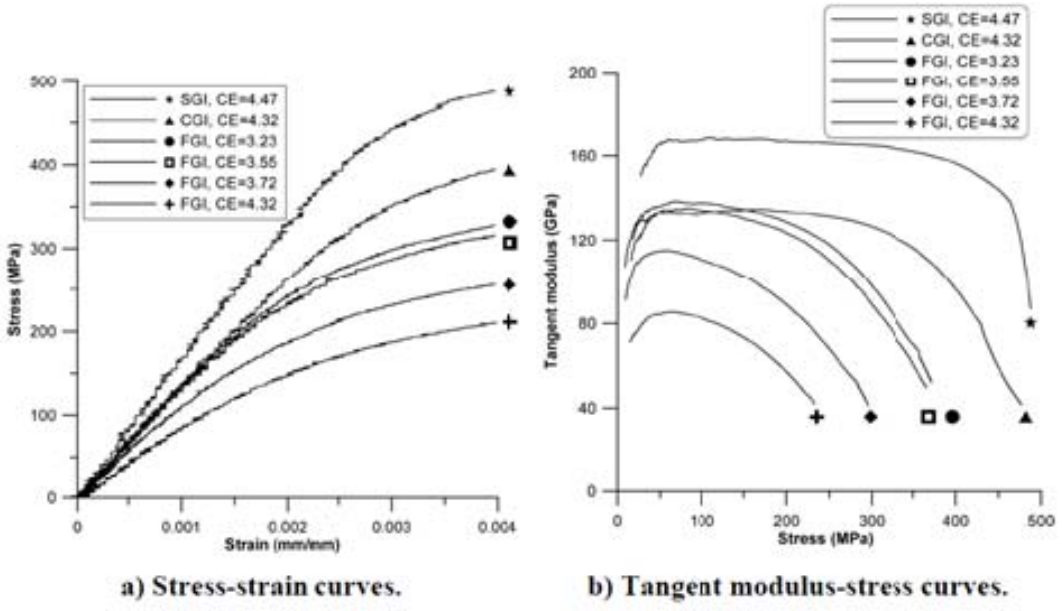

Figure 3 Stress-strain curves (a) and tangent modulus of elasticity versus stress (b) for the three cast irons (*Fang et al. 1995*)

Carbon equivalent values, in general, have direct effects on the strength of cast irons. However, the properties of compacted graphite irons are much less sensitive to variations in the carbon equivalent values than flake (gray) graphite irons. At carbon equivalents close to the eutectic value of 4.3%, both pearlitic and ferritic compacted graphite irons will maintain their higher strengths than the low carbon equivalent high duty unalloyed flake (gray) graphite irons. The sensitivity of mechanical properties, such as tensile strength, to wall thickness is substantially lower for compacted graphite iron than for flake (gray) graphite cast irons [33, 67].

2.5.4.2 Tensile Property

Tensile test results of compacted graphite iron are generally matrix dependent. However, the characteristic morphology of graphite in CGI provides CGI with better ductility, higher tensile strength, and modulus of elasticity when compared to gray iron of typical matrix structure. The modulus of elasticity of compacted graphite iron is determined at low stresses by making a measurement of the resonant frequency within a narrow band from 155 to 170 GN/m^2 for well developed compacted graphite structures [68].

Compacted graphite iron's maximum strain may reach values up to 6.7% for Ce-treated matrix with >95% ferrite [33], while gray iron seldom has any measurable elongation. Considering the same matrix structure, the tensile strength and yield strength of CGI are approximately 150% and 185-190% of gray iron, respectively [69]. Comparison between high-strength gray iron, Ce-treated CGI, and ductile iron properties are listed in **Table 8** [70].

Table 8 Comparison of properties of high-strength pearlitic FG iron, pearlitic FG iron, Cerium-treated CG iron, and ferritic SG iron in the cast condition, of the same chemical composition.

Property	HS FGI (100% P, 100% FG)	FGI (100% P, 100% FG)	**Ce-CGI (>95% F, >95 CG)**	SGI (100% F, 80% SG, 20% poor SG)
Ch. Comp%	3.10C,2.10Si,0.6Mn	3.61C,2.49Si,0.05Mn	3.61C,2.54Si,0.05Mn	3.56C,2.72Si,0.05Mn
T. Strength MPa	317	110	336	438
Elongation. %	…	…	6.7	25.3
M.O.E GPa	108	96.9	158	176
Brinell Hard HB	200	156	150	159
Th. Conductivity. W/(cm-k)	0.419	0.423	0.356	0.327

Typically, tensile strength would increase by 1.5 times with an increase of 10 to 20% nodularity [64], on the other hand, flake graphite should be totally excluded. Compacted graphite iron exhibits linear elasticity for both pearlitic and ferritic matrices, but to a lower limit of proportionality when compared to ductile iron. The ratio of yield strength to tensile strength ranges from 0.72 to 0.82, which is higher than that for ductile iron of the same composition. This makes it possible to achieve a higher loading capacity for CGI. The limit of proportionality is 125 MPa for both ferritic and pearlitic CG irons. It is slightly lower than that of ductile iron [71].

2.5.4.3 Impact property

Compacted graphite iron's impact property is closer to nodular irons than to gray irons. Charpy impact tests were run at room temperature and at 100ºC (212ºF) on V-notched samples made of gray, compacted, and nodular graphite irons. It was noticed that no change was shown for gray iron and the energy value was still low, while compacted

graphite iron's energy value increased by 25%, and the nodular iron's energy value was doubled at 100ºC (212ºF). It was also found that at room temperature and below (-40ºC) that a reduction of about 10% was found in the energy value in all three materials. However, when Charpy tests were run on unnotched bars, compacted graphite iron was found to have impact values of approximately four times those of gray iron, approaching those of nodular graphite iron. In addition, test data showed that compacted graphite iron was less notch sensitive compared to gray iron [69]. This can be reasoned by the effect of the round graphite ends in compacted graphite iron which work as crack arrestors.

2.5.4.4 Fatigue property

In regards to fatigue properties, it was found that the endurance ratio (ratio of unnotched fatigue strength to tensile strength) was approximately 0.45 and was unaffected by changes in the matrix structure [64]. This ratio was similar to that obtained for nodular graphite irons and low phosphorus engineering gray irons. It was reported that a V-notch in the fatigue test sample with a root radius of 0.25 mm reduced the fatigue strength of compacted graphite iron by 1.75. This strength reduction factor was calculated as the ratio of unnotched sample fatigue strength to the notched sample fatigue strength. This reduction factor was similar to that of nodular graphite iron as well [67]. It is evident that both impact and fatigue properties of compacted graphite iron are closer to nodular graphite iron than to gray iron. This is basically due to the absence of the sharp-edged graphite flakes which act as internal stress concentration localities in gray iron. The results of fracture toughness tests published by *Shen-Chih et al.* indicated that for the

same matrix microstructure, compacted graphite iron with higher vermicularity[14] yielded lower K_{IC} values, however these values were still higher than those of gray cast iron. [72].

2.5.4.5 Wear resistance

The wear resistance for unalloyed pearlitic compacted graphite iron is about one and a half times higher than the unalloyed pearlitic gray iron [64]. Results showed that when testing the wear behavior using pin-on-disc tests, there was about 45% less wear in compacted graphite iron than in gray iron [73]. Abrasive tests showed that the weight loss of compacted graphite iron specimens were 40-55% less than that of gray iron [74].

A series of scuffing tests were conducted by *Hogmark* & *Alander* to compare the wear resistance of various compacted graphite iron microstructures and compositions with commercially available cylinder liner materials such as alloyed gray iron, LASER hardened Cr- gray iron, and *Nikasil*[15] aluminum [75]. The scuffing tests were conducted by pushing a test specimen against a rotating nitride steel cylinder. It was found that the best performance was in the alloyed compacted graphite iron samples which simultaneously displayed the lowest friction and the highest scuffing load.

2.5.4.6 Thermal conductivity

Thermal conductivity of compacted graphite iron is slightly lower but closer to that of gray cast iron when compared to nodular graphite iron due to the interconnected network

[14] Vermicularity is defined as the percentage of the graphite existing in the vermicular form when the graphite aspect ratio is in between 2 and 10. Nodular iron would have an aspect ratio of 1, gray iron would have a aspect ratio of over 10.

[15] Nikasil is a trademarked electrodeposited lipophilic nickel matrix silicon carbide coating for engine components, mainly piston engine cylinder liners

of graphite in both irons; GI & CGI. In addition, the particular graphite growth structure of compacted graphite in CGI has better thermal conductivity than spheroid graphite as shown in **Table 9**.

Graphite is characterized by its high thermal conductivity, particularly flake graphite which is three to five times higher than that of either ferrite or pearlite. Accordingly, the amount and structure of graphite are critical factors in defining the thermal conductivity of cast iron. In order to quantify the effects of carbon content, especially in a range of 3.5–3.8% in compacted graphite iron, a series of controlled tests were conducted at the Australian Foundry Institute. It was found that thermal conductivity of CGI was 25% less than that of pearlitic gray iron at room temperature and 15-20% lower at 400ºC (752ºF).

Table 9 Thermal conductivity of micro-constituents in cast iron

Microstructure	Thermal Conductivity (W/(m-K))		
	0-100º C	500º C	1000ºC
Spheroid Graphite (along C-axis)	85	-	-
Flake Graphite (basal plane)	293-419	84-126	42-63
Ferrite	71-80	42	29
Pearlite	50	44	40
Cementite	7	-	-

As shown in **Table 10**, the thermal conductivity reaches its maximum for compacted and nodular graphite irons at about 200^{o}C [67, 76]. Thermal conductivity of compacted graphite iron gradually increases with increasing temperature. However, the presence of a relatively small percentage of flake graphite in the predominantly compacted graphite microstructure would cause the thermal conductivity to decrease with increasing

temperature. The decrease in thermal conductivity of flake graphite is rather interesting. In flake graphite, the graphite crystals are oriented in the most optimal way (basal plane) for good thermal conductivity. Increasing temperature will increase the movement of atoms which will likely cause the crystallographic orientation to deviate to a less than optimal orientation and more electron scattering which will result in lower thermal conductivity. Accordingly, a higher temperature increase will cause the flake graphite iron to become less thermally conductive. However, in compacted nodular graphite, a change in the crystallographic orientation would be for the better and increase the thermal conductivity. It is important to realize that this temperature dependency behavior for both nodular and compacted graphite is up to some critical temperature until the point where the scattering of electrons becomes too high and the thermal conductivity starts to decline. This is shown in **Table 9** as the thermal conductivity of flake graphite decreases with increasing temperature [77].

As in flake (gray) graphite irons, increasing the carbon equivalent in compacted graphite iron increases the thermal conductivity. The thermal conductivities of different cast irons at temperatures between 100^{o}C and 500^{o}C of pearlitic irons of various carbon equivalents and different graphite structures are listed in **Table 10**.

The graphite structure and carbon content have a significant effect on cast iron's thermal conductivity. Cast iron's matrix structure, as well, plays a role in thermal conductivity. It is reported that the thermal conductivity of ferritic CGI can exceed that of pearlitic gray iron at temperatures above 200ºC (392ºF) [62, 78], which may be expected from the data in **Table 9**. Accordingly, as with other types of cast iron, thermal conductivity of

compacted graphite iron would increase when replacing the pearlite content with ferrite.

Table 10 Thermal conductivity of flake, compacted, and nodular graphite irons

Cast Iron		Thermal Conductivity W/(m-k)				
Graphite Structure	Carbon Equivalent	100°C	200°C	300°C	400°C	500°C
Flake	3.8	50.24	48.99	45.22	41.87	38.52
Flake	4.0	53.59	50.66	47.31	43.12	38.94
Nodular	4.2	32.34	34.75	33.08	31.40	29.31
Compacted	3.9	38.1	41.0	39.4	37.3	35.2
Compacted	4.1	43.54	43.12	40.19	37.68	35.17
Compacted	4.2	41.0	43.5	41.0	38.5	36.0

2.5.5 Machinability of Compacted Graphite Iron

The outstanding combination of mechanical and thermal properties of compacted graphite iron (CGI) and the current significant advances in its processing techniques have made it a promising replacement for gray cast iron and aluminum to diesel engine manufacturers [79]. However, CGI's poor machinability presents a considerable hurdle to such replacement decision [80-82]. One critical reason for the poor machinability of compacted graphite iron (CGI) relative to cast iron is due to the absence of the protective and lubricating layer of manganese sulfide (MnS) which is typically formed on the cutting tool surface when gray iron is machined [1, 83]. Such a layer is found to grow denser at high cutting speeds (800m/min) when continuous cutting of cast iron is performed [84].

The lower percentage of sulfur in compacted graphite iron (CGI) (0.005-0.025%) compared to gray cast iron (0.08-0.12%) is one underlying reason for the absence of a

protective manganese sulfide's layer when machining CGI. Elements such as oxygen and sulfur are promoters for flake graphite formation. Accordingly, minimization of sulfur in the melt is ultimately needed for compacted graphite formation. Furthermore, the addition of magnesium balances the impurities in the melt and promotes compacted graphite formation.

Phillip was the first to conduct machinability test (continuous cut) on ferrite and pearlite grades of compacted graphite iron [85]. The machining tests were carried out with and without cutting fluids, using tungsten carbide (coated and uncoated) and ceramic (aluminum oxide) tools. From the tests, it was found that the machinability of CGI was intermediate between gray and spheroid cast irons. Modest improvement in CGI machinability was achieved when cutting fluid was used.

Several investigations have been performed to manipulate the metallurgical variables in CGI to achieve better machinability [1, 3]. Such investigations involved producing high sulfur CGI by adding manganese sulfide (MnS) into the melt. However, the strong thermodynamic affinity of magnesium prevented manganese sulfide (MnS) particles from forming and the high sulfur content led to the formation of magnesium sulfide. As a result, the abrasive magnesium sulfide inclusions were formed preferentially as compared to the lubricating and protective manganese sulfide layer in compacted graphite iron (CGI) leading to more aggressive cutting insert wear [86]. Aside from the absence of the protective and lubricating layer of manganese sulfide (MnS) in CGI machining, the presence of a low percentage of titanium in CGI poses a severe effect on cutting tool wear [87].

Higher amounts of titanium (0.1 – 0.25%) have been used to prevent the formation of spheroid graphite in cast iron and thus increased the stable magnesium range for CGI production. Despite the typical presence of titanium in cast iron (0.005-0.02%), higher percentage of titanium in CGI promotes the formation of titanium carbonitride (TiCN) inclusions which are harder than tungsten carbide and led to more aggressive cutting tool wear. It was found that a slight increase in the trace level of titanium from 0.01 to 0.02% is sufficient to reduce the tool life by about 50% as shown in **Figure 4** [1].

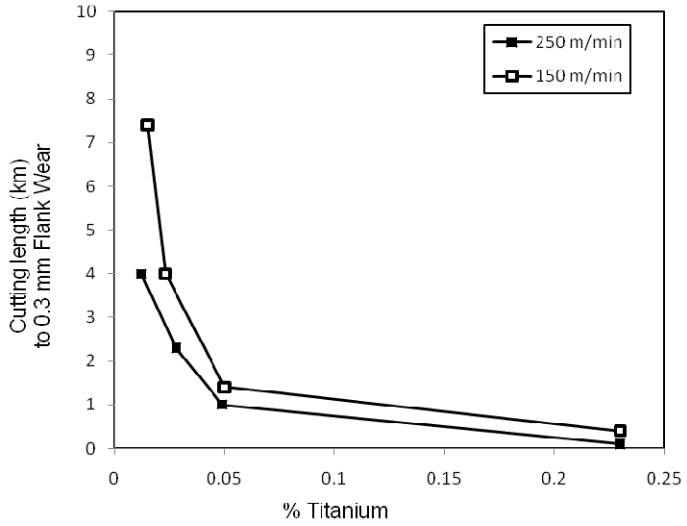

Figure 4 The addition of titanium dramatically reduces the tool life of compacted graphite iron during carbide turning

2.5.5.1 The Effect of Graphite Morphology

Since compacted graphite iron is composed of several constituents; pearlite, ferrite, graphite, and small amounts of other elements, a few studies have been performed to better understand the effect of each constituent on CGI's machinability [1, 80].

To understand the effect of the graphite morphology on CGI's machinability, high speed

turning tests (800 m/min) using Polycrystalline Cubic Boron Nitride (PCBN) cutting inserts showed that the most significant decrease in tool life occurred as the workpiece material changed from conventional pearlitic flake iron to a mixed flake/compacted graphite iron. In the same study, machining comparison of 50/50 flake-compacted, 5% nodularity with fully compacted, 80% nodularity CGI, and 85% nodularity CGI, graphite irons showed a less pronounced decrease in tool life, as shown in **Figure 5**.

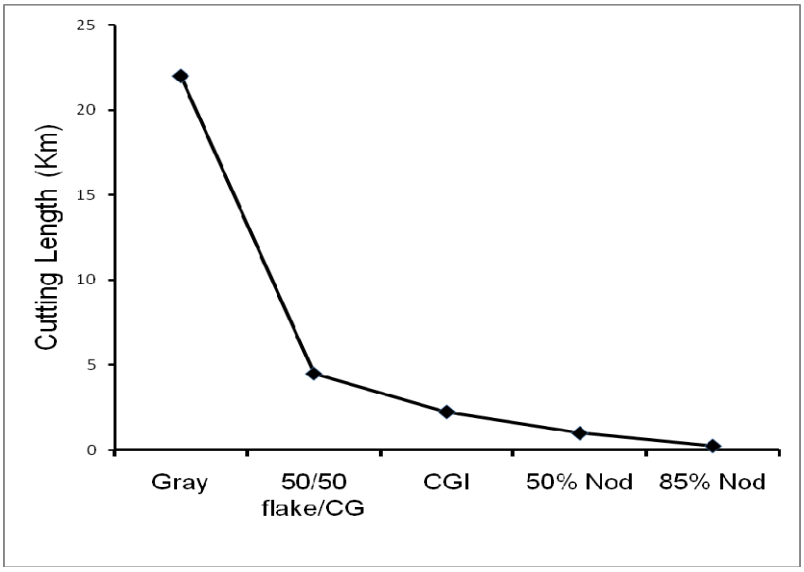

Figure 5 The influence of graphite shape on tool life for PCBN turning at 800 m/min.

Contrary to what might be expected, the 50/50 flake-compacted graphite iron should have an intermediate tool life between the fully gray and the 5% nodularity CGI, the 50/50 flake-compacted iron exhibited a performance closer to the 5% nodularity CGI. The reason is because the 50/50 flake/compacted alloy was produced from a standard desulfurized and magnesium-treated iron used for CGI and ductile iron production. Hence, the possibility for manganese sulfide (MnS) formation was greatly reduced, unlike

in the conventional pearlitic flake iron [1]. In parallel to the evaluation of the effect of graphite shape on machining of CGI, an alloyed gray iron (approx. 0.3% Cr and 0.25% Mo) was turned at different cutting speeds with PCBN and coated carbide. The tool life results showed no significant tool life difference between the alloyed gray iron and the 70-80% pearlitic CGI [1]. Decreasing nodularity, increased the tool life when CGI is turned at (150, 250, 400, and 800 m/min), as shown in **Figure 6** [1]. Keeping the matrix microstructure fixed, it is intuitively expected that changing from flake graphite to compacted graphite will have a negative impact on cast iron's machinability. However, nodularity has a more significant effect on machinability as it promotes higher strength, higher strain-to-fracture, higher hardness, and deficient thermal conductivity [3, 88].

2.5.5.2 The Effect of Pearlite content

Pearlite is a combination of interlamellar ferrite (*Fe*) and iron carbide (*cementite*) plates within the ferrite. The hard iron carbide plates reinforce ferrite (Fe) and makes it harder and more difficult to machine. Properties of pearlite are based on the amount and size of each of the cementite and the interlamellar ferrite layers [89]. The effect of pearlite content on the tensile strength, hardness, and elongation of compacted graphite iron's matrix is shown in **Table 11** [90].

Table 11 Nominal mechanical properties for different compacted graphite iron

CGI Mechanical Properties				
% Pearlite	Brinell Hardness	Min. Tensile Strength [MPa]	Min. Yield Stress (0.2% offset)	Min. Elongation
90% Min.	217-270	448	379	1%
10-90%	163-241	345	276	1%
10% Max.	130-179	276	193	3-5%

To evaluate the effect of pearlite on CGI's machinability, the amount of cementite in the pearlite grains and the ratio of pearlitic to ferritic grains should be considered. According to *Bates*, the amount of cementite in the pearlite phase of cast iron components can vary within the range of 8-15% depending on the product chemistry and cooling conditions. It was found that a higher content of cementite in the pearlite phase resulted in a significant reduction in tool life during drilling of gray cast iron [91].

To scientifically understand the effect of pearlite on CGI's machinability it is crucial to adopt a more detailed scenario. The effect of pearlite on machinability varies based on the machining process and the cutting tool chemistry. A study by *Dawson et al.* on the effect of the metallurgical variables on the machinability of compacted graphite iron, exposed the effect of pearlite content [1]. This study will be further analyzed in the review that follows.

Dawson et al. studied the machinability of CGI at different pearlite contents: (50-60%), (70-80%), and >95% with copper (*Cu*) + tin (*Sn*) stabilizers, in different nodularity percentages, at different cutting speeds, as shown in **Table 12**. Increasing the pearlite percentage of <5% nodularity CGI from (70-80%) to (>95%), was found to have a

negative effect on turning at (150, 250, 400, and 800 m/min) cutting speeds. However, increasing the pearlite content of CGI from (70-80%) to (>95%) at nodularity (5-10%) enhanced the tool life in milling as shown in **Figure 6**.

Table 12 Microstructure and chemistry details for evaluation of milling and turning as a function of pearlite content (Not all chemistry% is shown in the present table, complete table is in *Dawson et. al.* (2001))

Carbide or CBN	Turning or Milling	Microstructure		Chemistry (%)					
		%Pearlite	% Nod.	Mg	Cu	Sn	Mn	Sb	Ti
Both	Turning	50-60	5-10	0.012	0.43	0.029	0.40	0.004	<0.01
Both	Milling	50-60	<5	0.009	0.45	0.031	0.40	0.003	<0.01
Both	Turning	70-80	<5	0.011	0.46	0.033	0.40	0.004	<0.01
Both	Milling	70-80	5-10	0.009	0.43	0.036	0.41	0.004	<0.01
Both	Turning	>95	<5	0.013	0.75	0.090	0.39	0.005	<0.01
Both	Milling	>95	5-10	0.008	0.79	0.100	0.38	0.003	<0.01

An increase in the cutting length (tool life) corresponds to an increase in the pearlite constituent from (50-60%) to (70-80%) in turning, as shown in **Figure 6.** It is important not to erroneously relate this machinability improvement to the pearlite content alone. The actual reason for this machinability improvement was due to the lower nodularity percentage (<5%) in the (70-80%) pearlite range, as compared to (5-10%) nodularity in the (50-60%) pearlite range. However, the study did not show the effect of (50-60%) pearlite with (<5%) nodularity.

In addition to the above interesting findings, increasing the cutting speed improved

machinability in milling, but had a negative effect on turning. While the study did not provide details as to the reason behind the positive impact of the increased pearlite content and cutting speed on milling machinability, it concluded that the low pearlite alloys are too soft and deformable for easy cleavage and chip formation during milling while the high pearlite alloys are too hard and abrasive for continuous cutting. The study exposes helpful experimental results of the pearlite content on CGI machinability which may be analyzed as will be explained ahead.

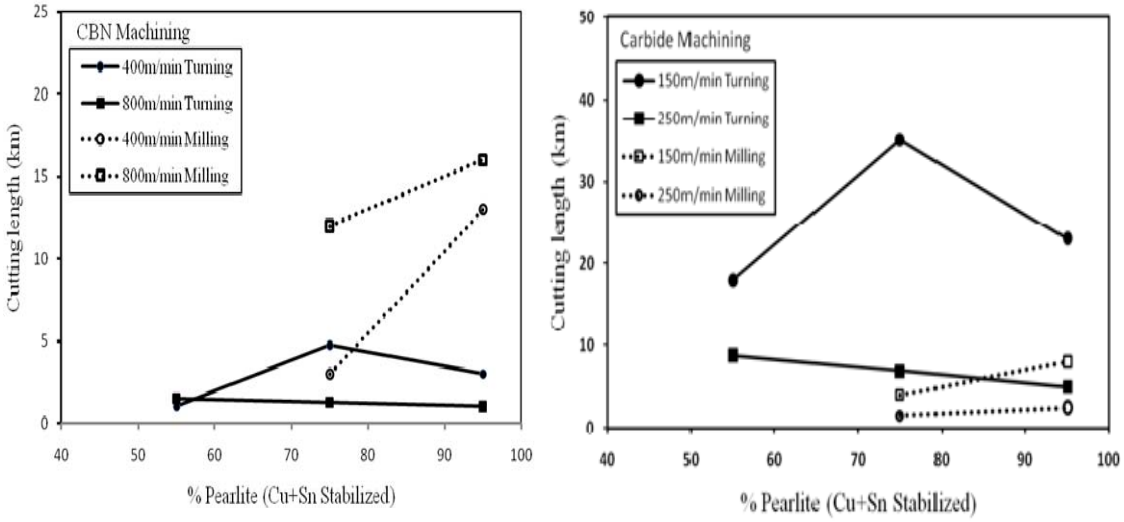

Figure 6 The effect of pearlite content on tool life during milling and turning using CBN (left) and Carbide (right), stabilized with copper and tin *(Dawson et. al. (2001)*

The presence of graphite in cast irons, in general, promotes the formation of segmental chip. During gray iron machining, the formation of a damaged region ahead of the tool tip [3, 92] causes the early formation (and separation) of the chip and a shorter chip-tool contact time when compared to the chip formation in ductile metals. CGI, as a cast iron, will have the same chip formation mechanism except that its better ductility than gray

iron will prolong the chip-tool engagement time.

A fundamental difference between milling and turning operations is the workpiece/tool engagement time. In milling each tooth will stay in contact for a period of time that depends on a number of variables one of which is the cutting speed. Once each cutting tooth completes its cutting stroke it will disengage from the workpiece and experience a cooling period. This thermal cycling is unavailable in turning. This explanation of the tool scenario will be used to explain the positive and negative influences of pearlite content on milling and turning machinability in the following section.

As pearlite is less ductile than ferrite, at lower pearlite content, CGI tends to have higher ductility and higher fracture strain. This prolongs the overall ductility promoting the metal to stay relatively longer in contact with the cutting tool. Increasing CGI's pearlite content consequently decreases the overall ductility and lowers the overall fracture strain promoting sooner material fracture and less chip-tool contact. As the tool life is judged by the tool wear, less chip-tool contact time translates into longer tool life.

The tool life in milling clearly benefits from a cutting speed increase up to a point, as shown in **Figure 6.** As both carbide and CBN tools show an increase in the tool life as result of a cutting speed increase, it is not possible to attribute this to the tool chemistry. However, CBN does have a higher cutting speed endurance. For both tools, increasing the cutting speed in milling, despite the cutting tool chemistry, will shorten the chip-tool engagement time and provide longer tool life.

Unfortunately, this relationship scenario is not typically found when turning CGI. Unlike in milling, during turning the tool stays in contact with the workpiece for as long as the

cutting process lasts. In addition, the tool will not experience any cooling periods until turning is concluded. Despite that the positive influence of pearlite in milling is greater than the negative influence in turning [1], it is important to realize that increasing pearlite does not have a positive impact when turning.

To justify the negative influence of increasing pearlite in turning, the following hypothesis may be proposed. During turning, the continuous workpiece-tool contact generates a significant amount of heat which is dissipated away from the cutting tool to prolong its life. A considerable amount of heat is removed with the machined chip. The good thermal conductivity of the workpiece material has a significant effect on the cutting region heat dissipation and thus serves to increase the tool life. As pearlite possesses lower thermal conductivity than ferrite due to the effect of cementite [93], increasing the pearlite content lowers the overall thermal conductivity of the material and degrades the tool life. Once again, it is more evident that the positive effect of pearlite on milling is more significant than the negative effect on turning as shown in **Figure 6**.

As the tool stays in contact with the workpiece for as long as the turning processes continuous, increasing the cutting speed will have a significant negative effect on the tool life. Longer contact of the tool with the workpiece will raise the cutting zone temperature leading to reduced tool life, as shown in **Figure 6**.

Dawson's study exposed the machining of CGI with two different pearlite stabilizers; antimony (Sb) and manganese (Mn). In this case PCBN was compared to carbide to investigate the influence of the two stabilizing agents on each material's tool life. According to Dawson, manganese stabilization (Mn-CGI) to 100% pearlite did not affect

PCBN tool life either in a positive or negative way. On the other hand, manganese stabilized CGI (Mn-CGI) to 100% pearlite exhibited increased the tool wear in carbide tool especially at low speed (150 m/min). However, lack of sufficient data led to inability to explain the effect of manganese on tool life in turning.

Stabilizing pearlite with antimony (Sn) provided a slight increase in tool life, especially at lower turning speeds (150 m/min. for carbide and 400 m/min for PCBN), compared to 70-80% pearlite levels. In addition, adding antimony (Sn) to increase the pearlite content caused the formation of needle-like graphite resulting in lower tensile strength. Accordingly, stabilizing pearlite with antimony was not recommended by Dawson for this reason. Unfortunately, no milling test data was provided in the study for either Mn-CGI or Sn-CGI.

2.5.5.3 The Effect of the Cutting Tool Material

Compacted graphite iron introduces a set of superior engineering properties over gray iron in automotive and locomotive industries. However, optimized CGI machining that is comparative to gray iron is still to be pursued. Several works are aimed to explore the effect of CGI on the performance of different insert materials.

Milling of gray iron using PCBN could achieve a cutting length of 20-25 km at 800 m/min. However, under the same cutting conditions and for a typical iron matrix, the tool life was reduced by 30-50% when CGI was milled using PCBN and ceramic tools. More significant reduction of tool life (about 10% of gray iron's) was found in continuous machining of CGI at the same cutting conditions [94]. From there it is clear that

compacted graphite iron is still much inferior to gray iron specifically in continuous cutting, **Figure 7**, [95].

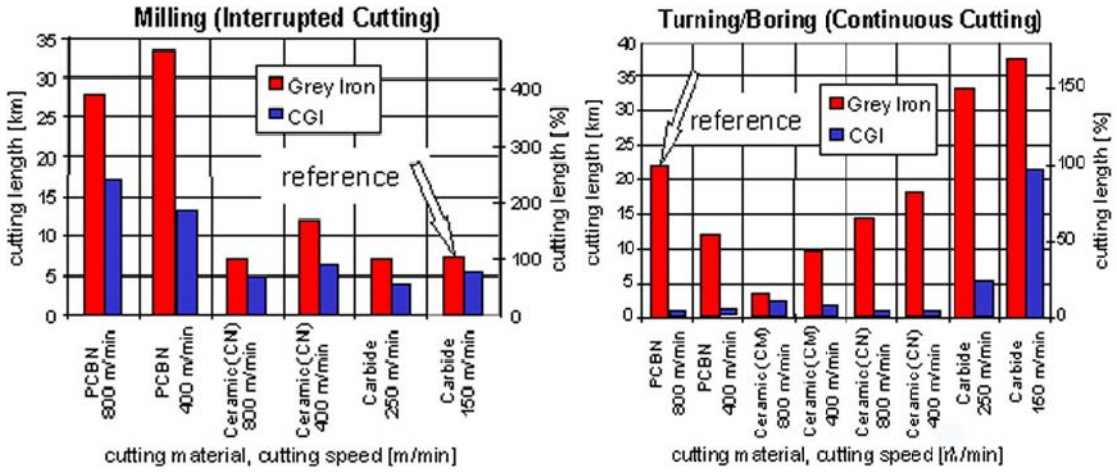

Figure 7 Comparative tool life for different tool materials in interrupted (milling) and continuous (turning/boring) cutting of 70-80% pearlitic CGI and gray iron

A performance comparison in milling of 98% pearlitic CGI of average hardness 230 HB by *Gabaldo et al.*[96], using coated carbide inserts; (TiCN, Al_2O_3 and TiN on the flank face and TiCN and Al_2O_3 on the flank face) and a Si_3N_4 (*Sialon*)-based ceramic tool. The Si_3N_4-based ceramic has higher toughness when compared to Al_2O_3-based ceramics and a low coefficient of thermal expansion, which is characterized by its good resistance to thermal shocks [97]. All milling operations were coolant free and the flank wear limit was set to $\leq$0.3 mm for cutting speeds 140, 220, 280, and 340 m/min, using a K15 carbide grade. More on the K15 carbide grade specifications can be found in the open literature [96]. Based on machined volume material criterion, the carbide's tool life did not show a significant decrease when the cutting speed increased to 420 m/min. At higher cutting speeds; 680 and 850 m/min, the carbide inserts presented a significant decrease in tool

life tendency. According to *Gabaldo,* carbide inserts presented longer tool life than the ceramic inserts when they were tested under the same cutting conditions, similar to other researchers [98]. In addition, *Gabaldo's* study showed that attrition was the main wear mechanism in carbide up to a cutting speed of 420 m/min. As the cutting speed was further increased, chipping and thermal cracks were observed due to the significantly higher cutting temperature.

Pretorius et al. evaluated different cutting tool materials for continuous CGI machining [84]. The CGI grade used in the study was GJV400, >95% pearlite, and 10% nodularity). The cutting insert materials evaluated were Polycrystalline Cubic Boron Nitride (PCBN), Polycrystalline Diamond (PCD), Ceramic, Cermet, and coated carbide. The machining conditions are listed in **Table 13**.

Table 13 Machining variables used to evaluate different cutting insert materials (Pretorius 2006)

Machining Variable	
Cutting speed (m/min.)	100 - 350
Feed rate (mm/rev.)	0.1 – 0.35
Depth of cut (mm.)	0.25
Coolant	Compressed air (5 bar)
Time (min)	5
Flank wear (mm.)	0.05

Using CGI machining wear maps, Pretorius found that Polycrystalline Diamond (PCD) was the only material with low enough wear (0.02 mm/5 min.) that was capable of reaching a similar tool life as in machining gray iron with PCBN. It was found that PCD will go through a transition from mechanical to thermal wear mechanisms as the cutting

conditions get more severe. At a low cutting speed (200 m/min) and a high feed rate (0.35 mm/rev.), the wear mechanism was predominantly mechanical. At higher cutting speeds (300 m/min) and a low feed rate (up to 0.2 mm/rev.) the wear was predominantly thermal. PCD was able to machine at double the speed of carbide and achieve a 10-20 fold increase in tool life. It also outperformed the PCBN tools.

As cermet inserts are considered to be more chip and abrasion resistant, its hardness can be increased by adding titanium carbide (TiC) and titanium nitride (TiN) [99]. Two types of cermet inserts were used in the study; TiN-based and Ti(C, N)-based. It was found that neither one was suitable for continuous cutting of CGI. The wear after 5 minutes of turning was found at 0.12 mm. Despite that the Ti(C,N)-based cermet insert was more wear resistant, however, the wear mechanism in both insert types was abrasion. Accordingly, cermets were not considered further as they were found to be inefficient for CGI machining.

Two types of ceramic inserts were used in the study; Al_2O_3 and Al_2O_3-TiC coated ceramic insert. Likewise, the ceramic inserts were discarded despite the fact that the Al_2O_3-TiC coated inserts outperformed the aluminum oxide coated insert, due to the severe flank wear (0.1 mm/5 minutes) that was generated. In support of the inferior performance of ceramic inserts in CGI machining, *Souza et al*. recommended cutting speeds less than 200 m/min [83, 100].

In an effort to improve CGI's machinability, a study by *Diamini et al.* using PCBN inserts on dry turning of 5% nodularity, 70% pearlitic compacted graphite iron [101] was prepared to study tool wear when machining CGI. The study used two end-of-life criteria;

maximum flank wear scar size of 0.3 mm, and a surface finish criterion which is based on the requirements of the final application. In this study, the tool possessed a negative rake angle of -6º, flank angle 6º, and a lead angle of 45º, and a cutting speeds range of 400 – 800 m/min. *Diamini* reported that tool wear at a high cutting speed (600 – 800 m/min) was dominated by crater wear. Decreasing the cutting speed prolonged the tool life and wear was then mainly observed on the flank surface. A transfer layer on the cutting edge was found that comprised mainly of (Ti, C, and Al) from the tool and (Si, Fe, Mg, and C) from the workpiece due to the significant high edge temperature (about 1135ºC). A layer deposited on the trailing edge of the cutting tool was observed on a region that was not in contact with the workpiece, identified as a secondary melt wear [102]. The main wear mechanisms reported were chemical and diffusion wear, and oxidation wear due to the exposure of the CBN to oxidation. Diffusion wear was confirmed after a separate study by Abele et al. [80] which compared gray and compacted graphite irons in machining. Both metal samples were maintained in contact with PCBN for 6 hours at 700ºC and 1050ºC in a pure helium atmosphere (99.99%). It was found that at both temperatures, elements including boron, tungsten, and titanium were diffused into the specimen materials. Oxidation was found when the samples were heated to temperatures exceeding 950ºC in an oxygen containing environment leading to oxidation of the tool binder in the form of titanium dioxide (Ti_2O) and the presence of microcracks at the oxidation sites.

Aside from the dry turning of CGI, a study by *Varghese et al.* was carried out to assess the effect of tool material, tool topography and minimal quantity lubrication (MQL) on the machinability of CGI [103]. The study concentrated on coated carbide and coated

cermet inserts, and ceramic insert materials. Flat and grooved coated carbide, grooved coated cermet, and chamfered ceramic inserts were used. All inserts were tested under dry and MQL machining conditions. Commercial machining conditions were applied for the practicality of the tests. The machining was performed at cutting speeds of 250 and 400 m/min, depth of cut 1.524 mm, and a feed rate of 0.28 mm/rev, for 5 seconds per insert. The machined CGI's basic characteristics are listed in the table below:

Table 14 Basic characteristics of CGI test specimen

CGI, %	Nodularity%	Pearlite %	Hardness HB	Ult. Strength MPa	Elongation
>95	<5	>95	254	520	1.2

According to *Varghese et al*'s. test results, flat coated carbide inserts provided higher cutting forces in dry and MQL conditions compared to grooved coated carbide inserts. However, machining under MQL conditions at low speed (250 m/min) caused an increase in the cutting forces when flat coated carbide and grooved coated cermet inserts are tested. A reduction in cutting forces under MQL conditions was found using grooved coated carbide and flat ceramic inserts. At higher cutting speed (400 m/min), machining under MQL conditions increased the cutting forces for all cutting inserts.

The highest cutting forces were recorded when a flat coated carbide (dry and MQL) and flat ceramic inserts (dry) were tested at a low speed (250 m/min). The lowest cutting forces were recorded when a grooved coated carbide (dry) was used to machine at a high cutting speed (400 m/min)

CHAPTER 3

Metal Cutting Modeling

3.1 Introduction

A metal cutting process in its simplest form can be described as a shearing process where a well defined cutting tool is advanced into the workpiece material, shearing off part of it as a chip. The cutting tool should have specific geometries aimed to provide a controlled shearing action. Despite the geometric complexities of most cutting tools used today, all cutting tools in conventional machining processes should have two primary faces in common; rake and flank faces. The rake face is simply to facilitate the shearing action and sliding of the cut material over the cutting tool face, while the flank face is the opposite side of the tool which faces the machined surface with both surfaces determining the cutting tool wedge angle. The wedge angle mainly controls the cutting tool strength and temperature. The flank angle is responsible for any friction of the cutting tool back surface with the machined material which may cause both degeneration of cutting tool and product quality. The two faces meet together to form the cutting edge(s).

Modeling the cutting process often takes the form of one (or combination) of the following models: analytical, slip-line, mechanistic, and finite element, models.

3.2 Analytical Models

Analytical models [104-108] establish relationships between the force components based on the cutting geometry. These models are usually simple to apply, however, a prior knowledge of the shear angle or chip thickness and mean-friction angle should be determined experimentally. This typically limits their applicability and accuracy. One common model was proposed by *Ernest* and *Merchant* [109].

3.3 Slip-line Models

Slip-line models [110-118] depend on the work material properties, rather than on experimental data. These models predict mechanical response and temperature distribution, and are compatible with strain, strain-rate, and temperature-dependent models. However, the geometry of the slip-line field in the shear zone must be modeled, assumed, or somehow determined. One relatively recent Slip-line model was proposed by *Oxley* [110].

3.4 Mechanistic Models

Mechanistic modeling is a semi-empirical method capable of accurately predicting the cutting forces in a wide range of complex machining operations [119-122]. While this type of model is semi-empirical, changes in the cutting conditions under which they were calibrated will render them invalid [123]. This approach is based on the assumption that cutting forces are proportional to the uncut chip area. The constant of proportionality, called the specific cutting energy, depends on the workpiece material, the cutting

conditions, and the cutting geometry. The form of the function relating the specific cutting energy to the cutting geometry and conditions is assumed. The actual function is then determined by fitting experimental data in a calibration process. Calibration can be based on simple orthogonal or oblique machining set-ups. Geometric transformations can then be applied to predict cutting forces for a complex, three-dimensional machining process [124].

3.5 Finite Element Models

The finite element method has been successfully used to model the cutting process for over four decades. However, progress in formulation and techniques is continuing. One of the earliest was due to *Klamecki* in 1973 [125]. Despite *Klamecki*'s model precedence, it was limited to the incipient cutting stage. A model by *Usui et al*. assumed a steady-state chip geometry and an incremental advancement of the tool [126-127]. *Iwata et al.* modeled the orthogonal cutting process using a rigid-plastic finite element model [128]. However, the model did not consider the effect of temperature on the cutting process. *Stevenson et al.* conducted pioneering work in thermal finite element analysis of machining [129-130]. *Lajczok* proposed a cutting model based on plain strain principle [131]. Other models have been used to predict the residual stresses in machined parts [132-134]. The significant advancements in digital computational resources in the late eighties, promoted the advancement of the finite element modeling of orthogonal cutting by *Strenkowski* and *Carroll* [135-137].

Following the previous pioneering foundational efforts, other efforts have been

introduced to study other phenomena in the cutting process. Studies of the segmental chip formation in orthogonal cutting by the finite element method by *Ceretti* [138]. *Natarajan* and *Jeelani* used a viscoplastic model to predict the chip geometry [134]. Recently, *Marusich et al*. developed a model with adaptive remeshing that can predict non-steady chip formation [139-141].

Since the finite element method is basically a discretization process of the continuum problem, the finite element cutting models are based on meshing the workpiece using different types of elements. A fundamental consideration when modeling a continuum problem is the choice of an appropriate kinematic description of the continuum. Such a choice will determine the relationship between the deforming continuum and the finite element mesh. Continuum mechanics algorithms utilize two classical descriptions of continuum motion; the Lagrangian and Eulerian descriptions.

3.5.1 Lagrangian Formulation of Motion

In the Lagrangian description, the finite element mesh (grid) is attached to the continuum material. Each individual node of the mesh follows the associated material particle and takes the updated geometry of the deforming workpiece material throughout the simulation. The Lagrangian formulation is mainly used when the continuum deformation is studied. Since the Lagrangian formulation is attached to the continuum material points, severe distortion of the mesh is expected. Therefore, several methods are used to remap the finite element mesh to handle the resulting levels of mesh distortion associated with machining. The Lagrangian models usually need more computational resources. The first

model of orthogonal cutting using an updated Lagrangian formulation to simulate chip formation from incipient stage to steady state was performed by *Strenkowski* and *Carroll* [137, 142-143]. To prevent mesh distortion, the model had to include a material failure and parting mechanism to allow the chip to separate from the workpiece [144].

3.5.2 The Eulerian Formulation of Motion

In the Eulerian description, the finite element mesh (grid) is fixed and is more useful in continuum flow models. In other words, the mesh is fixed and the continuum moves with respect to the mesh. The conservation equations (momentum, mass, and energy) are formulated in terms of the spatial coordinates and time. Therefore, the Eulerian description of motion only involves variables and functions having an instantaneous significance in a fixed region of space. Hence, the material velocity at a given node corresponds to the velocity of the material point coincident at a particular instant of time for the node under consideration. The velocity v is consequently expressed with respect to the fixed mesh without any reference to the initial configuration of the continuum and the material coordinates.

The Eulerian models are used to calculate the variables needed at different time instants. Eulerian models are faster with less computational resources used, and are not vulnerable to mesh distortion since the mesh is spatially fixed. The Eulerian formulation has been used to model other manufacturing processes, such as metal forming and extrusion [145-148]. The first application of the Eulerian formulation to metal cutting was due to *Strenkowski* and *Carroll*. In this model, the boundary of the chip was determined in

advance and the model was used to study the steady-state cutting only. Despite the need to determine the chip shape in advance, the model did not need a chip separation criterion and fewer elements were needed to model the chip and the workpiece. However, other work by *Zienkiewicz* was published to automatically update the chip geometry [149].

3.5.3 The Arbitrary Lagrangian Eulerian Formulation of Motion

To overcome the shortcomings of both Lagrangian and Eulerian formulations, the Arbitrary Lagrangian-Eulerian (ALE) technique was developed. This technique was successfully able to combine the advantages of both techniques [150-152]. The ALE method was introduced into the finite element method from fluid mechanics for modeling the solid-fluid interaction and free surface problems [153-154]. In the ALE description, the finite element mesh nodes are allowed to move with the continuum as the case in the Lagrangian scenario or held fixed as in the Eulerian description. This freedom of node motion provides the method with the ability to continuously handle a greater degree of distortion in the continuum than in the Lagrangian method alone with more resolution than in the Eulerian method alone. However this freedom should not be overshadowed by the burden of specifying mesh velocities well suited to the particular problem under consideration. Therefore, successful implementation of the ALE method requires that an automatic mesh displacement prescription algorithm be supplied.

3.5.4 Chip Separation Criteria

3.5.4.1 Introduction

The success of studying machining using the finite element method (FEM) is due to the various material models and complex boundary conditions which can be, to a reasonable accuracy, simulated. In addition, more detailed information can be obtained from the finite element model analysis than from conventional research methods. However, one issue that is critical to the success of the finite element model is the chip separation criterion.

Since machining changes the geometry/dimensions of the workpiece by removal of parts of the workpiece material, the finite element model will have to simulate this separation phenomenon. The updated Lagrangian formulation is used to describe the material geometry throughout the machining process. Each node in the finite element mesh is allocated to a specific material point. Accordingly, to prevent mesh distortion due to chip formation, the chip elements will have to be mathematically departed from the rest of the workpiece mesh. Several mesh separation (chip separation) criteria have been proposed in finite element simulations.

Mainly, chip separation criteria are divided into two categories: (1) geometrical and (2) physical criteria. *Huang* and *Black* reported that the chip geometry, distributions of maximum shear stress, effective stress, and effective plastic strain in the chip and the machined surface were not sensitive to the type of chip separation [155]. However, the magnitude of the chip separation criterion showed a significant effect on the mesh

distortion, maximum shear stress and the effective stress on the machined surface. They also recommended a geometrical criterion if only steady state cutting was of concern because the magnitude of the criterion would be easier to determine. If both incipient and steady-state cutting were of interest, a criterion based on a combination of geometrical and physical conditions would be used.

3.5.4.2 Geometrical Chip Separation Criteria

In the finite element simulation using the updated Lagrangian formulation, a chip parting line is normally predefined. Two coinciding sets of nodes are located on the chip parting line. In the geometrical chip separation criterion, a critical distance *"d"* between the tool tip and the two coinciding nodes immediately ahead of it is specified as shown in **Figure 8.** Once this distance is reached, the two coinciding nodes will be separate [156]. One node will belong to the chip and the other will define the finished workpiece surface. The main disadvantage of the geometrical criteria is that they are not based on a physical phenomenon.

Usui and *Shirakashi* first introduced a geometrical chip separation criterion [126]. *Komvopoulos* and *Erenbeck* observed that sufficient distance between the overlapping nodes and the tool tip was essential to avoid convergence issues due to elemental distortion [157]. Determination of the distance *"d"* has been proposed by *Zhang* and *Bagchi* to be 10% to 30% of the element length [158]. Later, they proposed a geometrical chip separation criterion which used the ratio of the distance *"d"* to the depth of cut claiming that this criterion was equivalent to micro-fracture mechanics [159].

A coupled thermo-mechanical model of plane-strain orthogonal metal cutting with continuous chip formation was proposed by *Mamalis et al* [160]. The model was able to predict the stress, strain, strain-rate, and the developed cutting forces. In addition, the model was reasonably able to predict the temperature distribution in the chip, the workpiece, and the cutting tool. The model employed a geometrical chip separation criterion that was based on a critical distance "d". *Mamalis* et al. reported that the critical distance at which node separation would take place was specified equal to 0.003 mm. This distance was about 5% of the element length and according to *Mamalis* was small enough to ensure continuous chip formation. The critical separation distance had no physical basis and accordingly was experimentally determined by *Mamalis*.

A geometrical chip separation criterion was compared to the energy density criterion by *Lin et al*. [161]. The choice of a critical distance between 0.01 and 0.03 of the element length gave reasonable results. However, this range was merely based on trial and error. It is not to disqualify the results, though. The selected distance was based more on empirical data and ultimately found to be material and machining conditions dependent. Interestingly, *Lin et al.* concluded that despite the success of the geometrical criterion, combination of the geometrical criterion and a separation criterion based on the strain energy would be much better.

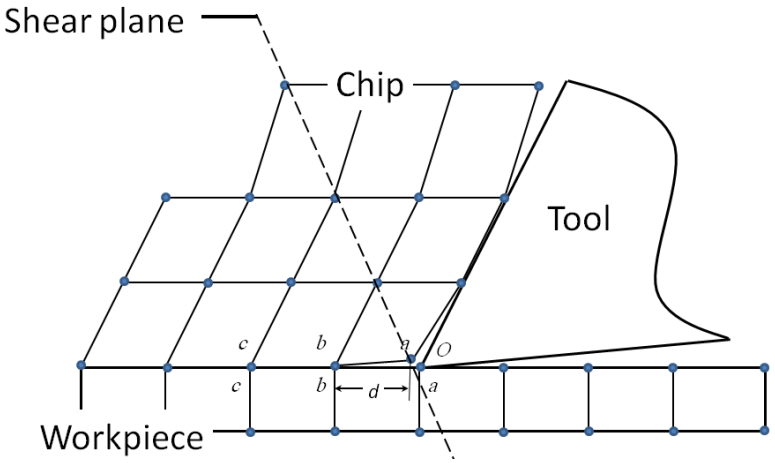

Figure 8 Geometrical chip separation criterion showing the twin node separation at prescribed distance *"d"*

3.5.4.3 Physical Chip Separation Criteria

Physical chip separation criteria are based on threshold values of selected physical variables: accumulated effective plastic strain [162], *von Mises* strain [137, 163-165], or strain energy density [166]. According to *Atkins*, the separation criterion required in the finite element model will have to closely reflect the physics of separation at the tool tip rather than a computational fix [167].

Physical chip separation criteria use mechanics models, in general, to calculate the fracture threshold variable ahead of the tool tip to which fracture will take place. *Strenkoweski* and *Carroll* studied a criterion based on the effective plastic strain [137]. They reported that the chip geometry was largely unaffected by the choice of the criterion value from 0.25 to 1.00 effective plastic strain, unlike the residual stresses which increased by increasing the criterion value.

Lorentzon et al. studied the transition between continuous and segmental chip formation.

They compared two physical chip separation criteria: *Cockroft-Latham* (C-L) fracture criterion [168] which is based on plastic strain energy considering hydrostatic stress, and the accumulated plastic strain used by *Hortig* and *Svendsen* [162]. *Cockroft-Latham* fracture model considers the effect of the maximum principal stress (σ_1) over the plastic strain path. According to the *Cockroft-Latham* model, damage occurs when the accumulated stress state over the plastic strain reaches to a critical damage value (D_{cr}) as given by:

$$D = \int_0^{\bar{\varepsilon}_f} \sigma_1 \, d\bar{\varepsilon} \qquad (\mathbf{3.1})$$

Where, $\bar{\varepsilon}_f$ is the effective fracture strain and σ_1 is the maximum principal stress. From the above equation, chip damage begins when the damage expression reaches a critical damage value $D = D_{cr}$. The above model takes the hydrostatic tension into account using the positive part of the major principal stress, i.e. $\sigma_1 = \sigma_1$ if $\sigma_1 \geq 0$, and $\sigma_1 = 0$ if $\sigma_1 < 0$, which means that damage cannot decrease. This later form of *Cockroft-Latham*'s model was used by *Ceritti et al.* [169] and later by *Calamaz et al* [170].

Lorentzon et al. found that due to the importance of thermal softening and material fracture roles in the chip segmentation process, a separation criterion with hydrostatic dependency should be employed.

An energy density based criterion was considered by *Lin et al.* to simulate chip separation. *Lin et al.* based their study on the strain energy density being a material constant [171]. *Iwata et al.* considered a criterion that was based on a ductile fracture

mechanism that considered stress history [128].

Ng et al. [172] used conditional link elements criterion **Figure 9**. Two node link elements were placed between the chip and the workpiece surfaces along a predefined separation path. Separation of the elements was based on a shear failure criterion which is a function of the effective plastic strain. Once the effective plastic strain reaches the "damage" plastic strain, the conditional linked element will fail and be deleted accordingly.

Segmental chip formation was also modeled by Ng et al. using a Johnson-Cook damage model [173]. The *Johnson-Cook* damage model considers the effect of strain, strain rate, and temperature on fracture strain. Once the strain reaches the fracture strain calculated by the *Johnson-Cook* model, the element is removed allowing for chip separation.

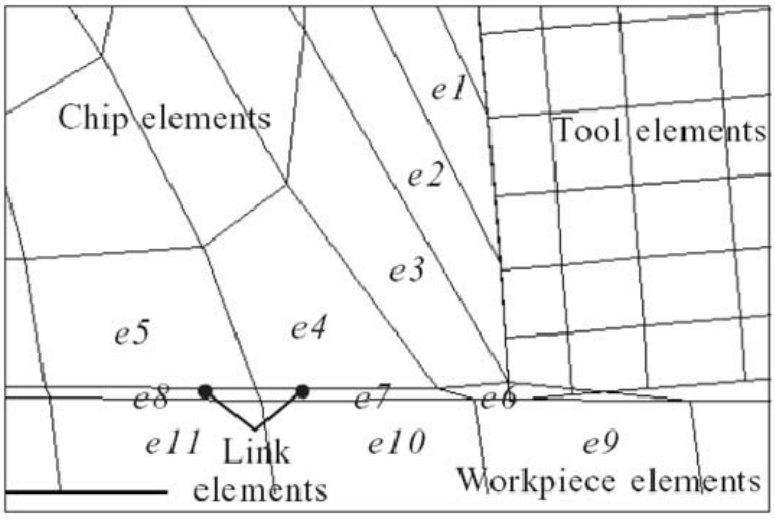

Figure 9 Conditional link elements inserted in between the chip and workpiece elements, modeled by *Ng et al.(2002)*

CHAPTER 4

Orthogonal Metal Cutting

4.1 Orthogonal Metal Cutting

The metal cutting process has been explained in a simplified model by *Piispanen* [174], shown in **Figure 10**. The model explains the cutting process considering the steady state condition without a built-up edge with the chip shown as a series of thin stacked sheared planes (lamellas) of the machined metal on the front of the cutting tool face. The sheared lamellas would form an angle (φ) with the plane of cut metal, the shear angle, which defines the primary shear plane. The shear angle would eventually change into (ψ) once the cut metal departs from the primary shearing zone.

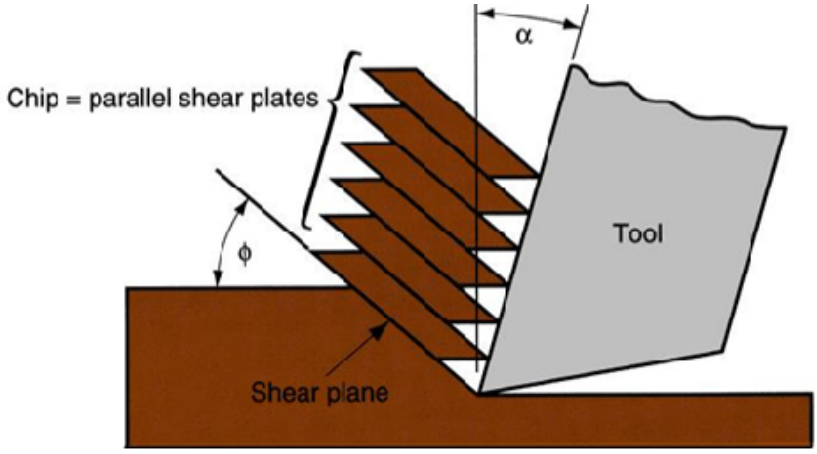

Figure 10 Piispanen Cutting Model

Despite *Piispanen*'s simplified model and its lack of considering the secondary shear zone, chip curl, tool-chip contact length, and the cutting tool plasticity, it presented the

shear plane theory in a very simple manner and illustrated some fundamental aspects of the orthogonal cutting process [175].

However, *Piispanen* has recognized the importance of the normal stress on the shear plane and its influence on the shear plane angle (φ). *Piispanen* has also tied the shear plane angle (φ) to the principle of minimum energy and tried to graphically deduce a predictive relationship of the shear plane angle. In addition, Piispanen has considered the effect of strain hardening on the direction of shear in the graphical method, though no experimental data was presented [176].

Despite the complexity and advancement of today's cutting tools, one relatively simple and fairly understood form of metal cutting scenarios used to model the cutting process is the orthogonal metal cutting process [111]. In orthogonal cutting, **Figure 11** , the cutting edge of the tool is parallel to the work surface of the material being cut and perpendicular to the direction of the relative motion of the tool and the workpiece (orthogonality condition). According to *Shaw* [175], other conditions should be present in addition to the aforementioned scenario to be realistic:

- The depth of cut should be large enough compared to the feed per revolution (*single straight cutting edge condition*),
- The uncut chip thickness of the cut metal (t) should be small enough compared to its width (w) such as $w>20t$ (*plane strain condition*) ,
- The cutting tool edge should be perfectly sharp with no cutting edge preparation, and no flank surface rubbing with the machined surface.
- The cutting edge width is greater than the workpiece width,

- No built up edge formation during cutting,
- Continuous chip formation during cutting (*steady state condition*).

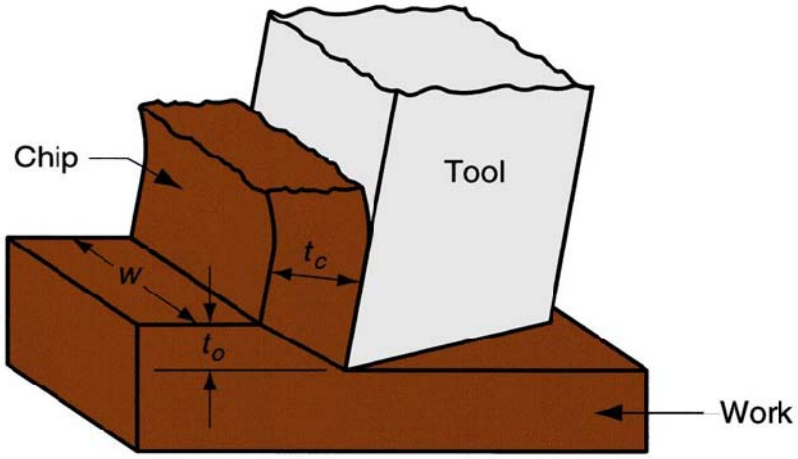

Figure 11 Orthogonal cutting principle

It is important to emphasize that the width of cut is large compared to the uncut chip thickness such that the side spread of material is concentrated at the edge and the material flow in general takes place in planes perpendicular to the work surface and parallel to the direction of cutting [111]. As the cutting tool proceeds into the workpiece material, the material will be subjected to concentrated shearing action. Considering orthogonal cutting and seeking simplicity, several researchers considered the shearing action would occur along a straight shear plane at angle (φ) relative to the cutting plane; the shear angle [177]. The shear angle can vary within a considerable range depending on a number of parameters such as the cutting tool geometry, the workpiece material, and the cutting conditions. In this scenario, uncut material of thickness "t_0" will pass through the shear plane and under shear deformation it will separate from the rest of the workpiece then

slide over the cutting edge surface in the form of chip with thickness "t_c". The thickness of the cut material (chip thickness) is typically greater than the uncut material thickness.

Considering the chip as a separate body in mechanical equilibrium under two opposite and "collinear" equal forces, these two forces are simply the resultants exerted by the cutting tool on the back of the chip and its reaction as the force applied by the workpiece on the base of the chip. These two forces are considered to hold the chip in equilibrium. The force *R* which is applied by the tool on the chip may be resolved along the tool face into two forces; (1) the friction force F_c, which is tangent to the tool face and is responsible for the work expended in friction between the chip and the tool face, and (2) a force normal to the tool face component; "N_c". The mean friction angle "β" is the angle between the normal force "N_c" and resultant "*R*". The resultant *R'*; applied by the workpiece on the base of the chip, can be resolved into two systems of forces. One system of forces is along the shear plane as a force parallel to the shear plane "F_s" and the perpendicular component "N_s". Force "F_s" is responsible for shearing the metal along the shear plan, and the normal force component "N_s" is responsible for the compressive stress acting on the shearing plane. The other system of forces is resolved into a force parallel to the direction of motion "F_p" (*cutting force*) and the normal component "F_q" (*thrust force*).

The relationships between the different force components can be determined from the force diagram proposed by Merchant [175]:

$$F_s = F_p \cos(\varphi) - F_q \sin(\varphi) \qquad (\mathbf{4.1})$$

$$N_s = F_q \cos(\varphi) + F_p \sin(\varphi) = F_s \tan(\varphi + \beta - \alpha) \qquad (\mathbf{4.2})$$

Where F_p and F_q are measurable, one can express the shearing and normal stresses on the shear plane (considering both stresses are uniformly distributed along the shear plane) as:

$$\tau_s = \frac{F_s}{A_s} = \frac{\big(F_p \cos(\varphi) - F_q \sin(\varphi)\big)\sin(\varphi)}{A_c} \qquad (\mathbf{4.3})$$

$$\sigma_s = \frac{N_s}{A_s} = \frac{\big(F_q \cos(\varphi) + F_p \sin(\varphi)\big)\sin(\varphi)}{A_c} \qquad (\mathbf{4.4})$$

The mean coefficient of friction is determined as:

$$\mu = tan\beta = \frac{F_c}{N_c} = \frac{F_q \cos(\alpha) + F_p \sin(\alpha)}{F_p \cos(\alpha) - F_q \sin(\alpha)} \qquad (\mathbf{4.5})$$

Considering the velocity diagram, we can deduce the following relations:

$$V_s = \left(\frac{\cos(\alpha)}{\cos(\varphi - \alpha)}\right) V \quad , \quad V_c = \left(\frac{\sin(\varphi)}{\cos(\varphi - \alpha)}\right) V \qquad (\mathbf{4.6})$$

The shear strain and the shear strain rate are:

$$\gamma = \frac{\cos(\alpha)}{\sin(\varphi)\cos(\varphi - \alpha)} \quad , \quad \dot{\gamma} = \frac{V_s}{\Delta s} \qquad (\mathbf{4.7})$$

As seen from the previous formulae, the shear plane angle is a parameter that plays a major role in determining shear and normal stresses on the shear plane as well as the shear strain and shear strain rate. Several analytical models have been developed to predict the shear plane angle.

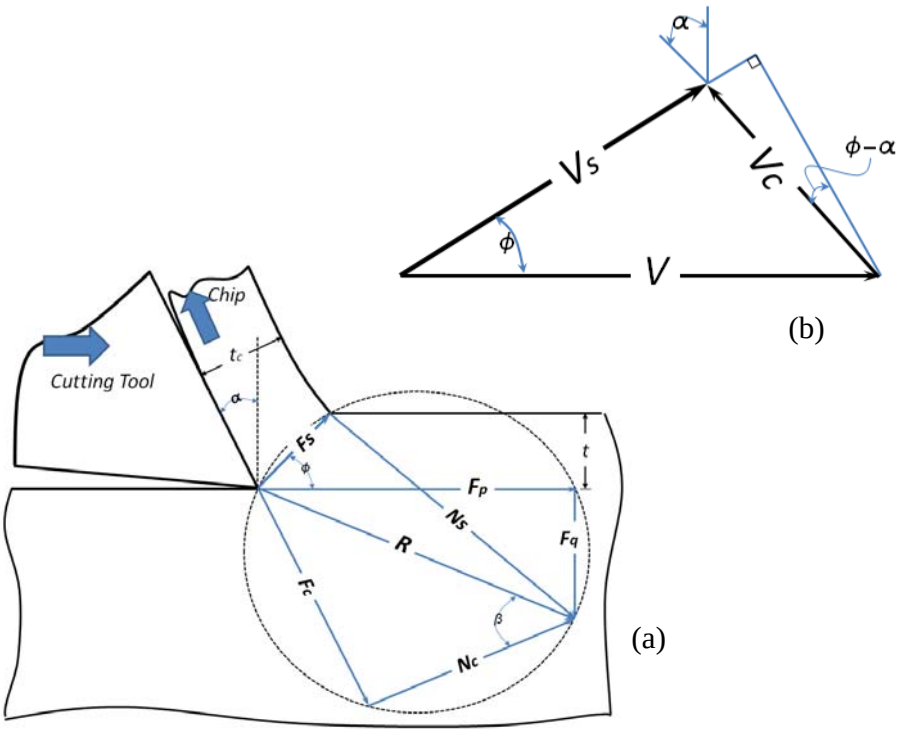

Figure 12 Merchant circle force diagram (a), Velocities diagram (b)

4.2 Chip Formation

4.2.1 Introduction

As the cutting tool proceeds into the workpiece, the workpiece material "generally" undergoes a shear deformation. Shearing takes place at three shear zones: primary shear zone (PSZ), secondary shear zone (SSZ), and tertiary shear zone (TSZ). During machining, most of the cutting energy is transformed into heat. As most of the plastic deformation takes place in the primary shear zone (PSZ), which extends from the tip of the cutting edge to the free surface of the workpiece, about 75% of the cutting heat energy

is produced. In the secondary shear zone (SSZ) about 25% of the cutting heat energy is produced, i.e. between the chip and the cutting tool face (chip-tool interface). In the tertiary shear zone about 5% of the cutting heat energy is produced, i.e. between the tool flank surface and the finished workpiece surface [178]. The formation of the chip is initiated mainly in the primary shear zone and to a much smaller degree in the secondary shear zone. The first task in analyzing the cutting process is to examine the chip produced. The chips are controlled by several cutting conditions such as the cutting speed, feed rate, depth of cut, cutting tool material and geometry, cutting temperature, and the workpiece material. As much as all these factors affect the cutting chips, they affect the cutting forces and the quality of the produced workpiece.

4.2.2 Types of Chips

4.2.2.1 Introduction

Early contributions to the study of chip formation were based on the work of *Mallock* [179] and *Taylor* [180]. Several chip classifications have been proposed since then: *Piispanen* [176], *Ernst* [109], *Recht* [181], *Rice* [182], *Davies* [183-184], and *Komanduri* [185]. However, the standard classification of chip formation for most materials as a function of cutting speed within the conventional speed range starts with a discontinuous chip (TYPE I), then continuous chip with built-up-edge (BUE); (TYPE III) and finally continuous chip; TYPE (II). The three types of chips were defined by *Ernst* in1938 [109] and *Merchant* in 1945 [104] in their early development of the theory of orthogonal cutting [186]. Further increase in the cutting speed causes instability in the cutting process in

both the primary and secondary shear zones in addition to the dynamic response of the machine tool structure yielding chip segmentation [187]. Other recognized classification was based on the state of the chip formation such as steady state continuous chips and cyclic chips [188] .

Chip type is a result of several interacting factors: material microstructure, mechanical and physical (thermo-plastic characteristics) of workpiece material properties, and previous material treatment, cutting conditions, frictional conditions (SSZ), and the machine tool structure and its response to the cutting conditions. The workpiece material and cutting speed effects on the chip type have been studied by several researchers [187, 189-190].

4.2.2.2 Type I Discontinuous Chip

Type I (*discontinuous*) chips are generally formed when cutting brittle materials, material containing concentration spots (such as graphite flakes in cast iron, or manganese sulfate inclusions in free-cutting steel), and some ductile materials at low cutting speeds and high feeds [175].

In brittle materials, discontinuous chips form by fracture and crack propagation. The mechanism of discontinuous chip formation has been described by *Cook*, *Finnie* and *Shaw* [191], *Palmer* [192], and *Field* and *Merchant* [193]. *Field* and *Merchant* introduced the mechanics of discontinuous chip formation by cutting under a very low cutting speed (0.515 fpm). They found that a discontinuous chip possessed a large shear angle in the beginning of machining which gradually decreased as machining progressed.

Finally, when the chip strain reached its critical value, it fractured and the entire process started all over.

As special case of the catastrophic shear chip, a discontinuous chip occurs when complete separation between the individual chip segments occurs as a result of the periodic rupture of the shear failed surface. In a discontinuous chip, the upsetting of the incoming workpiece material ahead of the tool occurs. This deformation is concentrated in a narrow band from the tool tip to the chip-free interface. This is followed by crack formation ahead of the tool tip due to a tensile stress concentration. Crack formation is further followed by rapid propagation which leads to rupture along the shear surface. Failure in the primary deformation zone is of a brittle nature and there will be no re-welding of individual segments.

Iwata and *Ueda* (1977) [194] found that the growth direction of initial fracture in discontinuous chips appeared to lean toward the direction approaching the maximum shear strain rate. After the fracture had grown to a suitable size, it continued to grow along the shear band until it reached the free surface.

Komanduri considered a discontinuous chip as one of several types called serrated or cyclic chip types [195]. According to *Komanduri*, serrated chips or cyclic chips are divided into four types; 1) wavy chip, 2) catastrophic shear chip, 3) segmental chip, and 4) discontinuous chip.

The wavy chip is mainly due to regenerative chatter under self excited vibrations causing variation in the undeformed chip thickness, rake angle and clearance angle. This type of chip has a symmetrical harmonic characteristic form. As the cutting process oscillates

close to the natural frequency of a part such as a tool in the machine system, this causes resonance and large amplitudes of vibrations [196-201]. The limited rigidity and low damping of the tool and workpiece supporting system are mainly the cause of this type of chip.

Catastrophic shear chip occurs at very high cutting speeds due to plastic instability and intense localized deformation in the primary shear zone leading to catastrophic shear failure between segments [181]. At high cutting speeds, the concentration of thermal energy in narrow bands can be due to insufficient time for the dissipation of heat from these bands. According to Shaw, most of the segment is formed by an upsetting process undergoing small amounts of strain separated by a thin highly strained concentrated shear band which acts as a plastic hinge. During this stage, the deformation in the primary shear zone is highly localized [202-203]. Catastrophic shear chip is also observed in certain materials of poor thermal properties such as difficult-to-machine titanium based materials and nickel based superalloys that have poor thermal properties and high strength at elevated temperatures [187].

The segmental chip type occurs due to certain instabilities in the primary shear zone as a result of the heterogeneous nature of the workpiece material giving rise to inhomogeneous plastic deformation [195, 204]. The segmental chip type formation is characterized by large strains, low shear angles that oscillate cyclically and exhibit stick-slip friction on the rake face. The instability in the cutting process is due to the negative stress-strain characteristics of certain materials at large strains, involving void formation around second phase particles and propagation into microcracks in the primary shear zone

and coalescence of these cracks leading to partial fracture. In other words, in addition to the cutting conditions, chip segmentation depends very much on the composition and microstructure of the workpiece material. This fracture process is the source of instability leading to chip segmentation.

4.2.2.3 Type III Continuous Chip with BUE

Type III (*continuous with BUE*) occurs at speeds where the temperature at the chip-tool interface is relatively low leading to fracture within the chip along a plane approximately at right angles to the shear plane [205], leaving behind a portion of the chip attached to the tool face [175]. This portion of the material will tend to grow and act as the cutting edge until it reaches a critical size then it will break and passes off with the chip. This portion of the chip is called a built-up-edge (BUE). The cyclic growth and fracture of the built-up-edge contribute to the variation of the depth of cut during machining, significantly affecting the machined surface roughness.

As the chip-tool temperature increases due to increasing the cutting speed, the BUE starts to decrease. The BUE disappears as a result of the lowered flow stress of the chip due to sufficient thermal softening at the chip-tool interface.

4.2.2.4 Type II Continuous Chip

Type II (*continuous*) chips occur when the flow of metal next to the tool face is not greatly restricted by a BUE or by friction at the chip-tool interface. Continuous chip occurs due to the ductile nature of the material which can shear out without rupture or fracture. Large rake angles and high cutting speeds promote continuous chips. Most early

analytical models relied on the classical ribbon like continuous chip formation. This is achieved by considering the primary shear zone (PSZ) as a constant plastic strain thin zone. As the cutting speed is reduced and the cutting tool edge becomes dull, the metal ahead of the cutting edge is compressed and due to frictional resistance to the flow of chip along the chip-tool interface small particles of the metal are formed as a built up edge. This built up edge eventually grows causing changes to the cutting edge geometry and the cutting process becomes unstable. Eventually, some fragments of the built up material are torn off causing accelerated wear and poor surface finish.

CHAPTER 5

Modeling of the Microstructure of Compacted Graphite Iron

5.1 Introduction

The following chapter presents the steps followed to model the microstructure of Compacted Graphite Iron (CGI). Throughout the modeling process, a number of challenging difficulties, tradeoffs, and assumptions will be addressed. In order to achieve a logical flow of work progress, it is more appropriate to address each difficulty, tradeoff, and assumption according to their nature in their specific relevant section.

Numerical methods, such as finite element method, are always the best resort when analytical methods fail or become inefficient. Based on that finite elements are mathematical domains rather than discrete physical regions of the continuum, and due to the absence of a unique modeling technique, several simplifying assumptions have to be introduced into each case to establish a “reasonable” approximation to the specific model foundation. The need for a degree of approximation is crucial to the meaningfulness of the model for several reasons. Firstly, the real world problem is usually too complex, if not impossible, to model its numerous interacting variables without running out of efficient analytical means or numeric resources. Secondly, in order to achieve meaningful and possible to analyze results, it is practically feasible to segregate the numerous volume

of output variables into a reasonable number of variables. However, in all cases, the degree of approximation must be realized and certainly understood during the modeling and eventually the analyses processes. In this work, every simplifying and/or approximating assumption will be reasoned, scrutinized, and ultimately justified where it is applied.

One major advantage of composites is that they are made to exhibit the best qualities of their constituents, if not sometimes exhibit qualities that neither constituent possesses alone. The presence of two distinct materials such as graphite and iron matrix in CGI, with the graphite particles embedded into the iron matrix, makes CGI conceptually a "natural" composite. It is a fact that the inaccuracy of a certain model is the natural outcome of the model's inaccurate consideration of its constituents. In order for the model of the microstructure of CGI to adequately represent the real material up to an acceptable extent of inaccuracy, feedbacks from the metallurgical investigations are employed along with the numerical modeling process.

Like in all composites, the mechanical (and physical) properties of CGI are definitely the product of the interacting mechanical (and physical) properties of the compound constituents. More specifically, three main constituents will have to be considered in this work due to their considerable presence in the real sample; pearlite, ferrite, and graphite. In order to successfully capture the effect of constituent, the complexity of each of the three constituents in the sample must be adequately considered and modeled.

5.2 Determination of Compacted Graphite Iron's model Constituents

A 2-D map of the three main constituents is generated after several CGI samples are prepared, polished, and etched with 2% *Nital* to reveal the ferrite and pearlite colonies in the metal. Careful polishing using wax instead of water is to be used to retain the graphite particles in place. Several graphite particles are found surrounded by either ferrite colonies or simply embedded in pearlite colonies recognized by their characteristic alternating cementite/ferrite lamellae as shown in **Figure 13**.

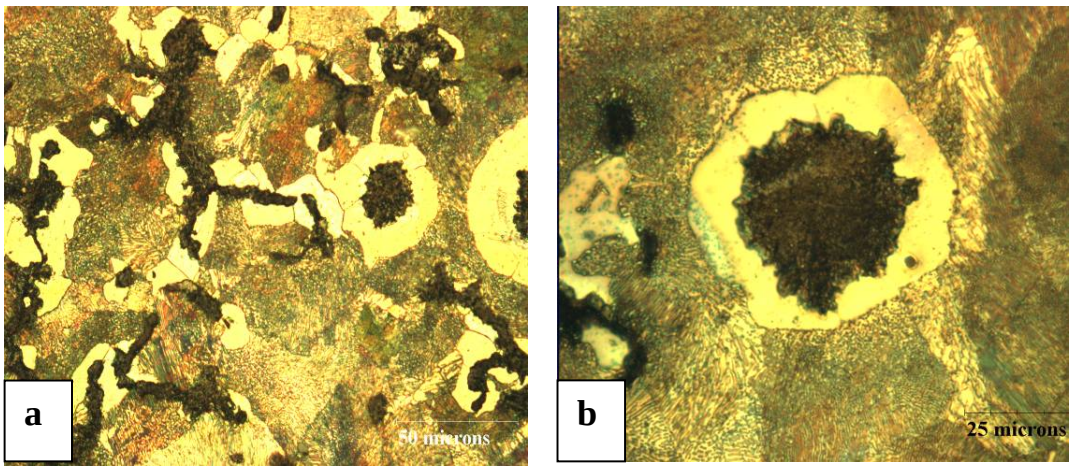

Figure 13 CGI's sample showing distribution of the three main constituents (a), Graphite particles surrounded with ferrite colony (b)

The images are then cleaned from irregularities such as sample scratches, irregular graphite sputters, and colors are enhanced to provide better visual using appropriate graphics software. The best image is then selected after many image quality-based filtering and is considered the representative volume element (RVE). Choice of the representative volume element is based on the area percentage average of each constitute and its clarity in the image. Calculation of the graphite area is performed before sample

etching with Nital to eliminate the effect of cementite dark lamellas on the calculation inaccuracy. Area percentages of graphite, ferrite, and pearlite are calculated to be 10%, 20%, and 70%, respectively. The representative volume element is then converted into standard ACIS Text (*.sat*) file format. The *.sat* file contains both graphite and matrix geometries.

Contours of the graphite particles are constructed as piece-wise splines. In other words, the model at this point contains two constituents only; graphite and the metal matrix. It is decided that the graphite phase geometries are the most vital component in the sample for two reasons. Firstly, the main reason for CGI's distinctive mechanical performance is basically referred to the graphite morphology. Secondly, is to capture the effect of the graphite morphology in CGI on the mechanism of damage during fracture and machining to a realistic extent without being drifted in to a study of such fictitious material. Accordingly, one contour file (*.sat* file) is loaded to Abaqus [206] representing the sample's geometry with vacancies in the matrix sketch. The contour file contains the metal matrix with vacancies (gaps) representing the graphite particles. This file, in fact, is the building block of the whole model.

Since graphite particles are present in the metal matrix in the form of gap fillers, the outer walls (boundaries) of the matrix sketch are then removed leading to a negative replica of the original matrix producing a sketch representing the graphite particles alone. Arbitrary colonies of the ferrite phase are next created in the matrix sketch after considering each constituent's calculated area to represent the final representative volume element (RVE), containing graphite, ferrite, and pearlite. The sketch is then converted into 2-D planar

deformable object. Finally, the constructed object is a replica of the compacted graphite iron sample and all existing graphite morphologies in 2-D plane are therefore conserved.

5.3 Heterogeneous Finite Element modeling of Compacted Graphite Iron

5.3.1 Modeling of Compacted Graphite Iron Constituents

Incorporation of the microstructure of different phases in the FE model requires sectioning of the overall model domain. This is achieved by the definition of sub-domains representing both ferrite and pearlite according to each area percentage within the sample image. Each sub-domain will be assigned its own material properties allowing it to deform accordingly. However, compatibility rules should be established among adjacent sub-domains to conserve the continuity of the whole matrix continuum. Sectioning does not conserve stress or strain continuities; however, it conserves force and displacement continuities to prevent continuum splitting (gapping). Based on the metallurgical investigations and absence of any practical finding to justify otherwise, separation between ferrite and pearlite will not be allowed. Accordingly, decohesion of the two constituents will merely be through failure of either constituent (or both). This will be elaborated on in the specific section.

Since graphite particles are merely the “fill ups” of the distributed vacancies in the matrix sketch, the negative replica of the matrix sketch constitutes the geometry of graphite particles, which are read by Abaqus as closed contours, and later are converted into objects of which Abaqus can recognize, as shown in **Figure 14**. No graphite particles are needed to be sectioned as they all have the same material properties. The assignment of

each constituent's mechanical (and physical) properties will be explained in more detail in the corresponding section to follow.

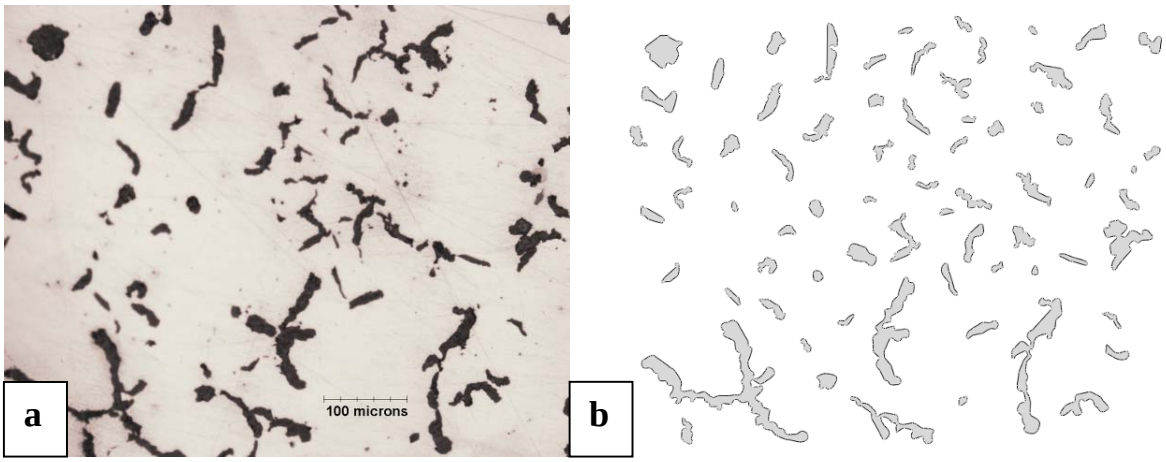

Figure 14 CGI's RVE optical microscope image (a), CGI's RVE graphite particles (negative replica of the left image (b)

5.3.2 Contact and Constraint Interactions

To model the separation action between graphite and the metal matrix, the two continuums are modeled as two separate parts. Parts in Abaqus are treated independently and interactions between them should be defined to prevent the penetration of one part into the other, and to establish the extent of possible interaction between the different parts. Each part's outer boundaries (surfaces) are defined using the command (*surface). In addition, definition of interactions between the different surfaces are established through either contact or constraint interaction. Contact interactions basically define how surfaces of different parts interact when they become in contact in regards to either transmission of forces and/or friction wise. On the other hand, constraint interactions define how different surfaces restrict the motion of each other. In this work, contact

interaction is used to define friction and pressure between meeting surfaces. Constraint interactions are used to "tie" the cohesive zone surface to the corresponding opposite continuum surface, as will be explained more in the next section. It is ultimately important to understand that careful handling of surface interaction should be maintained when working with surfaces of mismatching mesh densities and continuum densities. Modeling difficulties section will shed some lights on different issues concerning surface interaction definition and the "getting around" solutions performed in this work as will come later in this chapter.

5.3.3 Modeling the Graphite-Matrix Interface

Graphite-Matrix interface is modeled in the form of a cohesive zone using cohesive zone elements. Metallurgical investigation did not confirm the presence of any transitional region between the graphite particles and the metal matrix in the CGI sample. Accordingly, the interaction between the graphite particles and the surrounding matrix is considered to perform as a traction-separation interface with an infinitesimal thickness rather than a continuum. For this purpose, the cohesive zone elements are constructed of zero thickness series of elements (initially composed of two coinciding cohesive surfaces) inserted between the graphite and matrix surfaces, with each side tied to the opposite material surface. The two opposite surfaces of the cohesive elements are initially coincident in the unloaded state. When the cohesive element is loaded, its two opposite surfaces are separated and this relative separation creates normal and shear displacements which in turn generate stresses based on the element's constitutive equation. Accordingly, cohesive elements are able to transmit stresses in both directions (normal and shear)

according to a preset constitutive relation. The relative displacements (normal and shear) between the two opposite surfaces of the cohesive element/s represent the decohesion extent between graphite and the matrix continuums.

Decohesion between graphite and the matrix will go through three consecutive phases; hardening, maximum traction, and softening phases. When the cohesive zone is loaded, traction between the cohesive element two opposite surfaces will increase from zero to the maximum allowable strength to prevent element collapse (*decohesion*); hardening phase. With further loading, the cohesive zone's strength will reach a maximum that's specified in the cohesive zone model, representing an upper bound for the interface strength; maximum traction phase. Further straining of the cohesive zone will cause the stiffness to progressively degrade and opposite surfaces of the cohesive elements will further separate until complete separation occurs; softening phase. Failure of the cohesive elements will be reached once the specified maximum displacement is reached. The three phases are normalized and plotted in **Figure 15**.

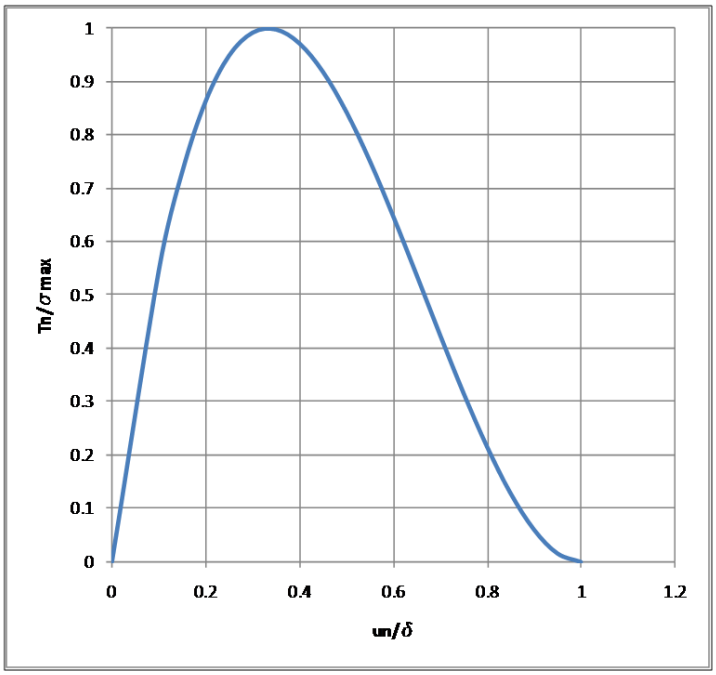

Figure 15 Graphite-matrix normalized normal traction decohesion model

The mechanical response of the cohesive zone is established through a constitutive model (in terms of a potential) that describes the dependency of the normal and tangential interface traction components ($\mathbf{T_n}$ & $\mathbf{T_t}$) between the graphite and the surrounding matrix, on the corresponding crack opening displacements u_n & u_t. The constitutive model does not describe any atomic interaction or discrete dislocation within the interface, and accordingly, the functional dependence of the traction field on the interface separation is not uniquely determined. The potential is expressed as:

$$\varphi(u_n, u_t) = -\int_0^u [\mathbf{T_n}\, du_n + \mathbf{T_t}\, du_t] \qquad (\mathbf{5.1})$$

The specific potential used to model the graphite-matrix decohesion is Needleman's model simplified for two-dimensional cohesive zone is as follows:

$$Q = \left[\frac{27}{4}\right] \sigma_{max} \delta_{max} \quad (\mathbf{5.2})$$

$$\varphi(u_n, u_t) = Q\left\{\frac{1}{2}\left(\frac{u_n}{\delta_{max}}\right)^2\left[1 - \frac{4}{3}\left(\frac{u_n}{\delta_{max}}\right) + \frac{1}{2}\left(\frac{u_n}{\delta_{max}}\right)^2\right] + \frac{1}{2}\alpha\left(\frac{u_t}{\delta_{max}}\right)^2\left[1 - 2\left(\frac{u_n}{\delta_{max}}\right) + \left(\frac{u_n}{\delta_{max}}\right)^2\right]\right\} \quad (\mathbf{5.3})$$

The above potential is chosen for analytical convenience and to prevent sudden drop in the traction-displacement behavior which may cause instability in the simulation.

As shown in equations **(5.2-5.3)**, modeling graphite-matrix decohesion is based on three quantities; the maximum interface strength (σ_{max}), maximum decohesion displacement (δ_{max}), and the ratio between the normal to tangential traction forces of the interface (α).

Based on comprehensive metallurgical investigations, no specific domination of failure in either graphite particles or matrix-graphite interface is present. Population of graphite-matrix decohesion is found to be as much as fractured graphite particles. Despite what precedes the other, both are generally equal in presence in the examined fractured surfaces. Accordingly, the interface strength over its boundaries will be considered as morphology dependent and the cohesion strength of the graphite-matrix interface would not exceed the least strong interface material; graphite. Based on that, the interface strength σ_{max} will be assumed equal to the graphite strength constituting the upper bound limit.

Based on comprehensive investigations of several interfaces and inter-graphite cracks performed in this work, decohesion gaps (displacements) is found in the range of 0.002-0.005 mm, shown in **Figure 16**. In this work, a conservative methodology will be adopted and the modeled maximum decohesion displacement will be 0.002 mm.

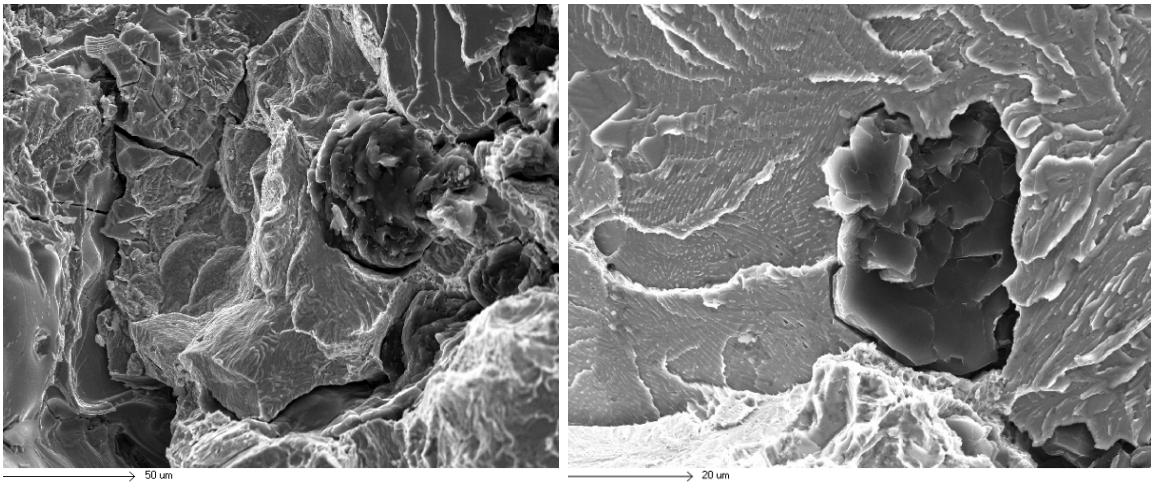

Figure 16 Graphite-matrix decohesion in a CGI sample

The third quantity to be determined; (α) represents the ratio of the shear stiffness to the normal stiffness at zero decohesion, which is set equal to unity, considering equal tractions in both directions. This assumption has been based on several literature sources, mentioned in the corresponding literature review chapter.

Damage is naturally an ongoing process rather than a sudden event in nature. In order to meaningfully model the process of damage, it must be broken up into stages. Each stage will have a scalar variable to determine when it commences and terminates. Modeling damage using cohesive elements in Abaqus is based on modeling of three stages; damage initiation stage, damage evolution stage, and the choice of element removal (or deletion) upon reaching a complete damage state. These three stages, in fact, correspond to the three decohesion phases mentioned previously.

Damage initiation refers to the beginning of degradation of the interface strength. Once damage initiation is reached, the traction-separation curve is irreversible and release of the applied load will not cause the element to retain its pre-damaged initiation

displacement. Numerically, damage initiation of the cohesive elements is judged when the scalar parameter (λ), expressed by the equation **(5.4)**, is equal to unity. Where $\varepsilon_{i=n,t}^{max}$ is the peak nominal strain when deformation is either purely normal or purely in the shear direction to the interface, respectively.

$$\lambda = \sqrt{\left\{\left(\frac{\varepsilon_n}{\varepsilon_n^{max}}\right)^2 + \left(\frac{\varepsilon_t}{\varepsilon_t^{max}}\right)^2\right\}} \tag{5.4}$$

The damage evolution criterion describes the rate at which the material stiffness is degraded once the above damage initiation phase is reached. Accordingly, damage will not evolve until the graphite-matrix interface reaches its peak strength. A scalar damage variable "*D*" represents the overall damage in the interface. The scalar damage evolution variable "*D*" monotonically evolves from 0 to 1 upon further loading after the initiation of damage. Complete separation occurs when the interface effective decohesion displacement reaches a critical value; fracture displacement. At this point both normal and tangential tractions will diminish and the cohesive element will no further be able to resist decohesion. The different effective displacements are calculated using the following equations:

$$\delta_{frac} = \sqrt{(\delta_n^2)_{max} + (\delta_t^2)_{max}} \tag{5.5}$$

$$\delta_{init} = \sqrt{(\delta_n^2)_{init} + (\delta_t^2)_{init}} \tag{5.6}$$

$$\delta_{eff} = \sqrt{u_n^2 + u_t^2} \tag{5.7}$$

The scalar damage variable "*D*" is expressed as:

$$D = 1 - \left[\frac{\delta_{init}}{\delta_{eff}}\right]\left\{1 - \frac{1 - e^{-\beta\left(\frac{\delta_{eff}-\delta_{init}}{\delta_{frac}-\delta_{init}}\right)}}{1 - e^{-\beta}}\right\} \tag{5.8}$$

Accordingly, both normal and tangential tractions are updated based on the following:

$$\begin{Bmatrix} T_n \\ T_t \end{Bmatrix} = \begin{Bmatrix} (1-D)t_n \\ (1-D)t_t \end{Bmatrix} \qquad D \geq 0 \tag{5.9}$$

$$\begin{Bmatrix} T_n \\ T_t \end{Bmatrix} = \begin{Bmatrix} t_n \\ t_t \end{Bmatrix} \qquad otherwise \tag{5.10}$$

Where $\bar{t}_n$ and $\bar{t}_t$ are the traction components in the normal and tangential directions of the graphite-matrix interface calculated at no damage. It is rather important to point out that the value of β in equation **(5.8)** is chosen to best describe the softening phase shown in **Figure 15**. Several iterative calculations are performed to choose the best value for the variable β. The best corresponding value used in this work is decided to be 1.5

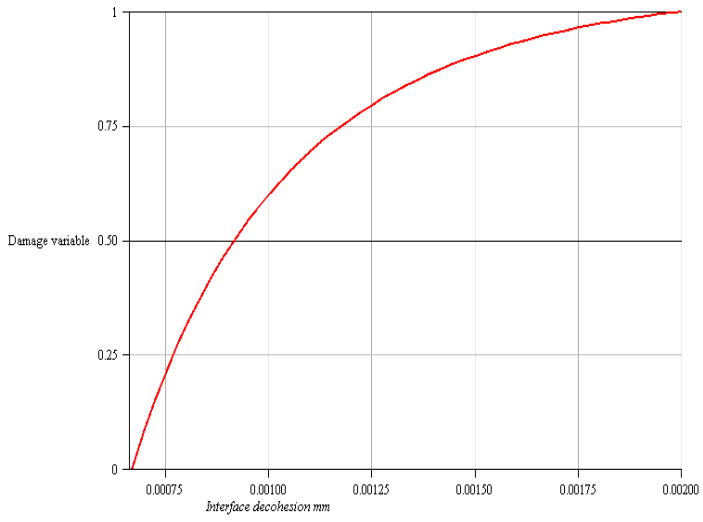

Figure 17 Damage evolution "*D*" vs. decohesion displacement

Once the scalar damage evolution variable *"D"* reaches unity, complete separation of the graphite-matrix interface is reached and element removal (deletion) is performed updating the interface traction to zero, i.e. the cohesive element's strength is set to zero.

Elements connectivity matrix is updated based on the elements removed. This is done automatically by Abaqus element deletion algorithm. However, two element deletion approaches are available in Abaqus. The first approach offers the damaged cohesive element to remain in the model even after the overall damage variable "*D*" is reached. In this case the stiffness of the element in tension (and in shear) remains constant (degraded by a factor of (*1–D)*). This choice is appropriate if the cohesive elements must resist interpenetration of the surrounding components after they completely degrade in either tension and/or shear. The second approach gives the ability of total removal of the damaged elements, which requires the definition of contact interaction between graphite and the matrix continuums to prevent interpenetration between continuums. The later approach is followed in the present work to have more control over the damage evolution process.

Abaqus two-dimensional cohesive element is assigned the name COH2D4. The cohesive element COH2D4 is a 2-dimensional 4-node element with two active degrees of freedom (x,y). Insertion of the cohesive elements into the model is done manually in the present work. Elements and nodes numbering must be carefully assigned to prevent later significant distortion error of elements during simulation. Node numbering follows a counter-clockwise scheme. Based on the direction of nodal numbering scheme, both

surfaces of the cohesive zone are decided. The illustration in **Figure 18** explains the node numbering scheme followed in this work and the corresponding surface designation. Element (I) consists of the nodal sequence (1, 2, 11, 10), element (II) consists of the nodal sequence (2, 3, 12, 11), etc.

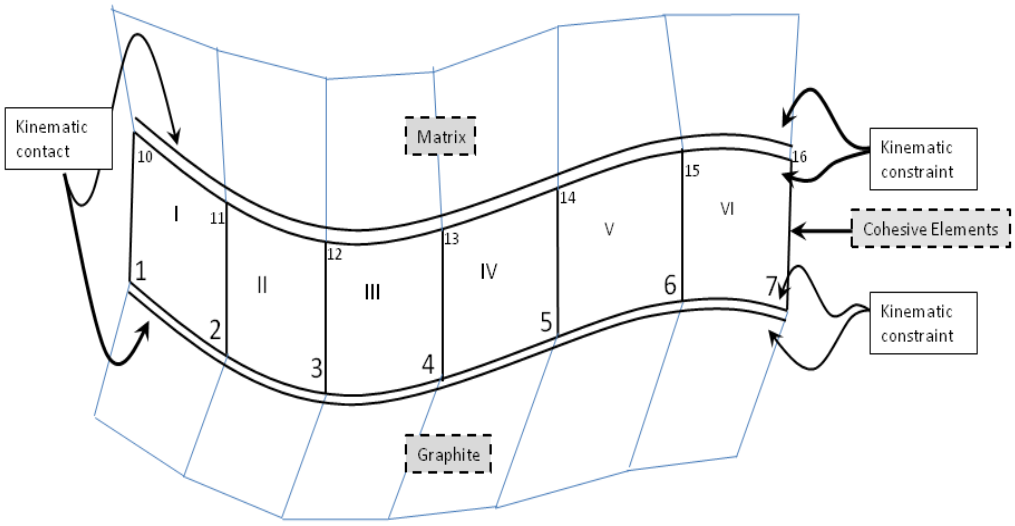

Figure 18 Node numbering scheme of cohesive zone elements

Based on this nodal scheme**,** each surface of the cohesive zone is uniquely determined. In order for the cohesive zone to function, each surface must be constrained to the opposite continuum using a kinematic constraint definition; TIE. This is done manually in the model's input file considering the corresponding surface designation. It is mandatory for the success of the cohesive zone performance to follow a careful node numbering. This is basically because both surfaces of the cohesive zone before loading coincide with each other and are zero distance apart. Inconsistency in the node numbering scheme will lead to incorrect tied surfaces leading to dysfunctional decohesion mechanism. It is important

to emphasize that **Figure 18** exaggerates the thickness of the cohesive zone for the sake of illustration only.

The cell shown in **Figure 19** is subjected to plain strain tension at side AB and explains the function of the cohesive zone elements. The cell is deformed in such a way where the straight edges surrounding it remain straight and the straight lines connecting the centers of the cells will remain straight. Seeking simplicity based on the symmetry of the cell in **Figure 19**, the boundary conditions on the cell quadrant will be as follows:

$$\dot{u}_x = 100\, m/min, \qquad u_y = 0 \qquad at\ x = \frac{L}{2} \tag{5.11}$$

$$\dot{u}_y = 0\, m/min, \qquad u_y = 0 \qquad at\ y = \frac{L}{2} \tag{5.12}$$

$$\dot{u}_x = 0\, m/min, \qquad u_x = 0 \qquad at\ x = 0 \tag{5.13}$$

$$\dot{u}_y = 0\, m/min, \qquad u_y = 0 \qquad at\ y = \frac{L}{2} \tag{5.14}$$

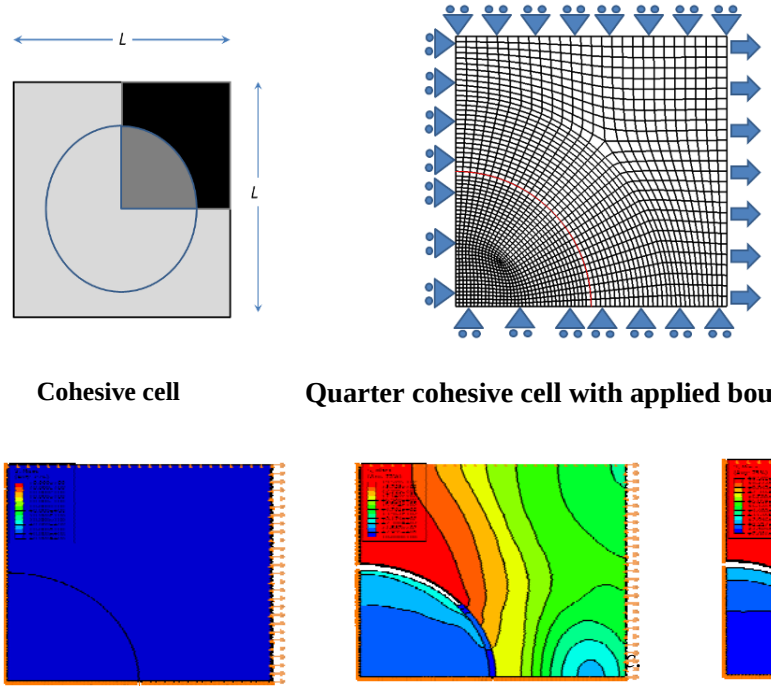

Cohesive cell **Quarter cohesive cell with applied boundary conditions**

Figure 19 Cohesive cell showing progressive decohesion during loading

According to the boundary conditions in equations **(5.11-14)**, the unit cell quarter will deform in the x direction. Side AB will exhibit a strain in the y direction that is equal to $(-\gamma\varepsilon_y)$, where γ is *Poisson*'s ratio. This will trigger the decohesion at point B first, until EF displacement reaches the damage evolution limit and exhibits a complete decohesion as shown at t=1.55E-5 sec. frame in **Figure 19** The *von Mises* contour lines in **Figure 19** validate the transmission of forces by the cohesive elements throughout the loading process.

5.3.4 Graphite-matrix modeling difficulties and solutions

As a zero thickness cohesion zone is inserted between the two continuums (graphite and matrix) to model the decohesion phenomenon, each side (surface) of the cohesive zone must be tied (constrained) to the corresponding facing continuum surface. This action constrains the motion of the two tied surface nodes up until the end of the simulation. Several types of kinematic constraints are available to use, however, in the present work "*Surface-based tie constraint*" is applied. In this type of constraint, each node on the first surface (called *salve*) will have the same values of degrees of freedom (in *x* and *y*) as the node on the second surface (called *master*) to which it is closest. However, failure and removal of the cohesive elements once decohesion is reached will require a contact interaction definition between the remaining continuums surfaces to prevent interpenetration which was originally prevented by the inter-continuums cohesive zone elements. The definition of contact interaction between the remaining continuums surfaces is called "*kinematic contact interaction*". Application of both kinematic constraint and kinematic contact interactions on the same node may result in a kinematic interaction conflict in the model. If a node that participates in a kinematic constraint is used in a kinematic contact interaction (which is the case in the present model), the kinematic contact constraint will most likely override the kinematic constraint interaction for a common degree of freedom of a certain node. Simply put as, the tie constraint will be overridden and the cohesive zone will separate from the adjacent continuum because the algorithm will have to decide on what degree of freedom value to choose from to

allocate to that node's degree of freedom. By default the algorithm will prefer kinematic contact over kinematic constraint interaction to resolve the conflict [206].

To prevent this drawback, a penalty contact algorithm is used, which introduces numerical softening which will prevent interference with the kinematic tie constraint [206]. The penalties are basically weighted based on the masses of the nodes participating in the multiple constraints. This proposed penalty will create a very small incompliance in the constraint and penetration of the slave surface nodes into the master surface may occur. However, this very small incompliance will be of minimal significance by using the pure master-slave algorithm with the master surface containing the more massive nodes (the matrix).

5.3.5 Modeling of the compacted graphite iron matrix

Modeling the mechanical properties of each matrix constituent in the present work (pearlite & ferrite) is performed using the rate dependent Johnson-Cook (JC) model, previously described in the literature review. Each constituent is modeled as an isotropic material. As mentioned before, the Johnson-Cook (JC) model is a strain rate, temperature dependent, viscoplastic material model for problems where strain rates vary over a large range (10^2 - 10^6 s^{-1}). The flow stress is a function of the plastic strain (ε^p), the strain rate ($\dot{\varepsilon}^p$), normalized by the reference strain rate ($\dot{\varepsilon_o}$). The model uses the following form:

$$\sigma = \left[A + B\left(\varepsilon_p\right)^n\right]\left[1 + Cln\left(\frac{\dot{\varepsilon}_p}{\dot{\varepsilon_o}}\right)\right]\left[1 - \left(\frac{T - T_{room}}{T_{melt} - T_{room}}\right)^m\right] \tag{5.15}$$

In the above equation, the first bracket represents the elastic-plastic behavior, the second

bracket represents the effect of strain rate, and the third bracket represents the thermal softening effect. Here A, B, n, C, and m are material constants determined by either the high strain rate Split Hopkinson Pressure (or shear) bar test as commonly done, or the application of cutting test.

In the case of a conventional homogenous material, one set of material constants is determined considering a single phase presence. However, in the present heterogeneous microstructure case, each constituent will have its own set of material constants. Considering the two main metal matrix constituents (ferrite and pearlite) in the present work, each constituent will have a separate set of material constants.

Simoneau et al. proposed material constant for pearlite and ferrite from cutting tests of normalized 1045 steel and by using a developed quasi-dynamic flow stress model [207]. The calculated constants were in good agreement with those determined by Jaspers et al. [208]. Preference will be granted to Simoneau's material constants over Jaspers constants. The reason for the preference is that Simoneau's strain and strain rate ranges were closer to the present work ranges of strain and strain rate ranges. Johnson-Cook material constants are valid only over certain strain and strain rate ranges. The strain range of $0.8 < \varepsilon \leq 7.2$ and strain rate range of $10^4 < \dot{\varepsilon} \leq 10^6$ are more practical when cutting at speeds of 100, 200, and 400 m/min. in the present work. The determined material constants by Simoneau are used for modeling the pearlite constituent. However, the Johnson-Cook ferrite constants are scaled down pearlite constants based on that each pearlite grain in will plastically constrain the ferrite grains during deformation and that will increase the strength of the soft ferrite grains, compared to pure ferrite grains under

metal cutting conditions. Considering the ability of sectioning the model into pearlite and ferrite sections with each section assigned their particular mechanical and physical properties, each matrix constituent is assigned the appropriate Johnson-Cook material model set of constants. **Table 15** provides the Johnson-Cook (JC) pearlite and ferrite constants used in the present work:

Table 15 Johnson-Cook model matrix material constants

Material	A (MPa)	B (MPa)	C	n	m
Pearlite	550	600.8	0.035	0.54	0.937
Ferrite	190	600.8	0.012	0.18	0.937

Scaling down of the ferrite Johnson-Cook model material constants is based on the rationale proposed by Simoneau et al. [207].

To account for fracture of the metal matrix, a cumulative damage model is used. The cumulative strain damage model assumes that damage toward fracture is due to the accumulated plastic deformations of the material. Accordingly, fracture occurs when the accumulated damage exceeds (or at least reaches) a material critical value; D_c, expressed as:

$$D \geq D_c \tag{5.16}$$

The above expression can be put in the form of a normalized compact expression such that damage occurs when the critical damage value is equal to unity:

$$D = \int_0^{\bar{\varepsilon}_c} f(\text{stress state})\, d\bar{\varepsilon} = 1 \tag{5.17}$$

where f is a history dependent damage function, $\bar{\varepsilon}$ is the equivalent strain, $\bar{\varepsilon}_c$ is the equivalent plastic critical strain at fracture. For the above expression to account for the stress, strain rate, temperature, and strain, the stress state integrand is expressed as follows:

$$D = \int_0^{\bar{\varepsilon}_c} f\left(\sigma, \varepsilon_f, \dot{\varepsilon}, T\right) d\bar{\varepsilon} = 1 \tag{5.18}$$

Johnson-Cook's failure model considers the effect of three quantities; triaxiality, strain rate, and temperature. The Johnson-Cook's fracture criterion is expressed in terms of the strain-to-fracture model:

$$D = \int_0^{\bar{\varepsilon}_c} f(\sigma, \varepsilon, \dot{\varepsilon}, T) d\bar{\varepsilon} = \int_0^{\bar{\varepsilon}_f} \frac{1}{\bar{\varepsilon}} d\bar{\varepsilon} \tag{5.19}$$

where the plastic strain-to-fracture is expressed as:

$$\varepsilon_f = \left[d_1 + d_2\, exp\left(d_3\, \frac{\sigma_m}{\sigma_{eq}}\right)\right]\left[1 + d_4 \log\left(\frac{\dot{\varepsilon}_p}{\dot{\varepsilon}_0}\right)\right]\left[1 + d_5\, \left(\frac{T - T_0}{T_{melt} - T_0}\right)\right] \tag{5.20}$$

where $\sigma_1, \sigma_2, \& \sigma_3$ are the principal stresses, and σ_m is the hydrostatic stress. The *von Mises* equivalent stress is expressed as:

$$\sigma_{eq} = \sqrt{\frac{1}{2}[(\sigma_1 - \sigma_2)^2 + (\sigma_2 - \sigma_3)^2 + (\sigma_3 - \sigma_1)^2]} \tag{5.21}$$

where $d_1 \ldots d_5$ are material constants. The first three constants (d_1, d_2, d_3) determine the effect of the hydrostatic stress to *von Mises* stress ratio on the fracture strain for quasi-static conditions. The fourth constant (d_4) determines the effect of the strain rate, and the fifth constant (d_5) determines the effect of temperature, on the fracture strain, respectively. The Johnson-Cook material damage constants are listed in the table below [209]:

Johnson-Cook Material Damage Constants	d_1	d_2	d_3	d_4	d_5
	0.05	4.22	-2.73	0.0018	0.55

Table 16 Johnson-Cook Material Damage Constants

5.4 Compacted Graphite Iron in Fracture and Machining

In order to successfully model compacted graphite iron in machining, it is crucially important to proceed according to a scientifically feasible plan. The purpose of the fracture model is firstly; to establish a foundation of a microstructure modeling technique which will serve as a foundation to model CGI in machining. As machining can be merely explained as a controlled fracture process, fracture model investigates and simulates the initiation and propagation of cracks in compacted graphite iron. The methodology of modeling machining processes in pursue of optimization without fully

understanding the mechanics of material fracture is by far similar to pursuing optimization through trial and error. It is not to rush into a conclusion, however, as will be seen afterwards that crack initiation and propagation throughout the CGI sample in machining is a major source of chip characteristics. Therefore, understanding the mechanism of crack initiation and propagation in CGI will ultimately shed a lot of light on the mechanics of CGI in machining. A second reason that is as important as of why use a fracture model to begin with, is the complex nature of machining modeling as it will certainly involve a numerous number of interacting and conflicting variables that will first need to be scrutinized in a less complex model. Following this modeling methodology will guarantee a more scientifically viable procedure.

5.4.1 Compacted Graphite Iron Model in Fracture

The main objectives of this model are to investigate and elucidate the initiation and propagation of cracks in compacted graphite iron (CGI) microstructure and to numerically investigate areas where crack initiation and propagation are more of favor to exist. As most fracture investigations are based on after-the-event findings, finite element simulation of the fracture of CGI will simulate the fracture initiation and propagation processes from initiation until failure. This will establish better understanding of the cracking mechanism in CGI and elucidate the failure phenomenon. Specific attention will be directed toward the analysis of the equivalent *von Mises* stress and to the maximum principal stresses as the bases of the presently applied damage mechanism.

It is imperative at this point to highlight the methodology pursued to successfully model

CGI. Neither numerical modeling nor experimental work is intended to perform as a stand-alone player in the present work. The methodology followed in this work is based on mutually cooperative and iterative interactions between the experimental metallurgical investigations of CGI and the finite element modeling and simulation technique. Several finite element modeling inputs are extracted from metallurgical findings. On the other hand, finite element simulation's results are, as well, been validated by experimental investigations.

Following the modeling procedure mentioned above in converting the material constituents images into splines and loading the splines into Abaqus, both metal matrix constituents (ferrite and pearlite) and the graphite particles are meshed with CPE4RT elements; 4-node bilinear displacement and temperature, reduced integration with hourglass control elements. Denser mesh surrounding the graphite particles are implemented (0.0025mm.) with less dense mesh at the model boundaries (0.006 mm.). Abrupt variation in mesh size is prevented to eliminate inconsistency and to maintain a smooth stress flow and temperature gradients. Several runs are tested to achieve best element size for the present model. The size of elements to map the graphite particles and the irregular graphite/matrix interface must be as small as numerically reasonable (0.0025 mm.) to accurately represent the graphite particles without causing convergence instability in the FE simulation. Too small of an element size may lead to an increased number of elements within the model leading to extended computational time and elevated computational resources costs. More specifically, as explicit central-difference time integration rule is used in explicit dynamic analysis, the stable time increment

depends on the length of the smallest element in the model, therefore extending the computational time. To avoid integration over larger elements using very small time increments, selective subcycling technique is used. Selective subcycling allows different time increments to be used for different groups of elements. Accordingly, smaller elements needed to define graphite particles contours will not significantly control the overall model's stable time increment. The subcycling domain is defined manually and integrated using a smaller time increment. The selective subcycling decomposes the domain into parallel domains where each subdomain will be integrated using a suitable stable time increment decided automatically by Abaqus. On the other hand, the non-subcycling domain is integrated using the largest stable time increment. Hence, subcycling leads to a better simulation time increment management with sufficient accuracy.

The model deformation is simulated considering it within the bulk of the sample, as shown in **Figure 20**, by applying the appropriate boundary conditions. The model is simulated at strain rate 1.7e+5 sec^{-1}. Considering the symmetry of the test sample, for simplicity one-half of the test sample middle section is meshed and simulated. The total number of elements used in the model was 13551 CPE4RT elements. Simulations were run on a Dell™ OPTIPLEX GX270™ Inter® with a Pentium® 4 CPU 3.0 GHz processor and 3.62 GB of RAM. One important modeling consideration is that the size of the model should match the material's microstructure size in order to maintain accurate force and displacement readings, i.e. in millimeters. Since units in Abaqus are user defined, the sample size is modeled in millimeters and the material properties are defined in SI units

(small loads). Accordingly, the basic dimensions will be *mm*, *Newton*, and *seconds* for length, force, and time, respectively.

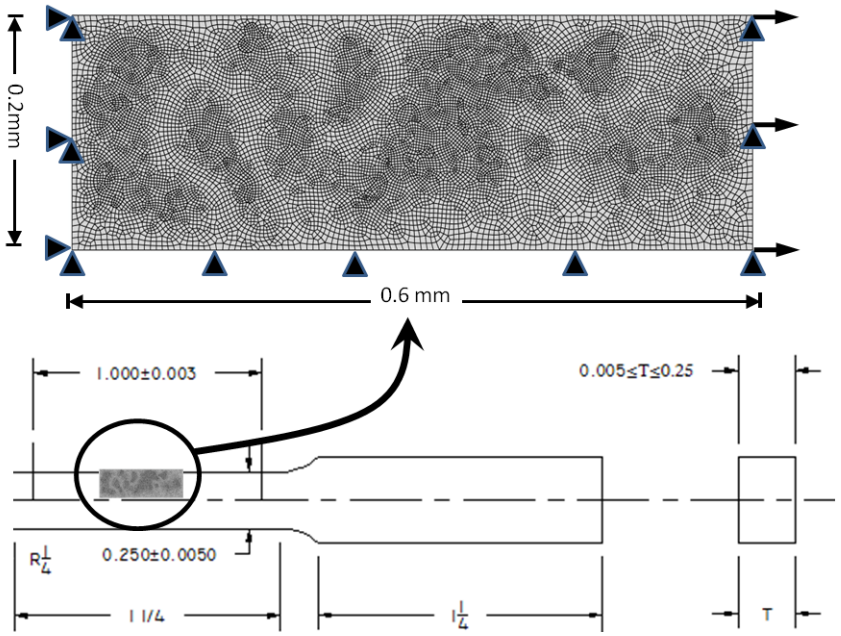

Figure 20 CGI fracture model under appropriate boundary conditions

5.4.2 Compacted Graphite Iron Model in Machining

As previously emphasized, modeling of compacted graphite iron in fracture will serve as a foundation to the machining model. More attention is awarded to the chip microstructure in the present work. No pearlite, ferrite, or graphite is added to the base of the work piece so to confine the scope of work to CGI's chip formation. In addition, this later procedure optimizes the processing time of the simulation to a significant extent. However, in addition to the modeling complexity of the workpiece microstructure, other modeling issues should be addressed at this point. Such issues are: chip separation criterion, chip-tool interaction, friction, machined workpiece surface and tool interaction,

boundary conditions, and constraints conflicts and their solutions. Each modeling difficulty will be exposed in more detail in the next sections.

The compacted graphite iron machining model setup is based on the orthogonal machining configuration. Despite that orthogonal machining comprises a special machining configuration that is not commonly used in real cutting, though, it is one simple machining configuration which can provide a significant set of helpful findings, and can be experimentally set up for verification purpose.

Regardless of the shape of the cutting tool, its action is always related to the relatively simple configuration of orthogonal cutting. Orthogonal cutting is based on a number of specifications among which the flow of chip should be perpendicular to the cutting tool edge plane. No angular chip flow is allowed. In addition, the width of the cutting edge should exceed the width of the chip, and the uncut chip thickness should be at least one-twentieth of the chip width to minimize the effect of transversal flow of the material during machining [210]. In this case the flow, in general, takes place in planes perpendicular to the workpiece surface and parallel to the direction of cutting. To summarize, orthogonal cutting is a good plane strain modeling case. Accordingly, the finite element machining model of CGI is based on a plane strain element formulation, where the material is free to strain in one plane and minimal strain is allowed perpendicular to that plane. The workpiece is constrained only at its bottom end in both vertical and horizontal directions. The cutting tool is placed at one side with its tip shifted down the top of the work piece as far as the uncut chip thickness is. The cutting tool is constrained at its back side in both vertical and horizontal directions. However, the

cutting tool is allowed to move against the workpiece to produce the cutting action according to the prescribed cutting speed.

Both cutting insert and workpiece parts are modeled as deformable parts to as closely as possible simulate the real cutting parts. No rigid part is introduced in the machining model. The mechanical and physical properties of the cutting insert are listed in **Table 17**. Specific mechanical and physical properties are received through direct communication with Kennametal Inc. The cutting insert is modeled based on the effective geometric configuration of the real cutting insert. Considering a very short machining test (5 seconds/insert/cut), the cutting insert is modeled with a sharp tip. Despite that in real cutting the cutting insert will lose its sharp tip during the first few milliseconds of operation, the cutting force measurements are always taken within the first few milliseconds of engagement. It is generally admitted that the simulated cutting forces will always be lower than the measured forces, even within the first milliseconds of operation. However, a variation of 10-15% in the simulated cutting forces is reasonably accepted and considered representative.

Table 17 Cutting insert specifications used in all simulations and experimental measurements

Kennametal TPG 432 – Grade 68[16]			
Young's modulus (GPa)	534	*Rake angle*	5^o
Poisson ratio	0.22	*Clearance angle*	6^o
Density (Kg/m^3)	14900	*Approach angle*	0^o
Specific Heat	250	*Chip breaker*	None
Thermal Conductivity (W/mK)	85		

Nine finite element simulations are run in the present work. Three cutting speeds 100, 200, and 400 m/min per three uncut chip thicknesses (feed rates) 0.05, 0.1, and 0.2 mm/rev. Results of the nine finite element simulations will be presented in the corresponding chapter. Modification of the cutting model is made each time the uncut chip thickness (feed rate) is changed to represent the correct damageable chip region. However, changing the cutting speed does not require any modification to the cutting model, except the cutting speed input and the corresponding time of simulation. The machining finite element models are shown in **Figure 21** and **Figure 22** for three feed rates (0.05, 0.1, 0.2 mm/rev.)

[16] Composition: Hard, low binder content, unalloyed WC/Co fine-grained grade. Recommended by Kennametal for machining; titanium, cast irons, austenitic stainless steels, non-ferrous metals, non-metals, and most high-temperature alloys.

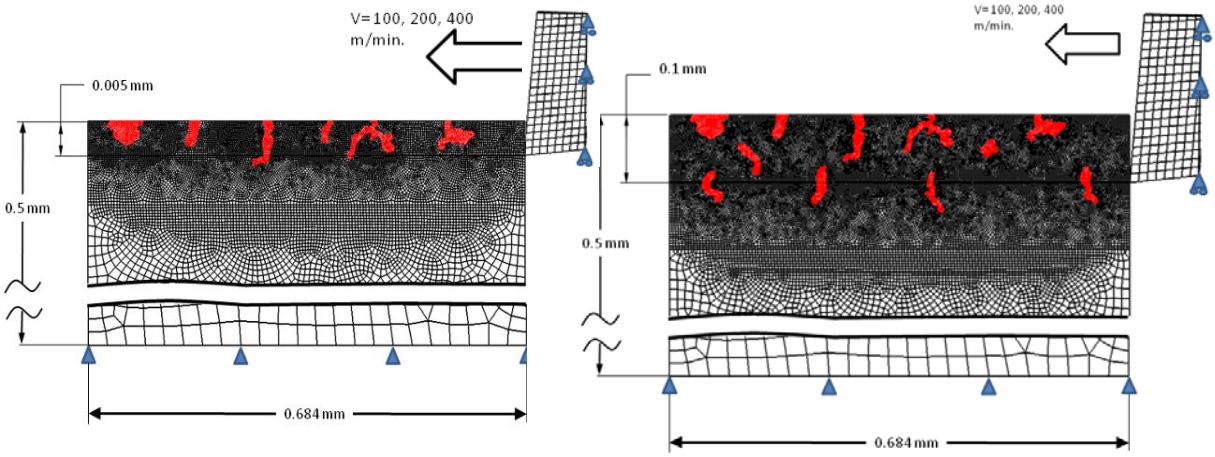

Figure 21 Finite element model of CGI in machining (0.05, 0.1 mm/rev.)

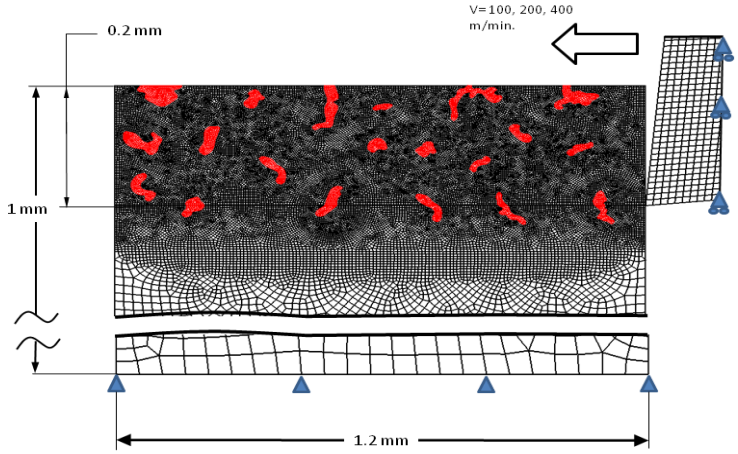

Figure 22 Finite element model of CGI in machining (0.2 mm/rev.)

The size of the 0.2 mm/rev. is changed to 1.2 mm long by 1 mm high to insure plane strain conditions. It is customary that the ratio of uncut chip thickness to the workpiece height not to be less than one-fifth in similar simulations. Any deformation in the end side of the workpiece before complete chip separation should trigger an increase in the

workpiece height to maintain plane strain condition throughout the simulation.

Four-node plane strain thermally coupled quadrilateral, bilinear displacement, reduced integration with hourglass control elements (CPE4RT) are used to model the workpiece (pearlite, ferrite, and graphite constituents) for 0.05, 0.1, and 0.2 mm/rev. feed rates using 13353, 19193, and 28285 elements, respectively. On the other hand, 504 four-node plane strain, thermally coupled quadrilateral, bilinear displacement, reduced integration with hourglass control element are used to mesh the cutting insert.

5.4.2.1 Machining Model Challenges

Primary machining tests of compacted graphite iron show discontinuous chip characteristics in all machining scenarios. Careful investigation of CGI's machined chip at high magnification shows segmental characteristics as will be further explained in the experimental work chapter. Accordingly, in order to successfully introduce the discontinuity in CGI's chip, the finite element *Lagrangian formulation* is applied.

In the finite element Lagrangian formulation, the mesh covers the exact geometry of the simulated material and the mesh nodes are attached to the material points throughout the simulation life. Since the mesh nodes are coincident with the material points, boundary nodes will remain on the boundary throughout the evolution of the simulation. This will simplify the imposition of boundary conditions; however, will require finer elements size to prevent significant element distortion due to the severe deformation of the mesh throughout the simulation as a result of the high strain magnitudes exist in machining processes.

5.4.2.2 The Chip Separation Criterion

In most machining simulations where the Lagrangian formulation is employed, a need for chip separation criterion is essential to prevent interruption of computation due to severe deformation of the mesh elements. Chip separation techniques basically function as the modeling tool required to separate the chip mesh from the rest of the model by deleting specific elements and creating substitutive nodes replacing the deleted nodes according to preset rules. Chip separation criteria are generally divided into two techniques; geometrical and physical techniques. In this work, the choice of a physical criterion is employed in order to closely represent the physics of the material behavior ahead of the cutting tool tip.

In finite element machining simulations where continuous chip is modeled, a set of elements is considered for deletion in priori according to a chip separation criterion. In a typical simulation, the chip region bottom surface is defined using a set of elements which comprise the bottom boundaries of the chip. As the cutting insert proceeds into the workpiece material pushing the uncut chip material away from the rest of the workpiece body, the chip material starts to bulge (strain) in front of the tool rake surface until it reaches its fracture strain. Further advancement of the cutting insert will force the chip material to separate and the predefined bottom surface of the chip will slide over the cutting insert rake surface according to the defined friction contact interaction. This technique is widely common and duplicated in all continuous chip simulations regardless of the chip separation criterion. Unlike in continuous chip simulations, in CGI's machining it is impossible to know the chip shape in priori. Compacted graphite iron chip

segments will form according to where crack initiation and propagation will evolve based on the driving fracture conditions; stress, strain, strain rate, and temperature. Determining the chip segment shape in priori will defeat the purpose of the simulation and will render the whole simulation unrealistic. Based on the aforementioned, material fracture should be let occur at any location in the chip region without prejudice to specific microstructural configuration or location.

To achieve the previous requirement of not predefining a unique chip surface to slide over the insert rake surface, the whole chip region should be able to act as stand-by surfaces. Simply put as whenever there is a need for a new chip slide surface, there should exist one without terminating the simulation and redefining a new one. Application of such technique requires the availability of a new surface every time the previous chip segment is separated from the material. Surface definition in Abaqus is classified as either element or node based surfaces. Node-based surfaces use a set of nodes where each node set represents a surface as shown in **Figure 23**. Node-based surfaces are by definition discontinuous where each node set acts as an independent slave surface. Unlike element-based surfaces, it is possible to break the node-based surface without collapsing the whole surface based on its discontinuity feature. However, contact definition between node-based surfaces is not allowed and is considered trivial. Node-based surfaces are defined using the *SURFACE, Type=Node" command.

One deficiency of the node-based surface is its inefficient contact interaction which may result in its penetration into other surfaces if used as a master surface in a contact pair interaction. This can be resolved by allocating it as a slave surface throughout the

simulation and meshing it with finer elements compared to the cutting insert rake surface (master).

Crack initiation and propagation in CGI's chip area will be determined according to the effective plastic strain relative to the critical fracture strain in Johnson-Cook damage model. The critical fracture strain in Johnson-Cook model is dependent on the plastic strain, hydrostatic stress, temperature, and strain rate, as previously mentioned in the matrix damage modeling section. To allow cracks to initiate at any point where the effective plastic strain exceeds Johnson-Cook critical fracture strain, all the chip region is left vulnerable to crack initiation. Johnson-Cook damage model is shown in equation **(20)** and the model constants are listed in **Table 16.**

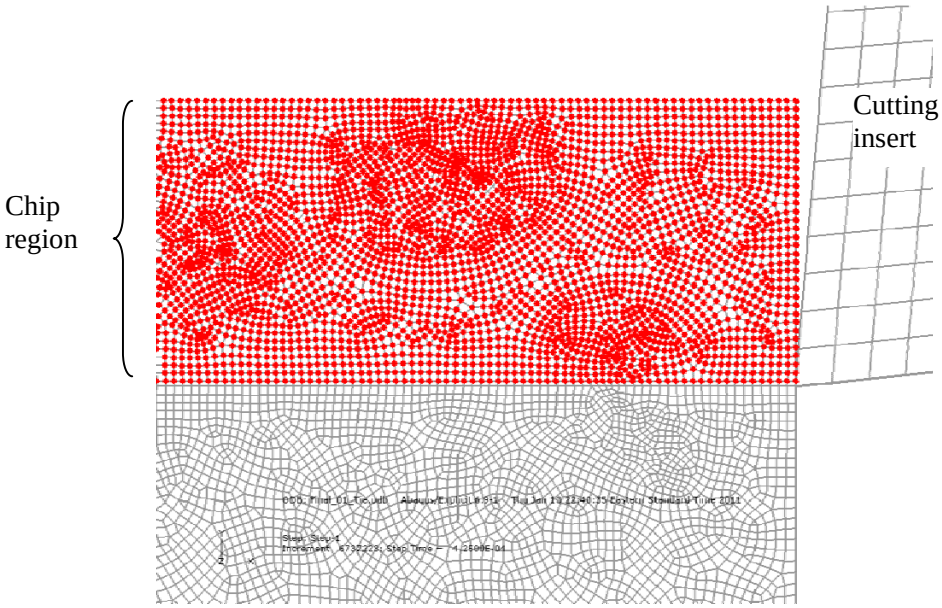

Figure 23 CGI chip node-based surface

Accordingly, crack initiation and propagation will have the freedom to occur anywhere in the chip region, including the graphite, pearlite, ferrite, and the cohesive elements. This is

not just how chip segments occur in real CGI machining; rather, it is how chip is formed in any machining process as will be seen later in this section when the present technique is applied on a different material.

5.4.2.3 The Chip-Tool Interaction

The cutting insert rake surface and the clearance surface are defined as element-based surfaces. Element-based surfaces are continuous surfaces and may not be discontinued before or during the simulation. They are able to transmit contact stresses and temperature more effectively than node-based surfaces. Element-based surfaces are can be used as master or slave surfaces. To create an element based surface, the command "*SURFACE, Type=Element" is used. In a situation where there are two surfaces in contact (slave and master surfaces), the master surface must have the higher material density to prevent contact noise and interpenetration. It is worth mentioning at this point that when the two surfaces in contact have a significant difference (several folds) in their densities such as the matrix and cutting insert, the master surface element size must be as many folds bigger as the slave's element size to prevent numerical oscillation during solution. In this case, the matrix element size is 0.0025 mm. and the insert element size is modeled 0.013mm.

Interaction among the chip node-based surfaces and the cutting insert rake surface is defined using kinematic interaction with friction equals to 0.1. Excluded from the kinematic interaction definition used for all the chip region nodes are the nodes used to tie both the matrix and the graphite regions to the corresponding cohesive nodes. The nodes on **Figure 24(b)** have been defined using penalty interaction definition which is less

stringent than kinematic interaction definition used for the rest of the chip region nodes **Figure 24(a)**. The reason for that is to prevent constraint definitions (tie constraint) from being over-ridden by the contact interaction applied between the chip and the cutting insert.

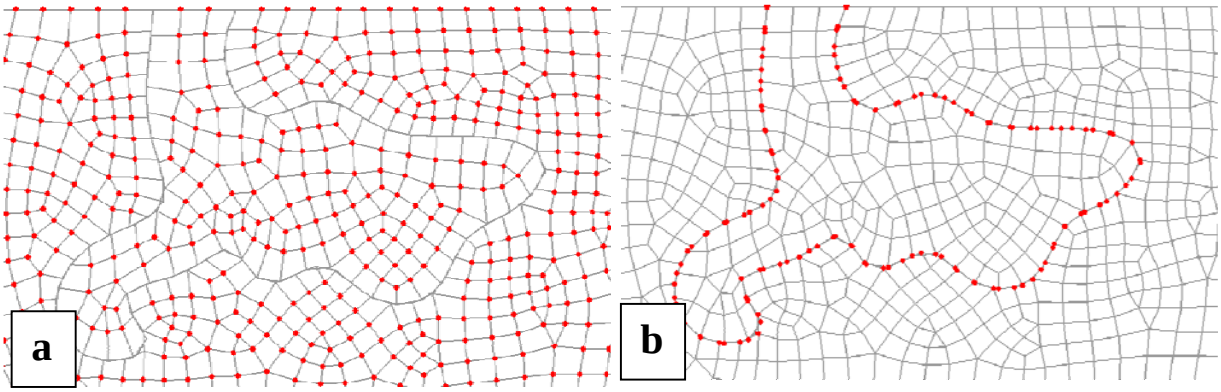

Figure 24 Graphite-Matrix nodes used to tie with the inter-cohesive nodes (a) included in a penalty contact interaction definition to prevent their constraint definition from being overridden by the kinematic contact definitions applied to other node-based surface nodes (b).

In other words, to prevent the tied cohesive zone from losing its cohesion with the graphite continuum and the matrix continuum in case there is a common degree of freedom at any time during the simulation. A simple explanation to this scenario is that a degree of freedom value is specified to the surface nodes in contact based on their deformation, if there is another constraint applied on these specific nodes another degree of freedom value will have to be specified to these same nodes by the algorithm. To resolve this conflict if present, kinematic contact degrees of freedom are by default given preference over constraint degree of freedom which simply loses the constraint

interaction (tie). Using the penalty interaction, which is less stringent than the kinematic interaction to specify a contact definition, will provide more flexibility to the contact interaction for these specific nodes without losing the constraint definition (tie). This technique is used in the simulation for the aforementioned rationale.

The workpiece finished surface is defined as an element-based surface. Kinematic contact interaction is defined between the element-based finished workpiece surface and the element-based cutting tool clearance surface with friction 0.1. The need for such definition will prevent a the cutting insert from penetrating the finished workpiece surface which may give trivial thrust force calculation and will provide a more accurate calculated cutting tool force.

5.5 The Graphite-Free Model

The purpose of this model is merely to use it for the validation of the applicability of the present CGI model on other materials by comparing the resulting chip characteristics generated to the chip characteristics generated in a previous work AISI 1045 presented by *Simoneau* [207]. It is not to presume that the simulated model accurately represents the composition of AISI 1045 used in *Simoneau*'s work, however, this so called no-graphite model represents the main characteristics of *Simoneau*'s material and may be considered a reasonable approximation of the real AISI 1045 material.

As the AISI 1045 material does not have the carbon element in the form of graphite as the case in cast iron, the graphite contours in the CGI model should be removed and replaced by ferrite regions. This is done in the model and the new model will contain only ferrite

and pearlite. However, it is important to emphasize on that the whole chip region is still vulnerable to crack initiation and propagation. Obviously, the cohesive zone strength should be modified to the strength of the ferrite constituent and the model will represent a no-graphite material. The graphite-free model mesh will match the mesh of the proposed CGI model mesh, however, all pertaining results will be presented in the results and discussions chapter.

CHAPTER 6

Experimental Work

6.1 Introduction

One aim of the current work is to model the microstructure of compacted graphite iron. Such aim should first be scrutinized and validated for credibility. In addition and for the purpose of practicality, this model should be applicable to an industrial problem of considerable importance.

The worthiness of adopting CGI in designing automotive and locomotive components is contingent upon its application and manufacturing comparability to the currently used materials. Accordingly, both fracture and machining of CGI are the two challenging venues to CGI's application in the industry and the effort of the present work will be directed toward these two venues.

6.2 Workpiece Preparation and Testing in fracture

6.2.1 Mechanical Testing Procedures

The studied compacted graphite iron samples are initially designed as cylinder liners for the heavy duty Hummer SUV. Twelve tensile test samples are machined after ASTM-E8 standards [211] as shown in **Figure 25**. Tensile tests are carried out at controlled 0.1 mm/min elongation rate to determine the material tensile strength, fracture stress, and maximum strain. The true stress-strain curve is calculated and graphed as will be shown

in the Results and Discussion chapter. Tensile tests are carried out on a MTS machine with self-aligning grips and 250 KN load cell.

To avoid limited elongation due to geometric instability in the tensile test, the shear test is also performed. The shear test sample is machined with short middle section span to ensure minimal possible bending in the test sample. The shear test is performed at controlled 0.1 mm/min elongation rate. The test sample is shown in **Figure 26**.

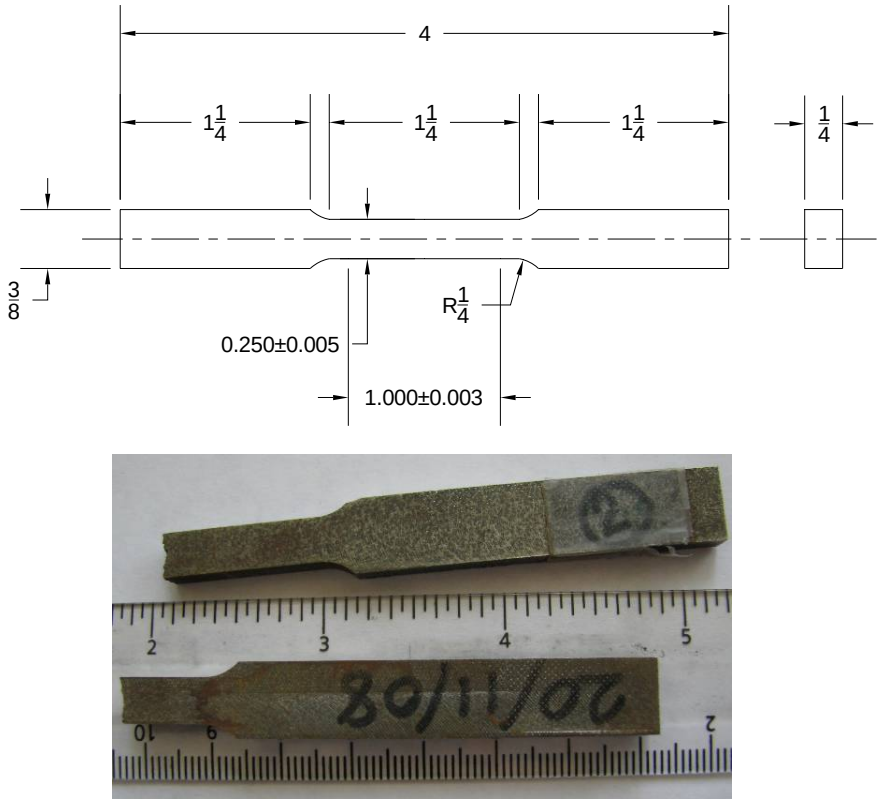

Figure 25 Tensile test specimen ASTM E8

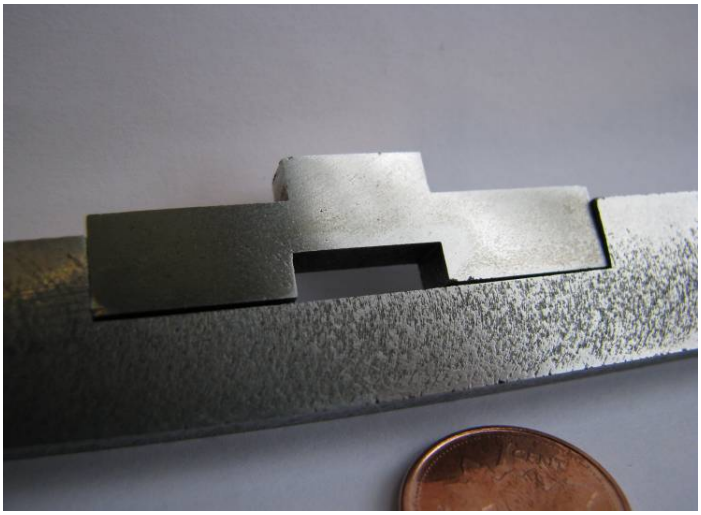

Figure 26 Shear test sample in the restraining block

Charpy impact test is carried out to study the fracture surface characteristics at high strain rate. The Charpy impact test specimen is machined after ASTM E23 standards “keyhole specimen”. The sample is shown in **Figure 27**.

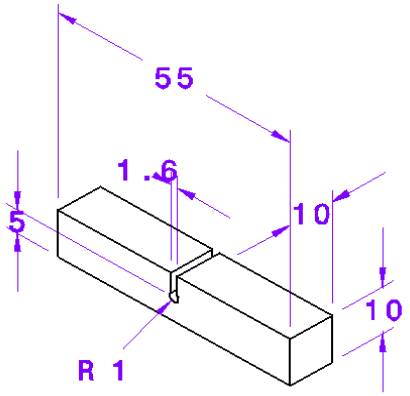

Figure 27 Charpy impact keyhole test sample sample sktech

The Charpy impact test sample fractured surface is examined using the Scanning Electron microscope (SEM) (JEOL 7000F) available at the Canadian Centre for Electron Microscopy-McMaster University, for high magnification details. The sample is cleaned

from dirt and oil contamination using alcohol and mounted on a clean stub using a silver paste adhesion for good connection and support. Several samples are tested to study the fracture mechanism and investigate the matrix graphite decohesion phenomenon. In addition, the matrix and the intergraphite cracks are investigated and used for the purpose of modeling and validation. SEM fractured sample is shown in **Figure 28.**

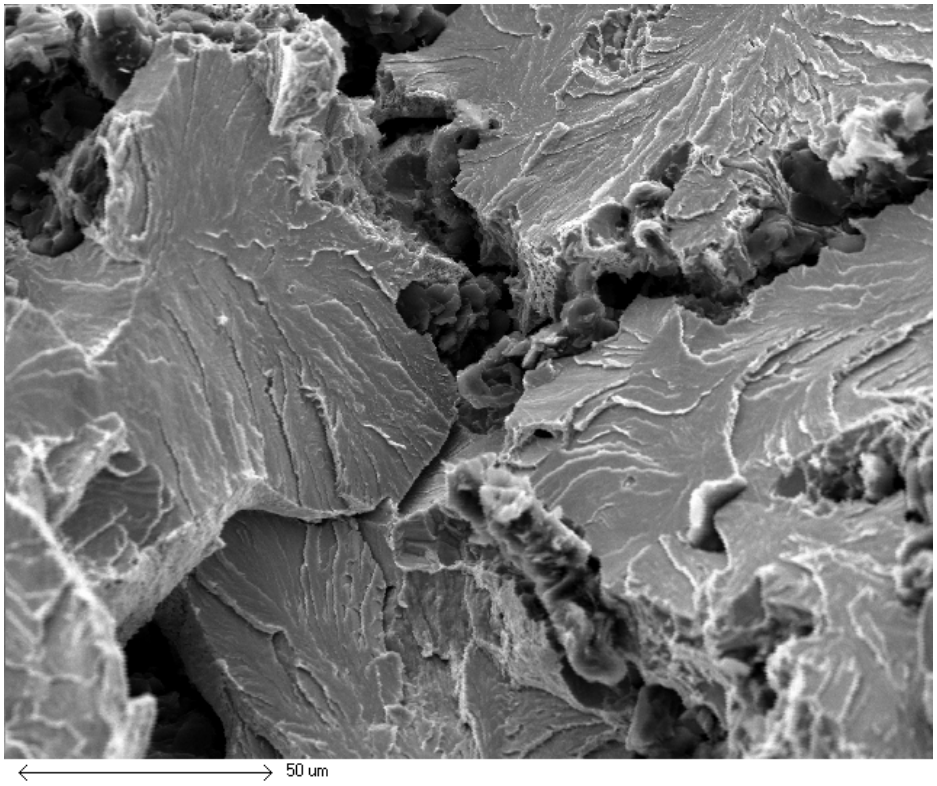

Figure 28 SEM image of CGI Charpy impact sample

6.2.2 Metallurgical Testing Procedures

The metal matrix composition of the CGI sample is >90% pearlite and <8% ferrite. The chemical composition of the CGI sample is listed in **Table 18**. The samples are very well polished and cleaned to remove any surface contamination. The chemical constituents are

extracted using the Glow Discharge Optical Spectroscopy (GDOES) analysis. GDOES combines sputtering and atomic emission to provide an extremely rapid and sensitive technique for element depth profiling. GDOES is often used to analyze surface films and coatings formed on a metallic material, since depth profiling by GDOES enables to analyze the quantitative composition of the material. This technique provides precise characterization of alloyed steels and other intermetalic compounds. Advantages of the GDOES technique are the simple sample preparation, short measuring time, relatively acceptable high sensitivity, and the very effective chemical analysis achieved.

Table 18 Chemical composition of compacted graphite iron sample using GDOES analysis

C%	S%	Si%	Ti%	Mg%	Mo%	Mn%	Cr%	Ni%
2.75	0.0113	2.242	0.022	0.0168	0.0053	0.354	0.0567	0.0094

The compacted graphite iron samples are cut and cold mounted in resin. The samples are then carefully sanded using different grades carbide sanding discs to prepare the sample test surface. To preserve the graphite contents, the last sanding stages are performed with wax instead of water. Then the samples are well polished using 0.005 and 0.002 mm diamond polishing discs to eliminate miniature scratches. This procedure is necessary to produce a clear image of compacted graphite particles in the metal matrix. However, distinction between pearlite and ferrite cannot be made at this point as shown in **Figure 29**.

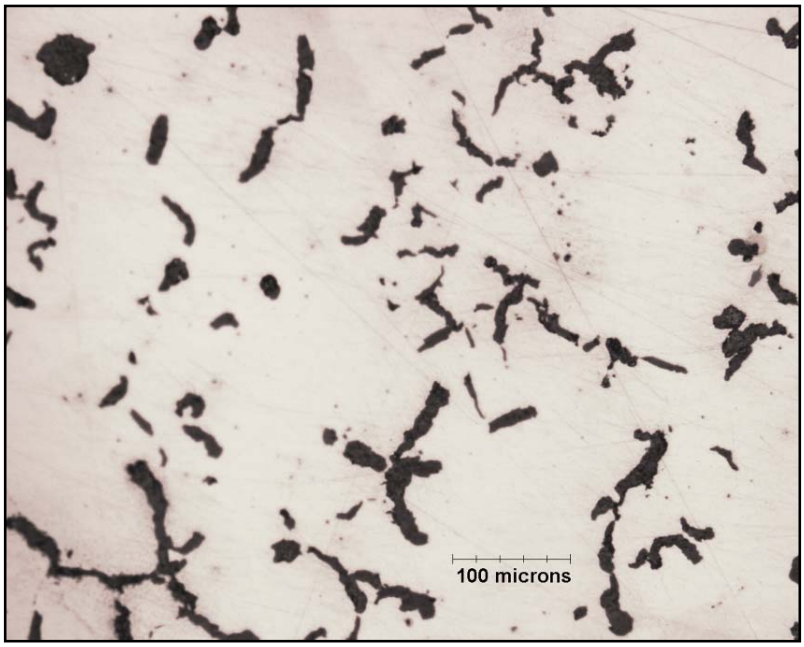

Figure 29 Compacted graphite iron sample showing the graphite particles

To distinguish the pearlite from the ferrite constituents, the samples are etched with 2% *Nital*. The sample is exposed to *Nital* for a short time (5-10 seconds) and then washed under a stream of water to stop further etching of the sample. The sample is then washed with alcohol (methanol or ethanol) and air dried. Examination of the etched samples exposes the pearlite and ferrite colonies as shown in **Figure 30**.

The ferrite constituent (pure iron) shows in the form of a white shiny area, while the pearlite is characterized by its distinctive two-phased lamellar structure. Pearlite consists of about 12% black contoured cementite formations (iron carbide) in about 88% ferrite. Graphite is the solid black regions shown below **Figure 30**. Graphite particles are commonly found surrounded by ferrite colonies, however, graphite may sometimes be surrounded by pearlite regions.

Figure 30 Etched CGI sample showing the pearlite and ferrite colonies. The white arrow points to the pearlite formation and the black arrow points to the ferrite.

6.3 Workpiece Preparation and Testing in Machining

6.3.1 Mechanical Testing Procedures

Preparation of the workpiece geometry is very important for accurate cutting forces measurement. As the cutting insert during force measurement is configured for face machining, the hollow cylindrical sample thickness must be peripherally constant. This will significantly minimize the overall cyclic waviness in the cutting forces profile due to wall thickness variation within the sample. The cylindrical samples are carefully turned to achieve a fixed wall thickness and a minimal eccentricity. Eccentricity measurement does not exceed 0.005 per 112 mm cylinder length. The samples are carefully turned to

5.500 ± 0.005 mm. peripheral thickness. Inside and outside turning of samples are carried out to achieve smooth internal and external surfaces. Sample preparation is carried out at a relatively low cutting speed (75 m/min) and low feed (0.05 mm/rev.). To prevent sample distortion by the lathe chuck due to their small wall thickness while preparation and measurement, a carefully turned thick steel plug is inserted inside the cylinder on the chuck side.

6.3.1.1 Experimental Procedure and Test Matrix

Dry turning tests are carried out on the prepared samples according to the shown test matrix in **Table 19**. The machining configuration is designed to insure an orthogonal cutting process. To insure orthogonality, the following conditions are strictly followed: (1) the insert edge is always perpendicular to the direction of cut, (2) the workpiece cut width is more than ten times greater than the feed rate (ratio 5.5:0.2), (3) the insert cutting edge (20 mm.) is wider than the width of the machined sample (5.500 ± 0.005 mm.). Since the tool is set to face machining, the feed rate is accordingly equal to the uncut chip thickness.

Each test is repeated six times for the reliability and repetitiveness of the collected data. The cutting insert is replaced with a new insert before every test to insure the sharpness of the cutting edge at the beginning of every force measurement. Each cut is performed for 5 seconds per insert to minimize the occurrence of worn or overheated inserts. The chosen test time is based on that no more than 2.5% increase in the cutting forces would be allowed due to tool wear under the severe cutting conditions shown in **Figure 31**. According to the preliminary tests, significant increase in the cutting forces is reached

after 15 seconds when machining at 100 m/min at feed rate 0.05 mm/rev. The low cutting speed is selected based on most literature data for comparison reasons while the higher cutting speed is according to the currently commercial value.

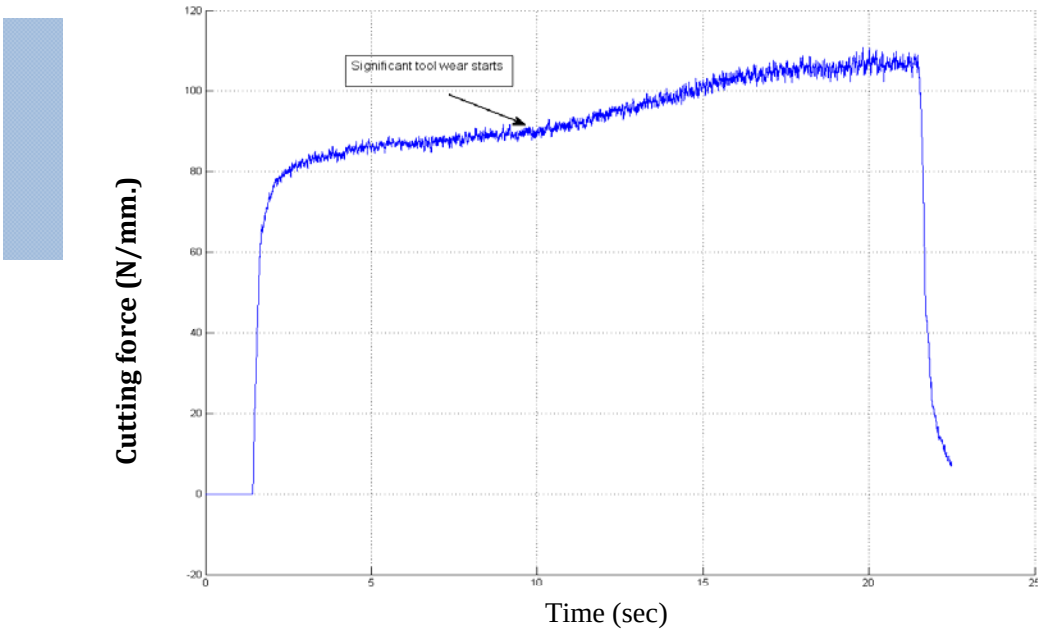

Figure 31 Significant tool wear initiation at lowest cutting force (100 m/min - 0.05 mm/rev) (uncertainty ± 1 N/mm.)

The cutting inserts used in all cutting tests are triangular uncoated carbide grade k68 from Kennametal on a KENDEX positive rake angle tool holder. The insert effective rake, clearance, and approach angles are 5^{o}, 6^{o}, and 0^{o}, respectively.

Table 19 CGI samples machining tests matrix

Test No.	Cutting Speed (m/min)	Feed rate (mm/rev.)
1	100	0.05
2		0.1
3		0.2
4	200	0.05
5		0.1
6		0.2
7	400	0.05
8		0.1
9		0.2

The cutting insert specifications are listed below in **Table 20**:

Table 20 The cutting insert mechanical and thermal properties (Kennametal Inc.)

Kennametal TPG432 – Grade 68	
Young's modulus (GPa)	534
Poisson ratio	0.22
Density (Kg/m^3)	14900
Specific Heat	250
Thermal Conductivity (W/mk)	85
Rake angle	5^o
Clearance angle	6^o
Approach angle	0^o
Chip breaker	None

The listed mechanical and physical properties listed in **Table 20** are received through direct communication with *Kennametal Inc*. The insert's mechanical and thermal specifications listed in **Table 20** will be used in the finite element modeling. The listed insert angles are the effective measurements when the above tool holder is used. Otherwise, the actual insert geometry may be obtained from *Kennametal Inc*.

Measurements of the cutting forces are conducted using a 3-component tool holder Kistler™ dynamometer (Type 9121) with piezoelectric sensors. Data acquisition is performed using Lab View 8.2 from *National Instruments*. Orthogonality of the machining configuration is verified by have a very low signal in the third axis. Machining arrangement of the test samples and the cutting tool are shown in **Figure32**. As shown in **Figure32**, the cutting tool is set to move parallel to the workpiece axis. All machining tests are carried out on a Nakamura-TOME SC-450 CNC machine.

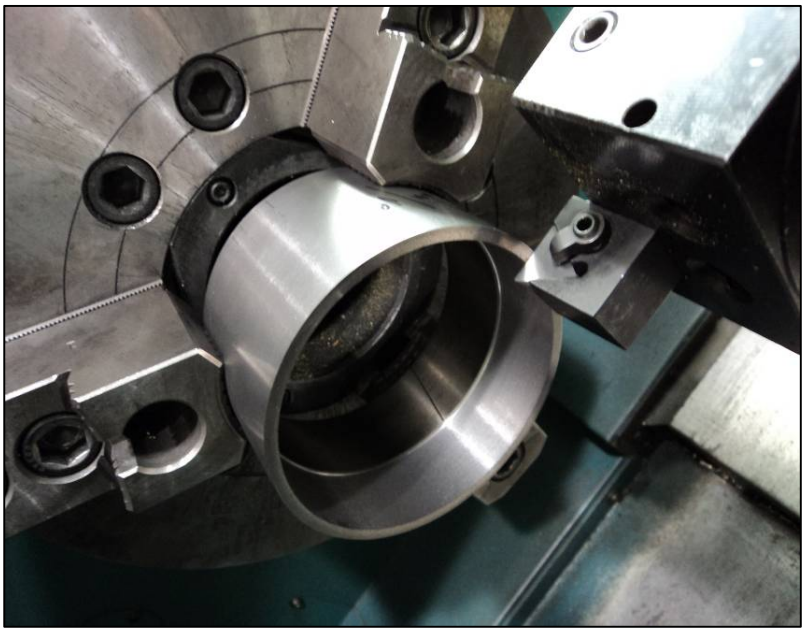

Figure32 Test configuration with the cutting tool mounted on the dynamometer

6.3.2 Metallurgical Testing Procedures

All the measurements of the tool wear are performed on a JEOL™ 7000F scanning electron microscope and a high magnification optical microscope. Chip samples are cold mounted and polished to reach the middle plane of the chip. The SEM image of the

mounted chip sample is shown in **Figure 33**. Measurements of the insert accumulated workpiece material on the tool flank surface are carried on using the scanning electron microscope JEOL 7000F. In assessing the insert wear extent no high magnification is needed. However, the SEM image quality is excellent and highly effective to investigate the wear profile.

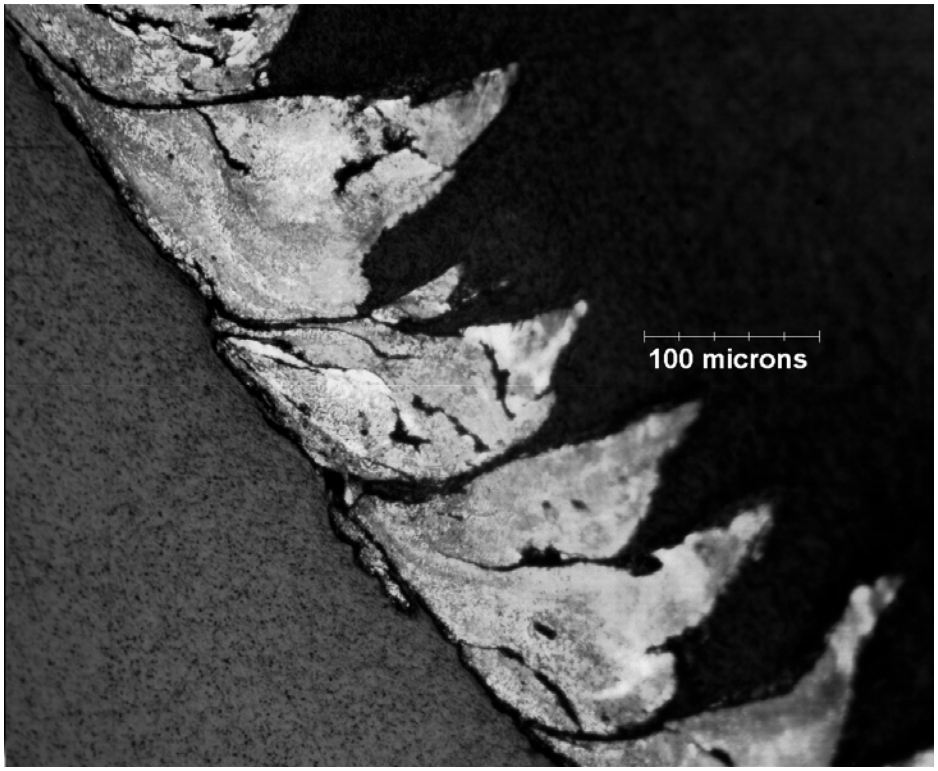

Figure 33 SEM middle plane chip image

Assessment of the insert wear is performed on every insert and the inserts' wear images matrix is provided in the Results and Discussion chapter.

CHAPTER 7

Results and Discussions

7.1 Introduction

The successful substitution of CGI to the currently used material in industry is contingent upon the two conditions; 1) CGI's exceptional mechanical and thermal characteristics and 2) CGI's comparable machinability to gray iron. Hence, since compacted graphite iron's characteristic performance is due to its unique microstructure, the effect of the CGI's microstructure on fracture and machining are the main themes of the current study. This chapter presents both fracture and machining experimental results and their relevant discussions, following the same sequence of activities pursued during the progress of work.

The first phase in this chapter will concentrate on the effect of compacted graphite iron's microstructure on crack initiation and propagation based on the relevant metallurgical investigations. More specifically, study of the role of graphite particles morphology in impeding crack initiation and propagation based on the curried out fracture tests will give more in depth understanding of CGI's characteristic performance.

Modeling compacted graphite iron's microstructure using the finite element method is proposed to simulate the fracture process. Validation of the finite element fracture model will be through a set of comprehensive metallurgical examinations of the fractured specimens relevant to the finite element model. Agreement between the experimental

work and the numerical simulation will verify the model.

The second phase in this chapter will concentrate on the effect of the microstructure of compacted graphite iron on machining. Such effect will be investigated, modeled, validated, and discussed. Three main tools of investigation will be employed in this work:

1) The cutting forces
2) The chip formation characteristics (chip morphology)
3) The cutting tool wear.

To validate the proposed finite element machining model, two validation tools are explicitly used: (1) the chip morphology and (2) the cutting forces.

The combined effects of cutting temperature and cutting forces on the cutting tool wear are analyzed to relate to the type of tool wear. The analysis will be through a comparative study of the experimental work and the finite element simulation results. This technique will be further elaborated on in its relevant section. During the validation procedures, other findings will be posted for their practical importance.

7.2 Phase 1: The effect of the microstructure of CGI on fracture

Maximum true strain recorded in the quasi-static (0.1mm/min) uniaxial tensile test of the tensile test samples is 1.56% as shown in **Figure 34** (a). Cast irons in general have limited plastic deformation represented in the low strain to fracture limit. However, tow factors will enhance the plastic deformation in compacted graphite iron. The first is due to the presence of the soft ferrite constituent (about 8%) which improved crack tip bluntness due to its ductile property. The second is due to the round end graphite particles which

decrease the stress concentration at the graphite ends. These two factors lead to an improved plastic deformation and extended strain to fracture limit.

From the curried out tensile tests, the average maximum tensile strength recorded is 520 MPa (75,400 psi). The yield strength is determined by the 0.2% offset tangent modulus method and is equal to 400 MPa (58,000 psi). The calculated tangent modulus of elasticity is equal to 158 GPa (23 Mpsi). To avoid the effect of the geometrical instability present in tensile test due to necking, shear test is implemented. The shear test sample is tested at controlled elongation rate (0.1 mm/min) where the maximum true strain achieved is 4%. The shear test results are graphed as shown in **Figure 34(b).**

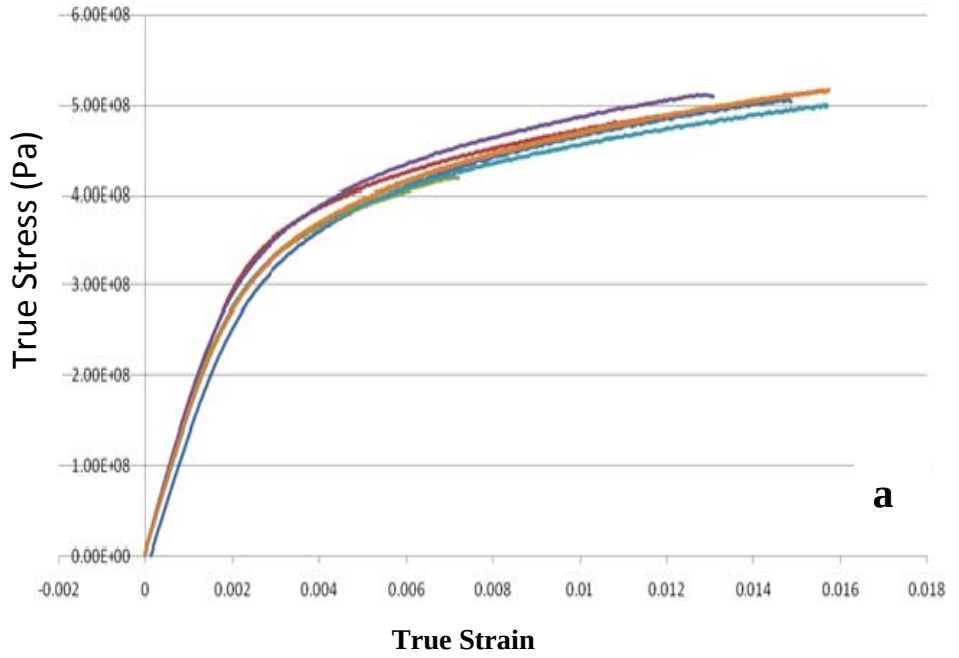

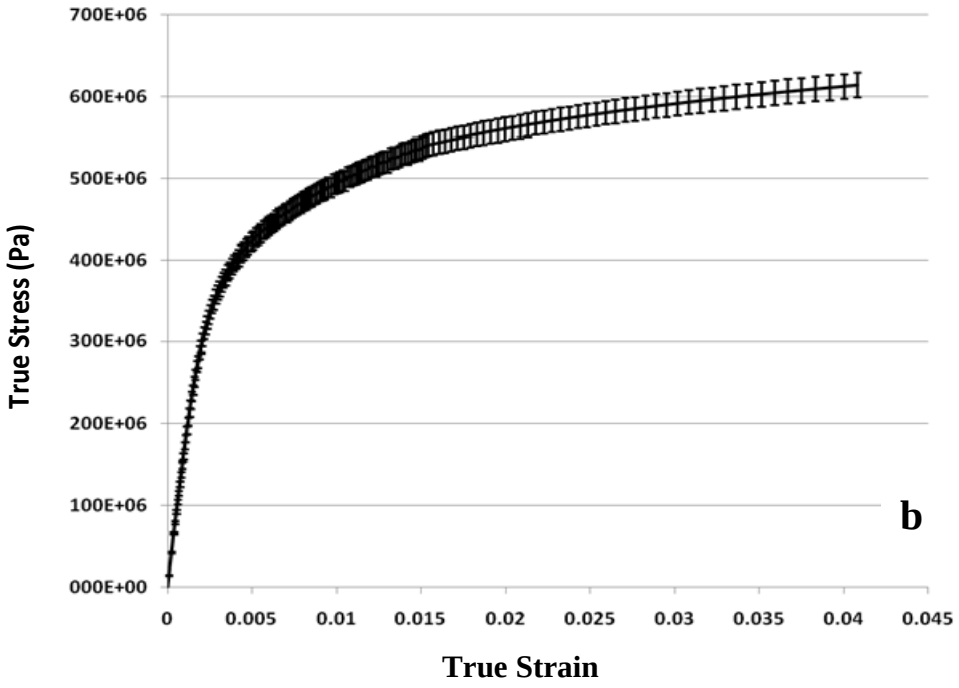

Figure 34 True stress-strain plots for CGI axial test (a), shear test (b)

7.2.1 Fracture Modes in Compacted Graphite Iron

The investigated CGI material consists of >90% pearlite and <8% ferrite. SEM analyses of the tensile samples' fractured surfaces at the central section (zone of nucleation) suggest the presence of two distinctive fracture modes; brittle and ductile modes.

Brittle fracture in the metal matrix is mainly induced by the percentage of the two-phase lamellar structure pearlite (>90%). The high strength pearlite constituent exhibits brittle fracture due to its content of the hard cementite (iron carbide). Brittle fracture is characterized by rapid crack propagation with less expenditure of energy due to minimal plastic deformation preceding fracture.

Examination of the fractured surface shown in **Figure 35** shows fracture under transgranular cleavage mode. Brittle transgranular cleavage mode is indicated by the presence of smooth cleavage facets and river patterns as known characteristics of such fracture mode indicated by the black arrow in **Figure 35**. Transgranular cleavage fracture frequently initiates on many parallel cleavage planes. As the fracture advances, the number of active planes decreases by a joining process that forms progressively higher cleavage steps indicated by the white arrows as shown in **Figure 35**. The edges of such steps form what is known as river patters. Such patterns are characteristic in identifying the origin of fracture and the direction of which fracture propagates. The river patters join in the direction of fracture progress.

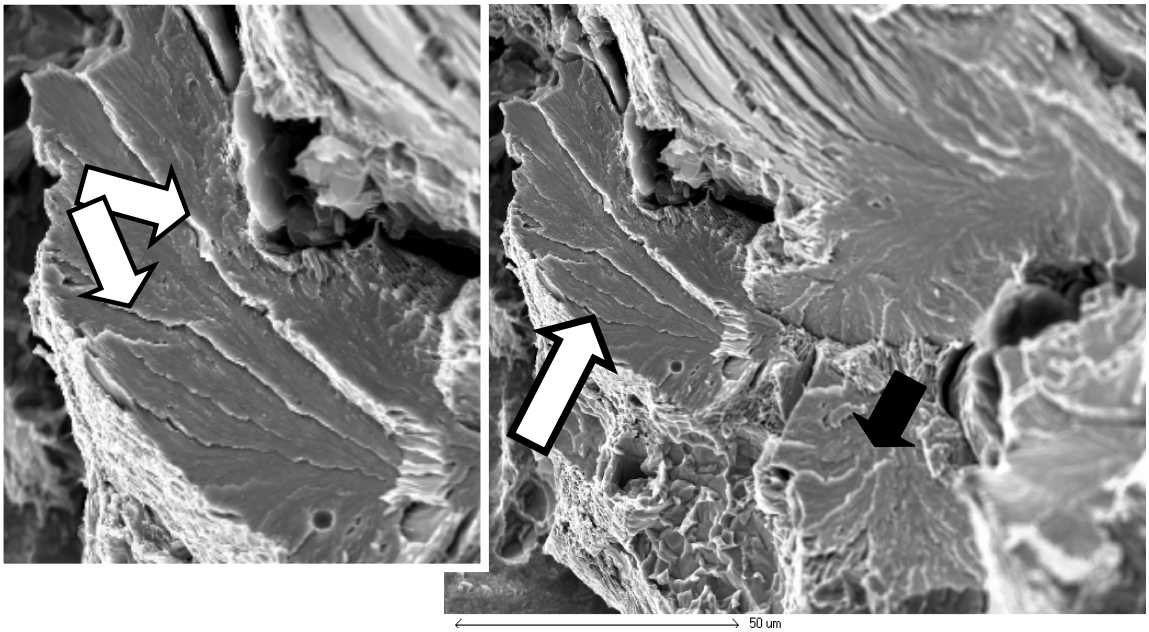

Figure 35 Cleavage planes merging in the direction of fracture propagation. As fracture propagates, the planes step get higher and fewer in number. The white arrow indicates the direction of fracture propagation

In addition to the brittle transgranular fracture in the metal matrix, presence of quasi-cleavage fracture characteristics are shown in **Figure 36**. Quasi-cleavage fracture exhibits specific characteristics of both cleavage and plastic deformation. The cleavage facets blend into areas of dimple ruptures and the cleavage steps becomes tear ridges as indicated by the arrows in **Figure 36**.

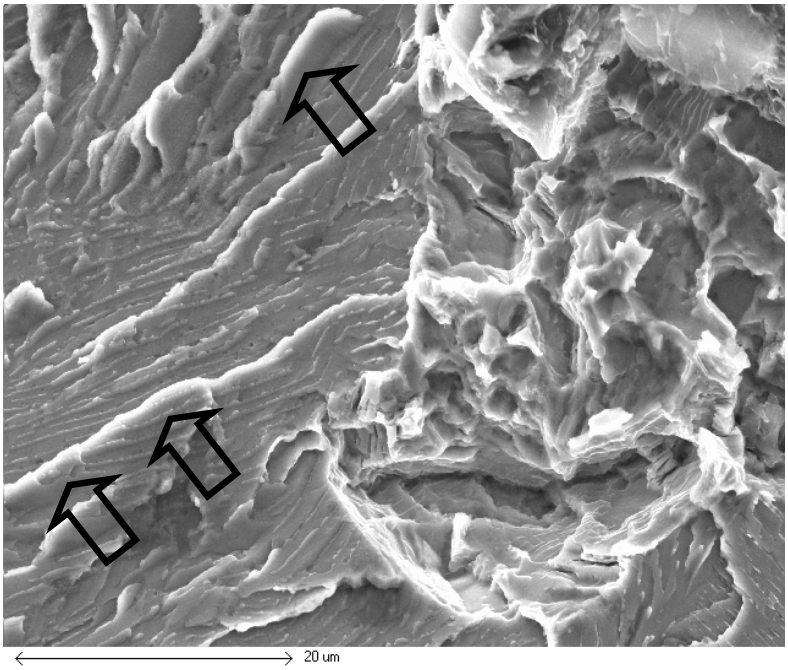

Figure 36 Quasi-cleavage characteristics

The ductile fracture is due to the percentage of ferrite in the metal matrix. Ferrite, pure iron, is usually found surrounding the graphite particles participating in a better crack tip bluntness and accordingly enhancing plastic elongation (higher fracture strain). Ferrite colonies are shown either surrounding the graphite particles or alone in **Figure 37 (a)**.

As shown in **Figure 37 (b)**, ruptured dimples are formed in the shape of numerous cuplike fine depressions which are the direct result of multiple microvoids coalescence and extended plastic deformation. Ductile fracture is characterized by the considerable plastic deformation contributing to less overall brittle behavior of compacted graphite iron and enhanced toughness.

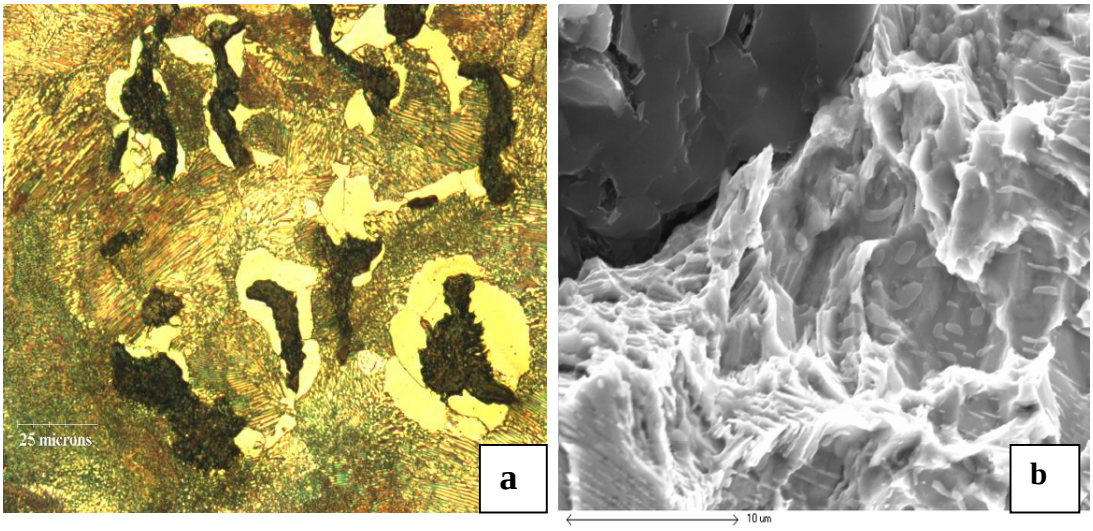

Figure 37 Ferrite colonies surrounding graphite particles (a). Ductile fracture showing the ruptured dimples in a ferrite region adjacent to a graphite particle. The graphite particles is at the top left corner (b)

7.2.2 Fracture Initiation and Propagation

Graphite particles are mainly the source of fracture initiation in compacted graphite iron. Preliminary optical microscope investigations of the fractured surfaces show that fracture initiates at the graphite particle since it is the weakest constituent. This fracture initiation scenario is supported by further SEM analyses as the number of cleavage steps and the river patterns merge in the fracture progress direction as shown in **Figure 38**. Examination of the cleavage steps and river patters indicate their occurrence at several localities at the same time rather than progressively. Discontinuous patterns of fracture indicate a trend of fracture initiation and termination with further loading in the form of crack initiation, propagation, followed by bluntness of fracture due to change of phase or the presence of grain boundaries. This unique morphology and structure of graphite significantly participate to the high strength and extended plastic deformation. Such

fracture progress will be simulated in the finite element fracture model.

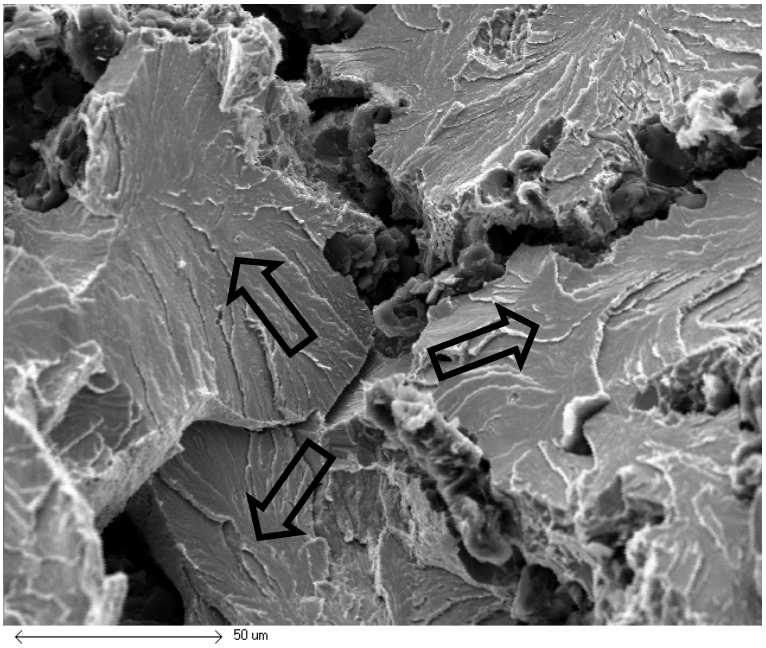

Figure 38 Fracture initiation at the graphite particle and propagating outward as the cleavage planes merge in the direction of fracture progress

SEM investigations show the presence of both compacted and nodular graphite particles in the studied samples. Nodular graphite particles are characterized by their distinctive growth of carbon mainly in the prismatic direction. This distinctive growth leads to a stronger particle where the carbon atoms are strongly bound by the high covalent forces, compared to the compacted graphite particles. Accordingly, two fracture scenarios exist based on the type of graphite. In contrast where nodular graphite is present, fracture has predominantly initiated in the form of interfacial decohesion between the graphite and the metal matrix **Figure 39** (a). The graphite-matrix decohesion is promoted by the less irregular particle boundaries leading to smaller adhesive interface. This characteristic fracture behavior will be shown in the FE simulation.

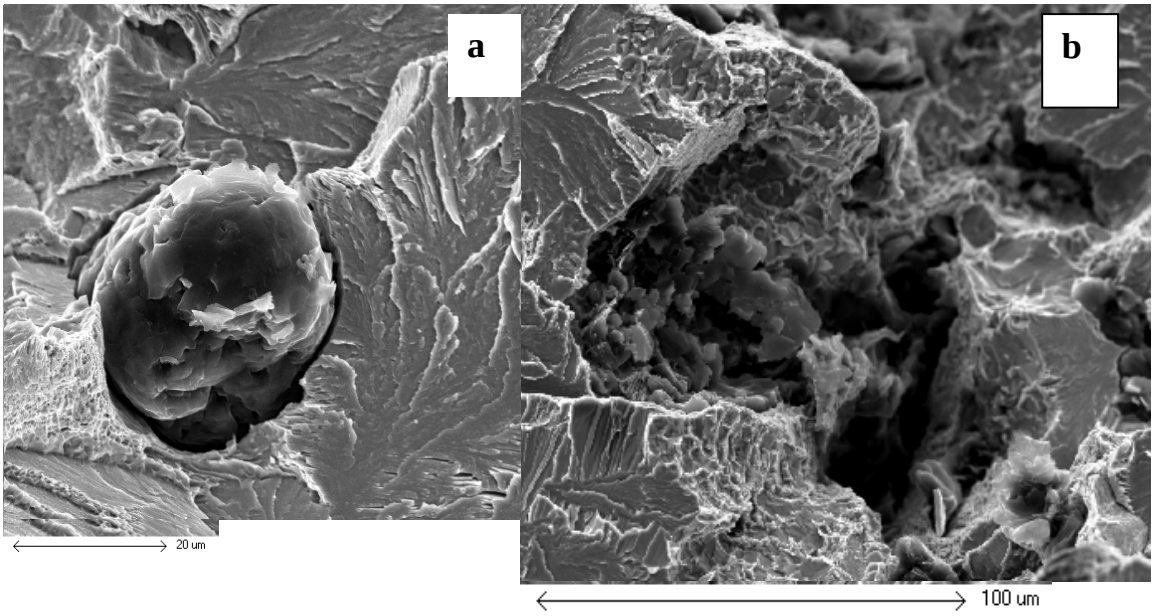

Figure 39 Decohesion between the nodular graphite particle and the metal matrix (a), Fracture within the compacted graphite particle where no decohesion between the graphite and the metal matrix (b)

As compacted graphite is characterized by its interchangeable growth of carbon in the basal and prismatic planes, compacted graphite is less self cohesive than nodular graphite. In addition, the irregular boundaries of compacted graphite improve the particle's cohesion to the surrounding matrix. Therefore, intergraphite fracture is more dominant in the compacted graphite particles as shown in **Figure 39(b)** and in **Figure 40**. Metallurgical investigations show that intergraphite fractures in the form of microcracks formation and coalescence is characteristic in compacted graphite particles, indicating graphite fracture by cleavage parallel to the basal planes, as shown in **Figure 41**.

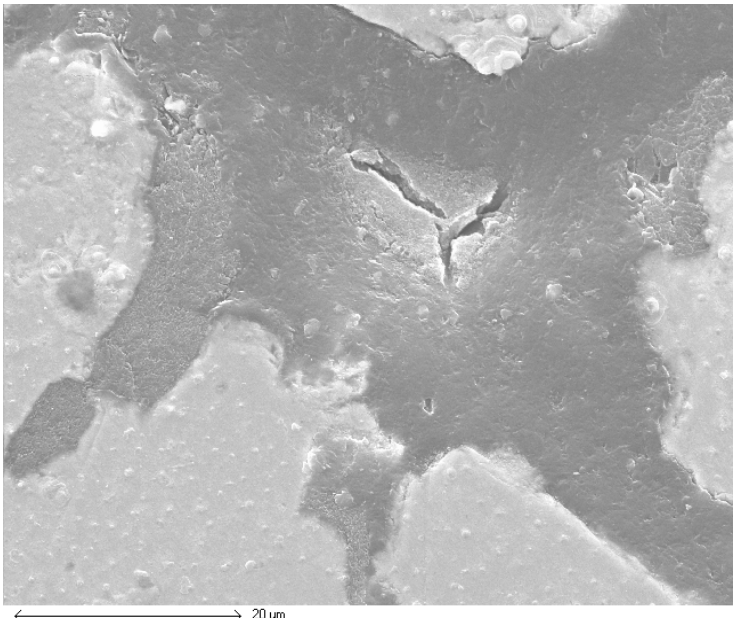

Figure 40 Intergraphite fracture in a compacted graphite particle

Separated fractured graphite planes are planes of grown graphite crystals mainly in the basal direction where the boding forces of the graphite layers in the perpendicular direction are several folds weaker (*van der Waals* forces) as shown in **Figure 41**.

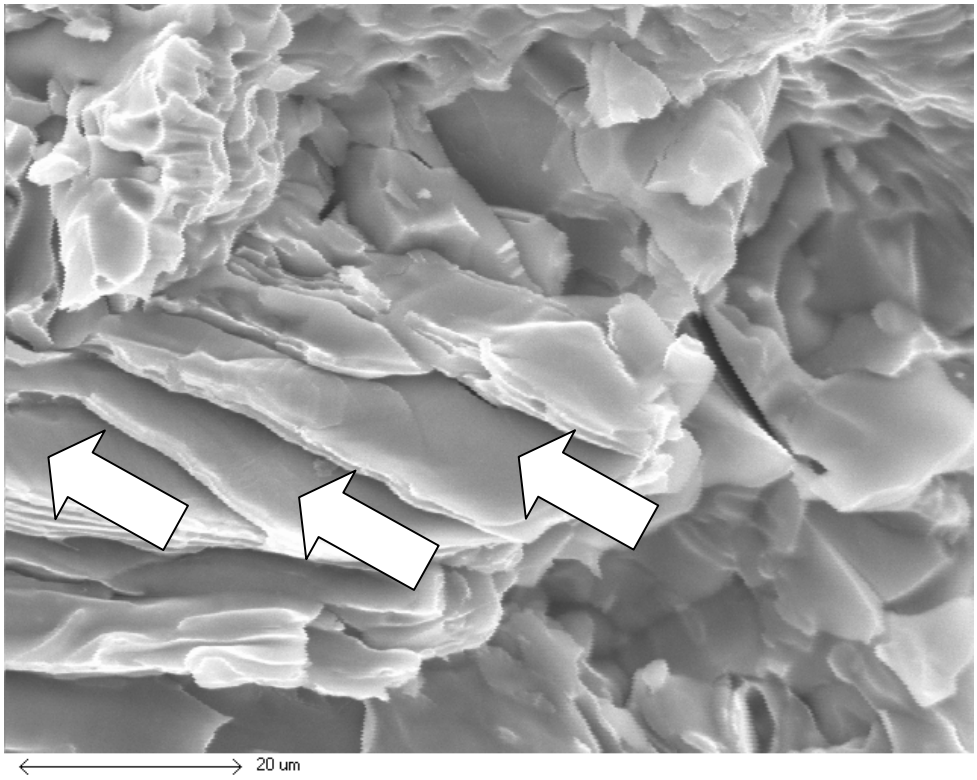

Figure 41 Fractured graphite particle characterized by planes separation due to weaker van der Waals bonding forces

Careful attention should be given in order not to mistaken the empty graphite pockets with the small ferrite dimples. Graphite pockets are characterized by their flat edges due to the low graphite fracture strain, unlike the elevated volcano-like walls of ferrite dimples due to the ductile deformation (necking) prior to failure. Partially empty graphite pockets would be characterized by the absence of matrix cleavage characteristics or vermicular formations on the pockets inner walls. Partially empty graphite pockets are not commonly present in the fractured surfaces. The above findings will be foundational to the validation of the fracture characteristics in the finite element model.

7.2.3 Validation of the Finite Element Fracture Model

Investigation of *von Mises* stress contours shows that higher *Mises* stress is present at the narrow ends of the vermicular graphite particles. Small matrix bridges at some regions promote the concentration of higher Mises stresses. The smaller the matrix bridges, the higher gradient and the more concentration of *Mises* stress contours.

As shown in **Figure 42 (b)**, crack initiation occurs at the region where the maximum displacement exceeds the prescribed displacement that is experimentally determined equal to the maximum crack width (0.002 mm.) and equivalent plastic strain at the graphite-matrix interface equals to 0.07. Graphite fracture initiation and decohesion occurs at low strain since graphite does not exhibit significant plastic deformation before fracture.

As shown in **Figure 42 (a)**, all graphite particles share the same equivalent plastic strain suggesting the vulnerability of simultaneous multiple crack initiation at all graphite particles. Higher equivalent plastic strain and higher stress concentration are recorded at thinner graphite cross-sections and narrower ends as in gray iron due to the stress concentration effect where the white arrows point **Figure 42(a&b).** As shown in **Figure 42(b),** crack initiation and propagation occurs at the locations where the high PEEQ values are.

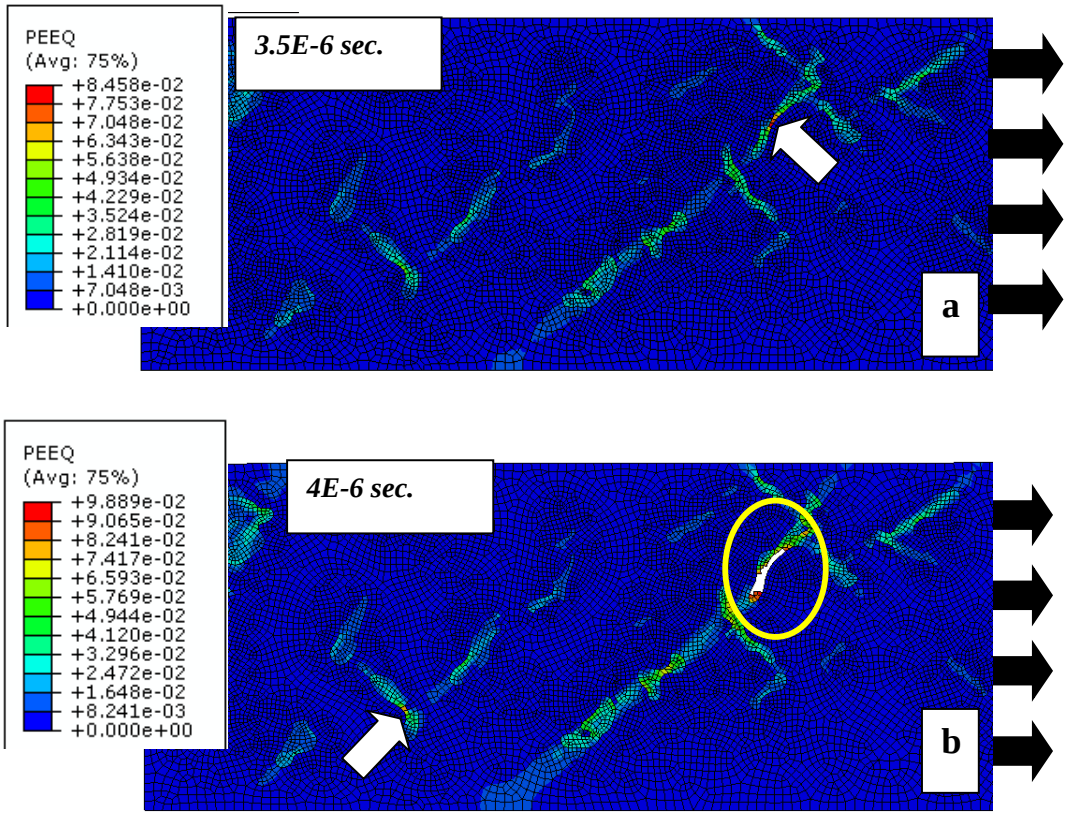

Figure 42 Crack initiation higher PEEQ values (white arrows) within narrow ends in the graphite particles (a). Crack initiation in the finite element model (b).

Further straining of the tensile test sample results in multiple crack initiation at either the graphite and/or graphite-matrix interface where the fracture criterion is satisfied as shown in **Figure 43 (a)** and **Figure 42(b).** The concurrent origination of high equivalent plastic strain at multiple graphite particles and at the graphite-matrix interface in the finite element model justify that crack initiation is not progressive. In other words, crack propagation does not proceed progressively from one cell to the next, but is a result of a simultaneous crack initiation at several cells which will eventually coalesce at higher strains **Figure 43 (b)**. This fracture scenario is found in the real fracture samples.

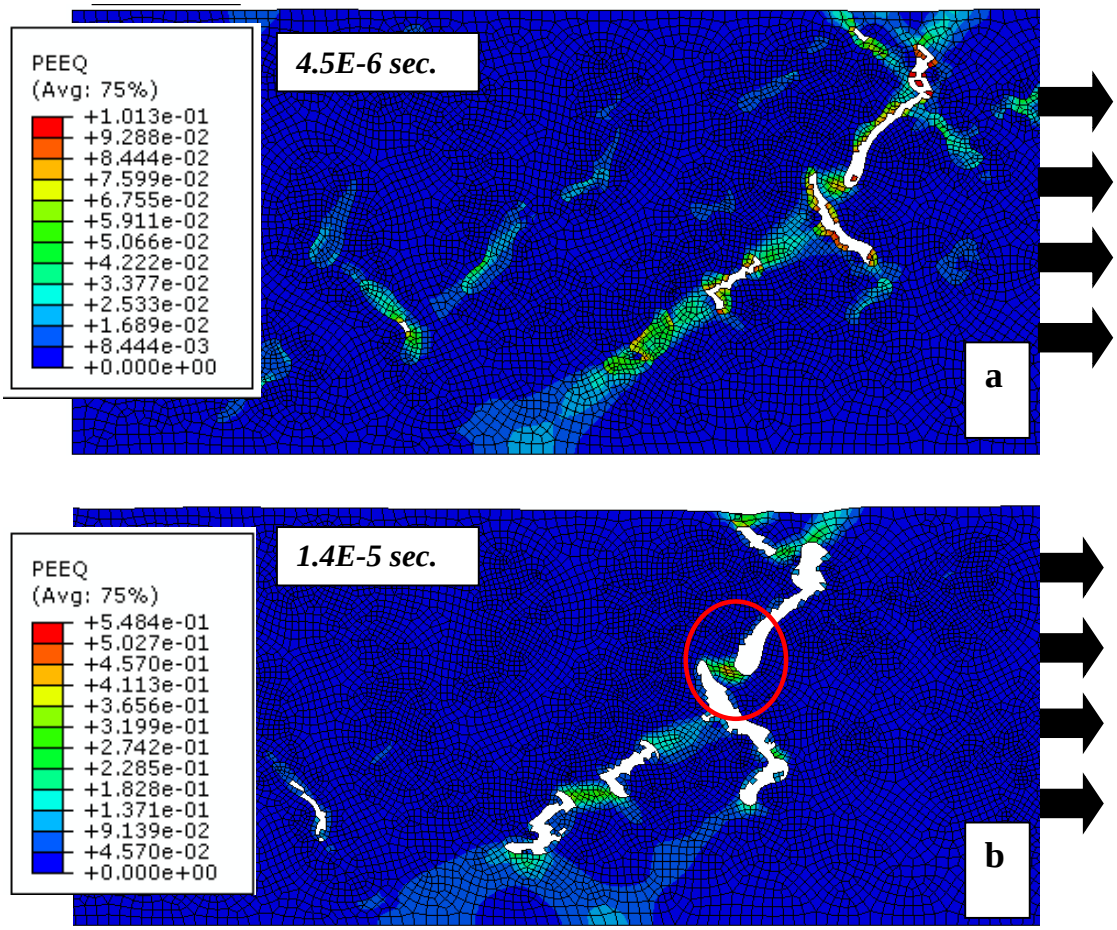

Figure 43 Crack initiation and propagation as simultaneously occurring at different localities in the simulated CGI sample (a), Crack bluntness at a round graphite end and diversion of crack path (b)

The round graphite ends of the compacted graphite particles work as crack initiation impedance leading to higher overall strength. In addition, this advantageous role of the round graphite particles ends facilitates crack bluntness, participating into higher fracture strain and further elevated overall strength as shown in **Figure 44**. As crack bluntness participates into extending the overall fracture strain level, crack paths alteration occurs participating to a higher strength prior to fracture.

Crack path alteration can be seen in **Figure 44**.

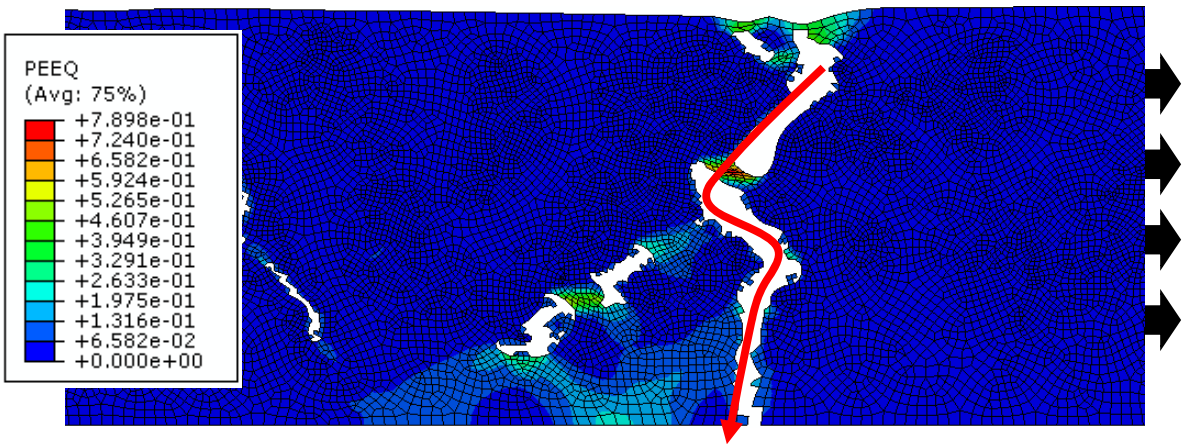

Figure 44 crack coalescence forming the final crack path leading to complete fracture of the FE sample.

Seeking simplicity, the mechanical and thermal graphite properties for both nodular and compacted graphite particles used in the current FE model are modeled equal. However, a more graphite-matrix decohesion fracture results in nodular graphite particles (indicated by the black arrows) is shown in **Figure 45**. On the other hand, more intergraphite fracture is found to be dominant in the vermicular graphite particles (indicated by the white arrows) is shown in **Figure 45**. Clearly this characteristic behavior in the finite element model is more of a morphological than of a material related nature. Future input of graphite type dependent properties in the FE model will significantly expose this fracture behavior. This explains the advantageous feature of the irregular graphite boundaries in compacted graphite particles and its less vulnerability to decohesion.

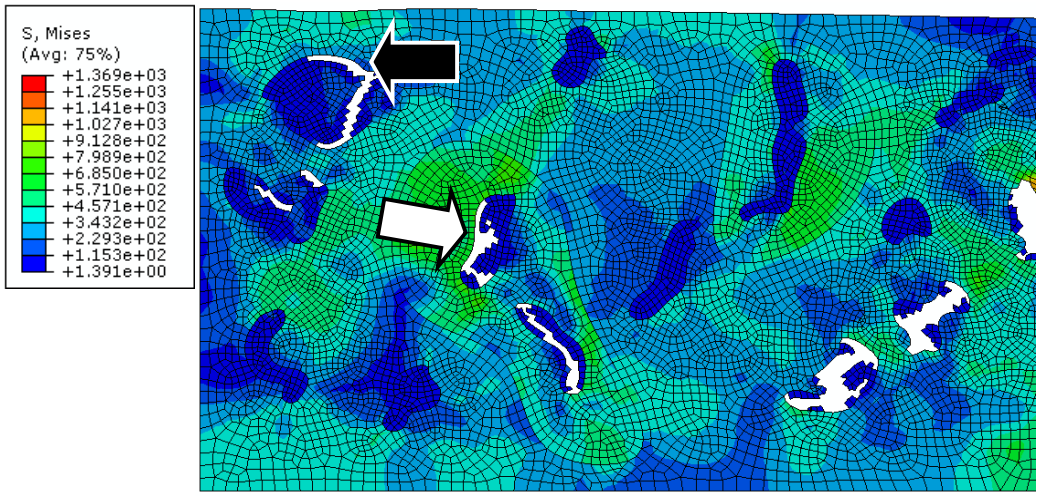

Figure 45 Nodular graphite exhibiting decohesion from the metal matrix

SEM samples images exhibit the same FE model crack bluntness, shown in **Figure 46**. Crack bluntness at the round graphite ends will reroute the existing crack path leading to the need of further straining to initiate another crack which will not propagate until the local effective strain reaches the critical limit enhancing the overall material strength.

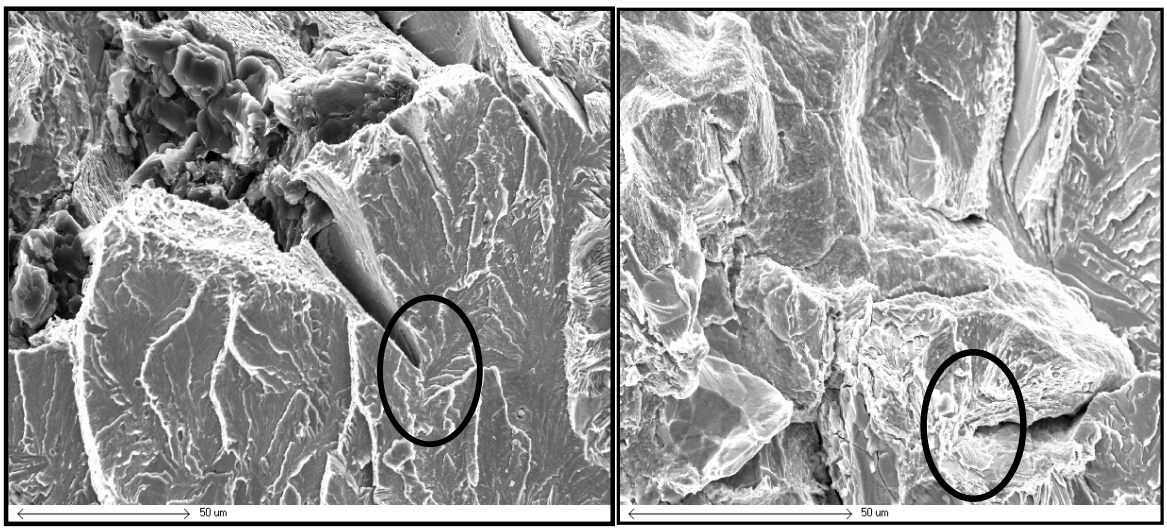

Figure 46 crack path alteration due to crack tip bluntness in a fractured CGI sample

The finite element simulated stress-strain graph exhibits higher fracture strength. The simulated FE model exhibits a tensile strength of 640 MPa while the experimental fracture strength recorded is 530 MPa. The simulated tensile strength is about 1.2 of the experimental tensile strength. Miniature machining imperfections in the real test sample will promote fracture initiation. In addition, the simulated and experimental strengths difference can be referred to the strain rate difference. The experimental strength is recorded at strain rate of 0.1 m/min., while the simulated model is performed at strain rate equal to100 m/min. This can be justified by *Johnson-Cook* model's second term which accounts for the effect of strain rate as:

$$1 + C\ ln\left(\frac{\dot{\varepsilon}_p}{\dot{\varepsilon}_0}\right) = 1 + 0.0235\ l\,n\left(\frac{100}{0.1}\right) = 1.162$$

The simulated modulus of elasticity is 160 GPa while the experimentally determined is 158 GPa. Maximum simulated fracture strain is 0.032, while the experimentally recorded is 0.016. The strain-to-fracture difference is referred to the geometrical instability in the real test sample. On the other hand, the maximum experimentally recorded shear strain is 0.04 which is reasonably close to the simulated strain-to-fracture value.

The tensile strength in the simulated stress-strain graph is recorded before the first crack initiation. Once the first crack occurs, the first drop in stress-strain graph occurs. Initiation and propagation of cracks within the sample will decrease the load bearing capacity of the simulated sample leading to variation in the stress-strain values as shown **Figure 47**.

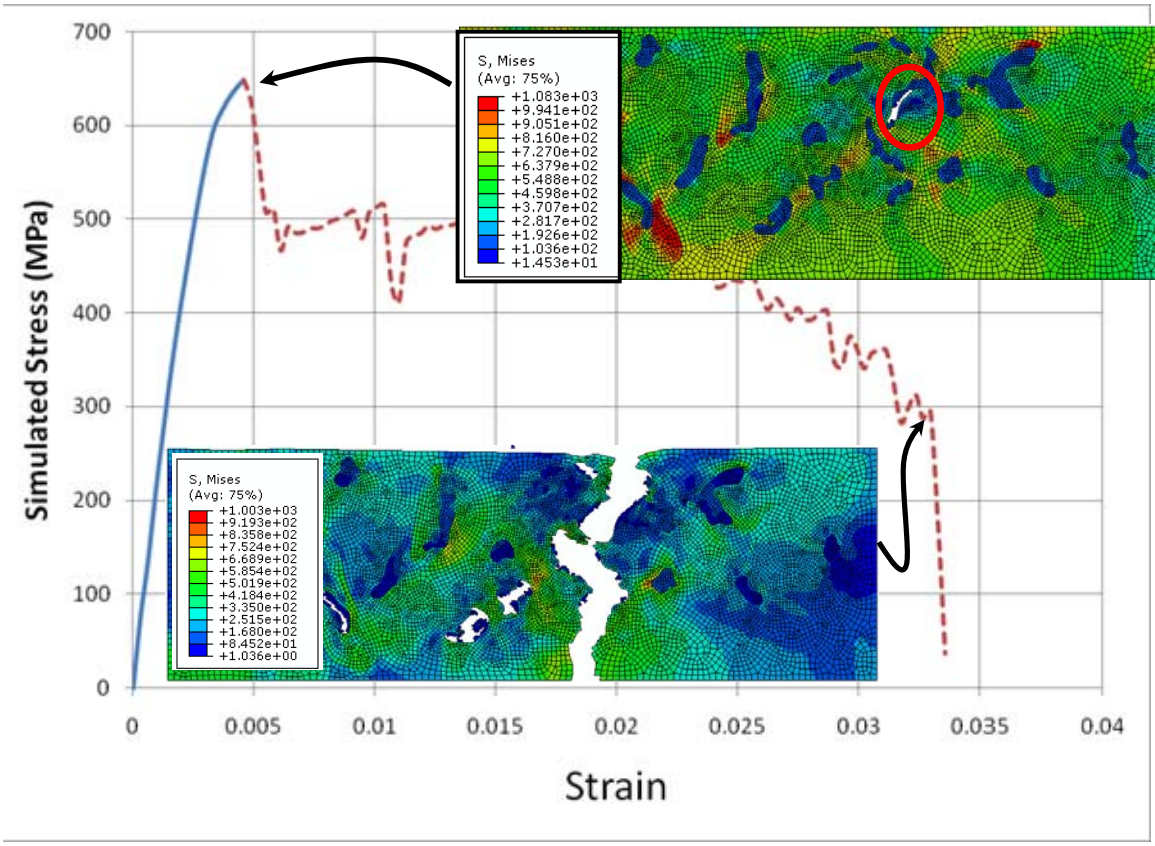

Figure 47 FE simulated stress-strain graph due Crack initiation and final fracture.

7.3 Phase 2: The effect of the microstructure of CGI on machining tests

The machined samples are prepared in the form of hollow cylinders of wall thickness 0.55±0.1 mm. The outer diameter of the sample cylinder is 116±1mm. and each cylinder is 160 mm. long. Each cylinder is carefully turned to achieve minimal eccentricity along the workpiece axis. Eccentricity error in each sample is within 0.005 mm.

Machining tests of the CGI samples are performed according to the following parametric matrix in **Table 21**:

Table 21 CGI machining tests parametric matrix

Test No.	Cutting Speed (m/min)	Feed rate (mm/rev.)
1	100	0.05
2		0.1
3		0.2
4	200	0.05
5		0.1
6		0.2
7	400	0.05
8		0.1
9		0.2

7.3.1 The Cutting Forces (Results and Discussion)

Cutting forces measurements are performed at all cutting speeds (100, 200, and 400 m/min.) and feeds (0.05, 0.1, 0.2 mm/rev.) using a 3-component tool holder Kistler™ dynamometer (Type 9121). To eliminate inconsistency due to variation in samples wall thicknesses, the cutting forces are normalized by dividing them by each tested cylinder wall thickness. Accordingly, the cutting forces are expressed in N/mm. Follows are experimental forces graphs shown in Figure 49 and Figure 50.

The simulated cutting and feed forces are extracted as the horizontal and vertical components of the reaction forces applied on the back of the simulated cutting insert. The cutting and feed forces are summed separately over the time of the simulation. A sample of the calculated cutting and feed forces is shown in **Figure 48** for illustration. As shown in **Figure 48**, initiation and separation of chip segments throughout the simulation produce the oscillation of in cutting and feed forces.

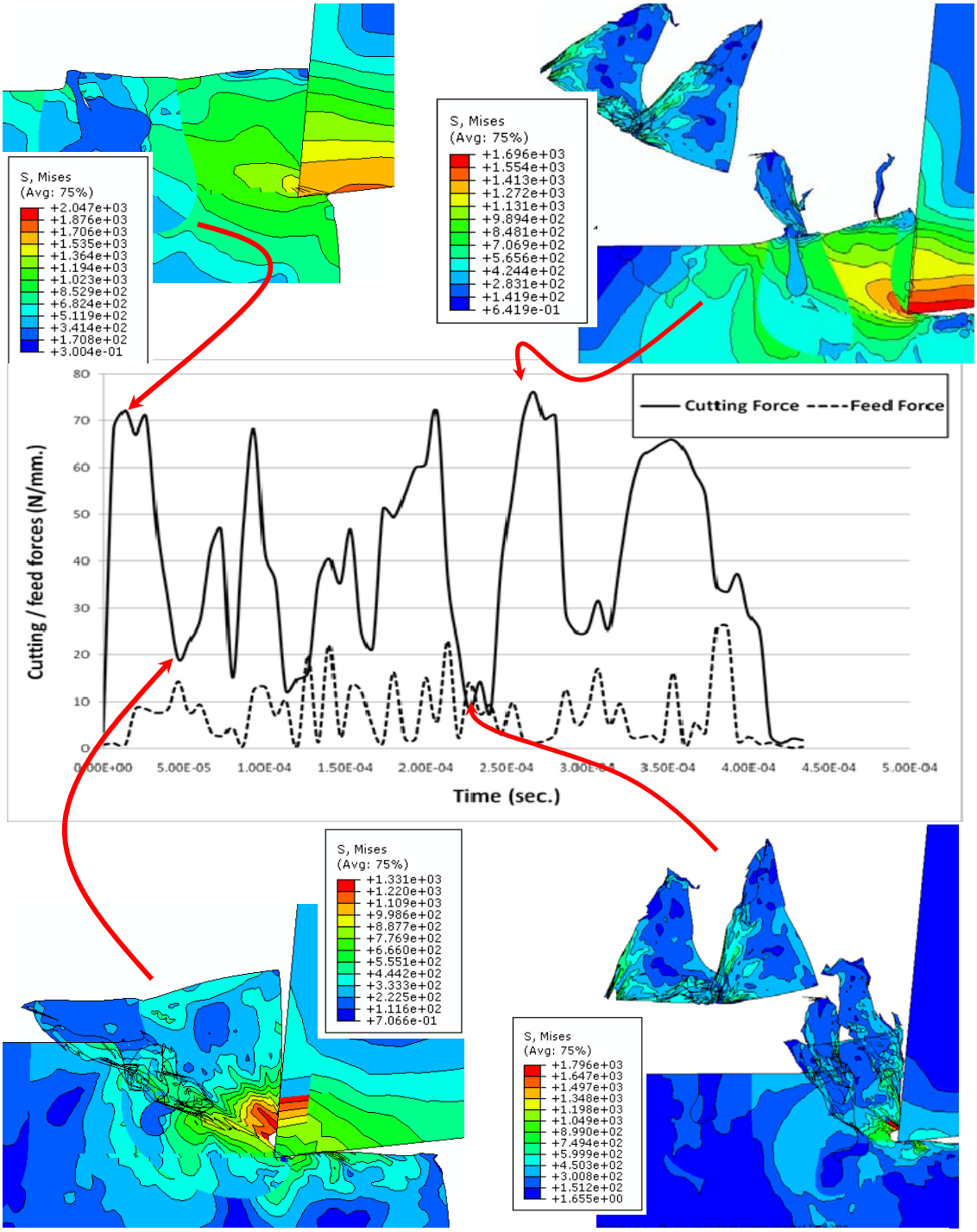

Figure 48 Simulated cutting/feed forces (0.05 mm/rev. – 100 m/min) and cutting tool position

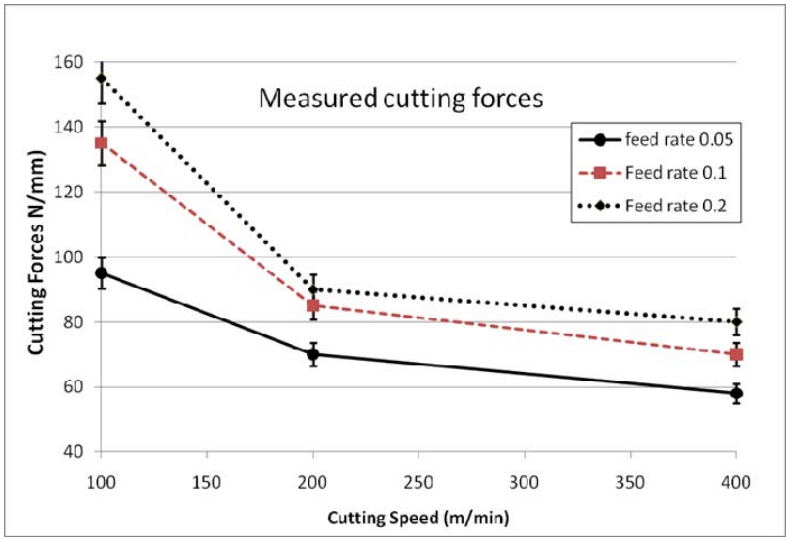

Figure 49 Measured cutting forces vs. cutting speeds

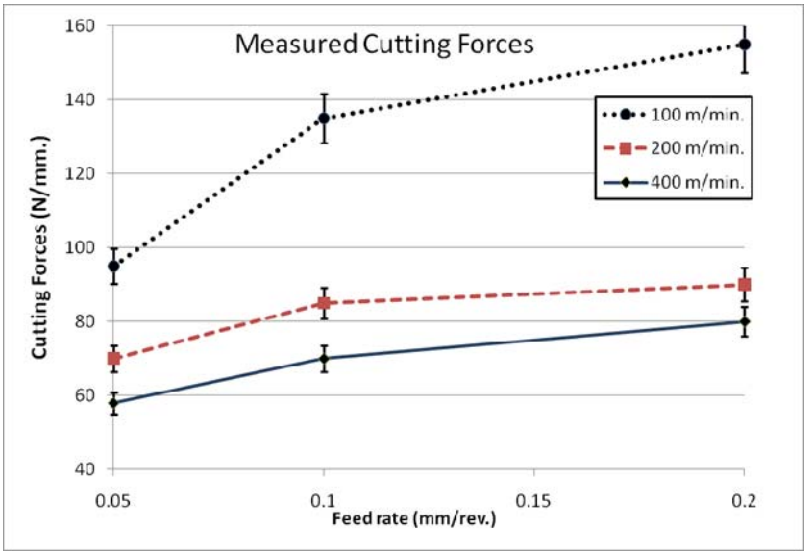

Figure 50 Measured cutting forces vs. the feed rate

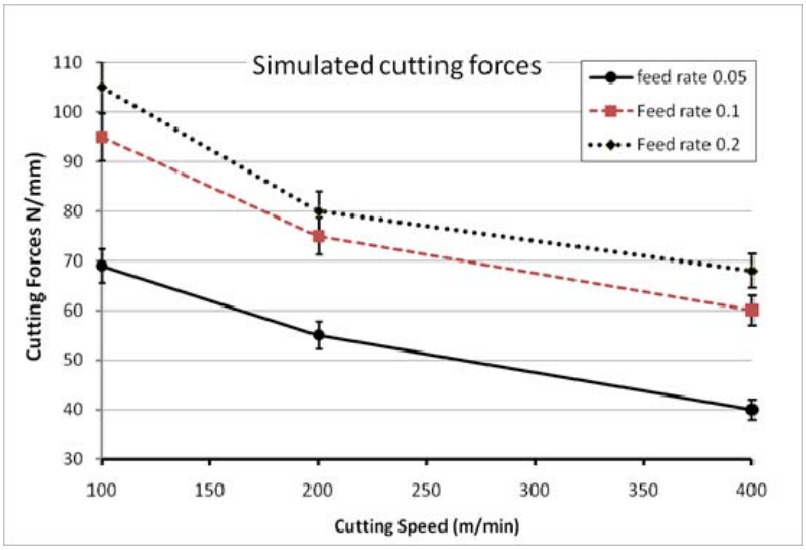

Figure 51 Simulated cutting forces vs. cutting speed

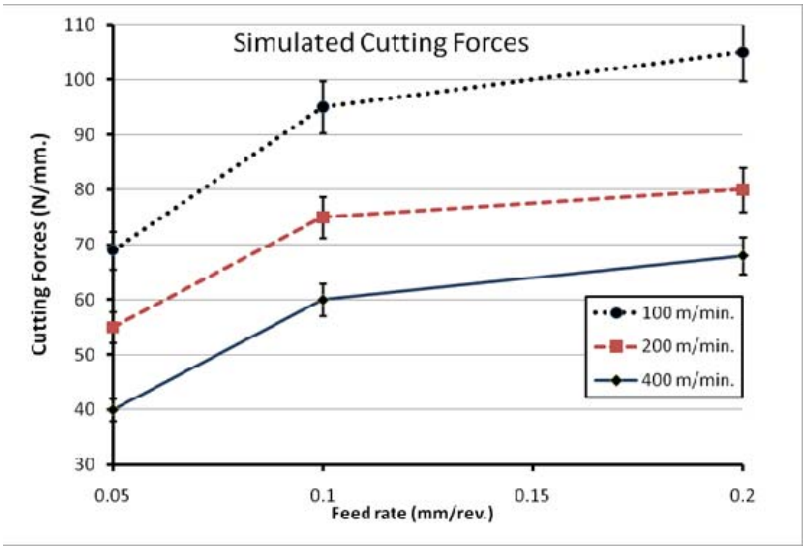

Figure 52 Simulated cutting forces vs. the feed rate

The measured cutting forces are plotted versus the cutting speed and the feed rate as shown in **Figure 49** and **Figure 50**. The general trend of the cutting forces versus the cutting speed in **Figure 49** demonstrates an increase in the measured cutting forces as the cutting speed is decreased. This is attributed in part to the decrease in the workpiece material thermal softening. As the cutting speed exhibits a significant effect on the cutting temperature in CGI machining, increasing the cutting speed increases the cutting temperature leading to a higher flow strain.

Two significant findings can be noticed in the cutting forces vs. cutting speed graph in **Figure 49:**

(1) For all feed rates, the drop in the cutting forces in the cutting speed range 100 to 200 m/min is steeper than it in the 200 to 400 m/min. range.

(2) Within the above cutting speed ranges, steepness in the cutting forces is more significant in the feed rate range 0.1 and 0.2 mm/rev. than at feed rate 0.05 mm/rev.

To reason the first finding, investigation of the cutting insert show presence of tool tip chipping in the 100 to 200 m/min cutting speed range in all the feed rates. Tool tip chipping has significantly attributed into the increase in the cutting forces in the aforementioned speed range. The increase in the cutting forces instigates more tool tip chipping which further increases the cutting forces as shown in **Figure 66**.

Increasing the cutting speed from 200 to 400 m/min increases the cutting temperature (thermal softening) lowering the material flow stress. The lowered flow stress due to

thermal softening eventually minimizes the tool tip chipping to complete disappearance. Therefore, the decrease in the cutting forces in the 200 and 400 m/min cutting speed range is due to the increase in material thermal softening and gradual decrease in the tool tip chipping together. To conclude, in the cutting speed range 100 to 200 m/min, change in the cutting forces is mainly controlled by the thermal softening and the tool tip chipping, however, in the 200 to 400 m/min. range, thermal softening alone is the cause of the less steep cutting force gradient.

Secondly, as for the significant steep slope in cutting forces in the feed rate range; 0.1 and 0.2 mm/rev. compared to 0.05 mm/rev shown in Figure 49, investigation shows that more significant tool tip chipping is present at feed rates 0.1 and 0.2 mm/rev. between 100 and 200 m/min cutting speeds. It is also found that increasing the cutting speed from 200 to 400 m/min has led to minimizing the tool tip chipping at feed rates 0.1 and 0.2 mm/rev. more significantly than at 0.05 mm/rev. This can be attributed to the effect of the feed rate to the cutting temperature. More specifically, in the feed range 0.1 to 0.2 mm/rev more thermal softening is produced due to the combined effects of feed rate and cutting speed leading to complete disappearance of tool tip chipping at 200 m/min. However, a trace of tool tip chipping is found at feed rate 0.05 mm/rev. at 200 m/min. which explains the less steepness of cutting forces at 0.05 mm/rev.

Study of the cutting forces versus feed rates in **Figure 50** shows steeper increase in the cutting forces in the range of 0.05 to 0.1 mm/rev. compared to 0.1 to 0.2 mm/rev. specifically at cutting speed 100 m/min. This can be attributed to the tool tip chipping dominant effect in this cutting speed and feed rate range. Again, the effect of the feed rate

on the cutting temperature leads to a less steep cutting force increase gradient in the feed rate range 0.1 to 0.2 mm/rev. as shown in **Figure 50** and as discussed above**.**

The simulated cutting forces are plotted versus the cutting speed and the feed rate as shown Figure 51 in and Figure 52. As can be seen in both experimental and simulated figures, the cutting forces follow the same trend with respect to the cutting speed. Similarly, increasing the feed rate increases the cutting forces in both cases. However, no effect of the tool tip chipping in the simulated cutting forces graphs is present due to its absence in the FE model. More specifically, the cutting forces gradient in the 100 to 200 m/min range is steeper in **Figure 49** than in **Figure 51**. The reason for that is the simulated cutting forces gradient in **Figure 51** is only due to the workpiece material thermal softening as a result of increasing the cutting speed as tool tip chipping is not simulated. Despite the absence of the tool tip chipping simulation**,** the effect of thermal softening has been captured in Figure 51 and Figure 52.

The current finite element simulation results are based on a perfectly sharp modeled insert. Despite that during all cutting tests significant care has been practiced to minimize any tool wear, breakage of the sharp tool tip during the first few milliseconds of machining is practically inevitable. Therefore, the simulated cutting forces will always be lower than the measured forces due to tool tip wear which will participate into more workpiece material-tool surface contact leading to higher cutting forces. Variation within 10-15% of the simulated main cutting force in comparison to the measured force would be acceptable based on the majority of relevant literature.

Simulated thrust forces are included in the current work as shown in **Figure 48**.

Simulated thrust forces are always contingent upon the simulated cutting insert geometry. Simulated sharp tip insert causes the thrust forces to record a very low value which is common in the major bulk of similar works.

7.3.2 The Chip Formation characteristics (Results and Discussion)

Preliminary investigations show that CGI machined chips are segmental, curly, and easy to break by hand in all machining tests. Cutting speeds and feed rates show some effect on the chip characteristics. Despite the characteristics variations in length, thickness, and frequency of chip segments, they all show segmentation due to fracture. Optical microscope images of different machined segmental chips are shown in **Figure 53**.

Keeping the cutting speed fixed, at feed rate 0.05 mm/rev. the chip is more of discontinuous segments where fewer chip segments are connected to each other. Based on SEM images, at feed rate 0.05 mm/rev. the chip size is closest to the size of the graphite particles (0.03 – 0.05 mm.) and complete fracture across the chip thickness is likely to occur leading to more separated chip segments.

Figure 53 CGI segmental chip at different feed rate and cutting speeds 0.05 mm/rev @ 200 m/min (a), 0.1 mm/rev. @ 200 m/min (b), 0.2 mm/rev. @ 200 m/min (c), 0.1 mm/rev @ 400 m/min (d).

As the feed rate is increased to 0.1 mm/rev., few more chip segments per chip are produced. Increasing the feed rate to 0.1 mm/rev. increases the matrix bridges in the chip relative to the average graphite particle size and fewer cracks are able to extend across the chip thickness. In addition, a slight increase in the cutting temperature due to feed rate

increase promotes longer chips. At 0.2 mm/rev. feed rate, the number of segments per chip does not significantly increase, however, depending on the cutting speed.

Keeping the feed rate fixed, increasing the cutting speed increases the cutting temperature. This promotes the material thermal softening in the chip and results in a relatively higher matrix strain-to-fracture producing more connected chip segments per chip. However, the presence of graphite particles at the top of the chip promotes surface crack where chip segmentation initiates and consequently easier formation of new chip segments. These two opposite factors will compete with each other leading to the final chip formation.

Examination of the chip segments reveals severe matrix strain at the secondary shear zone (pointed at with white arrows in **Figure 54**) as the pearlite contours are stretched following the direction of chip flow over the tool rake surface. This significant matrix strain is in part due to the high temperature at the secondary shear zone leading to increased matrix flow strain. Increased temperature at the secondary shear zone retards fracture at this region.

Presence of incomplete cracks extending from the free surface of the chip toward the tool tip suggests that crack initiates at the free surface of the chip and propagates toward the tool tip. The high temperature associated with high compressive stress closer to the tool tip re-welds the microcracks forming at the secondary shear zone side as shown in **Figure 54** represented by the white ellipses.

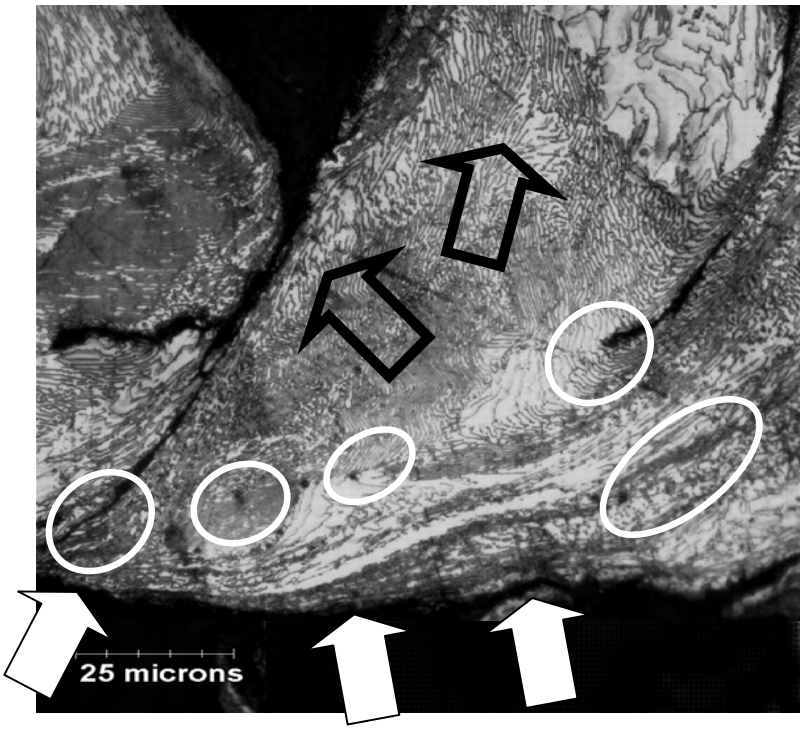

Figure 54 Chip segment severe matrix strain at the secondary shear zone side (white arrows), re-welding of microcracks due to higher compressive stress at the SSZ

Presence of the low plastic strain of the pearlite contours away from the secondary shear zone (pointed at with hollow black-boundary arrows) at the free surface side of the chip segment suggests that formation of the segments are initiated at lower fracture strain. To conclude, formation of chip segments starts at the free surface side of the chip where the strain-to-fracture is lower rather than at the chip-tool side where the strain-to-fracture is relatively higher [195].

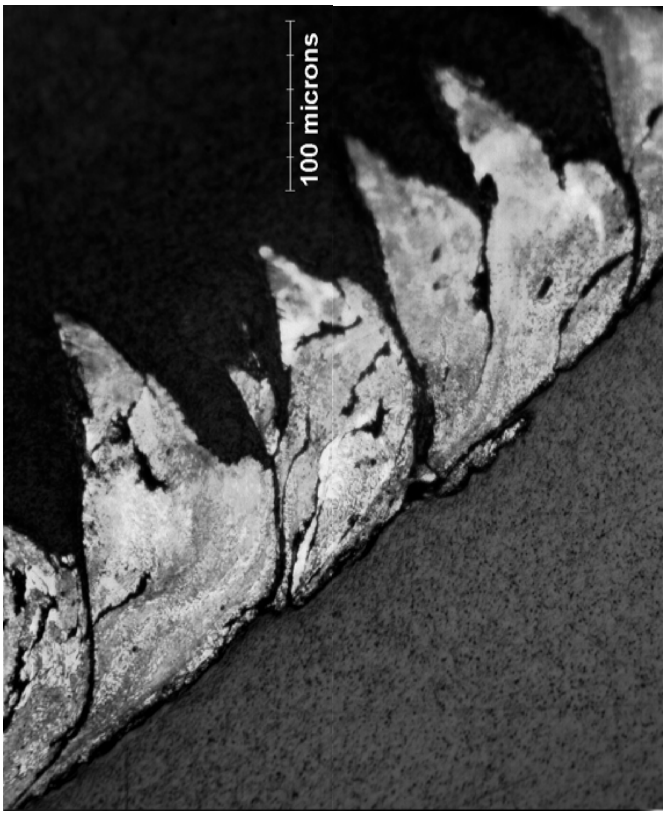

Figure 55 Segmental chip cross-section at middle chip plane

The asymmetric chip segments and low shear strain between segments shown in **Figure 55** suggest that formation of segments is initiated by crack formation at the graphite particles. As graphite is mainly the crack initiating constituent in the chip, the randomly distributed graphite particles throughout the matrix defer the complete separation of segments across the chip width, as shown in **Figure 56**. As can be seen in **Figure 56** and **Figure 57**, separation of chip segments is prevented by the incomplete crack growth across the chip thickness. Incomplete transverse cracks are pointed at with the white arrows in **Figure 57**.The incomplete microcracks closer to the chip-tool zone is promoted by the increase in the matrix bridge width as the feed rate is increased. Accordingly,

increasing the feed rate will relatively promote longer segmented chip. Naturally, segments will eventually tend to break due to the weak matrix bridges across the chip thickness.

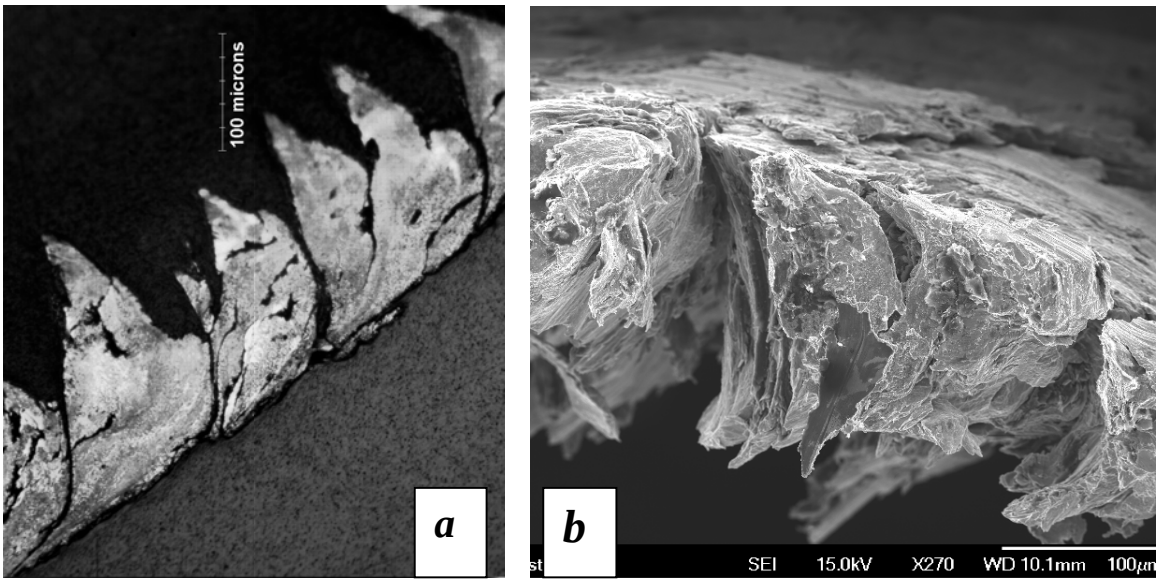

Figure 56 Chip segments showing incomplete separation in some chip segments (a), partial chip segmentation in a SEM image due to random distribution of graphite particles across the chip thickness (b) at 0.1 mm/rev @ 200 m/min.

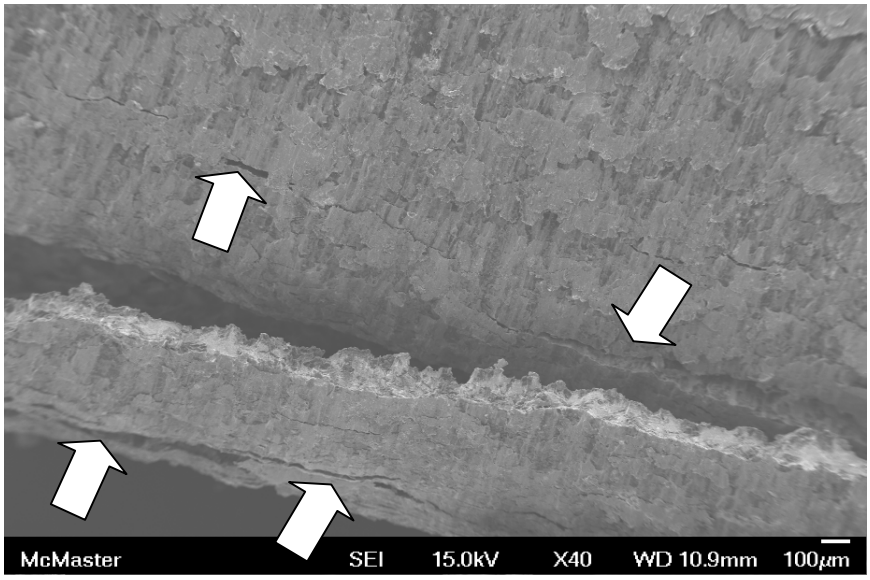

Figure 57 Incomplete transverse cracks due to the random distribution of the graphite particles across the chip

Finite element simulated chips are shown in **Figure 58**, **Figure 59**, and **Figure 60** for the three feed rates (0.05, 0.1, and 0.2 mm/rev.) at 400 m/min.

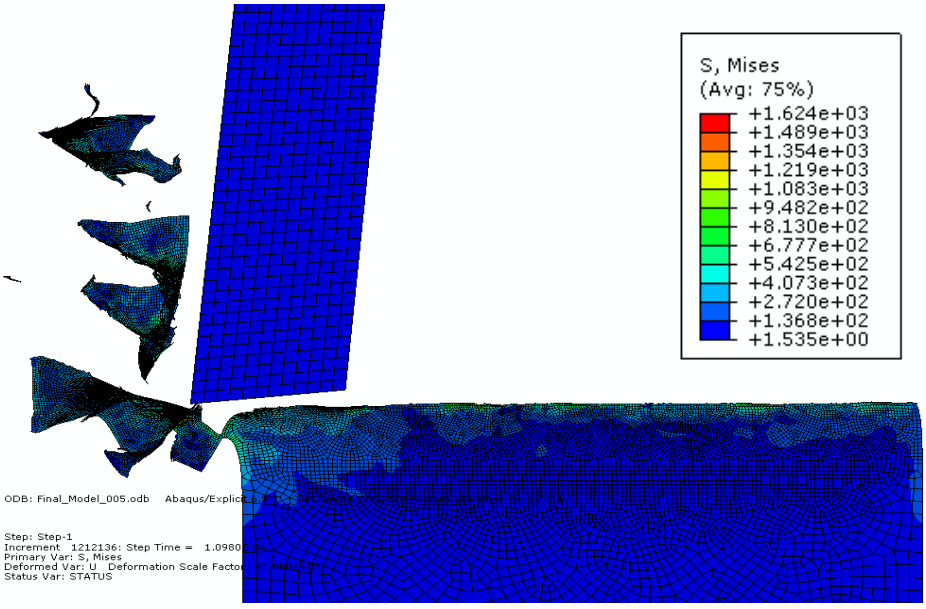

Figure 58 FE simulated segmental chip @ feed rate 0.05 mm/rev. @ 400 m/min.

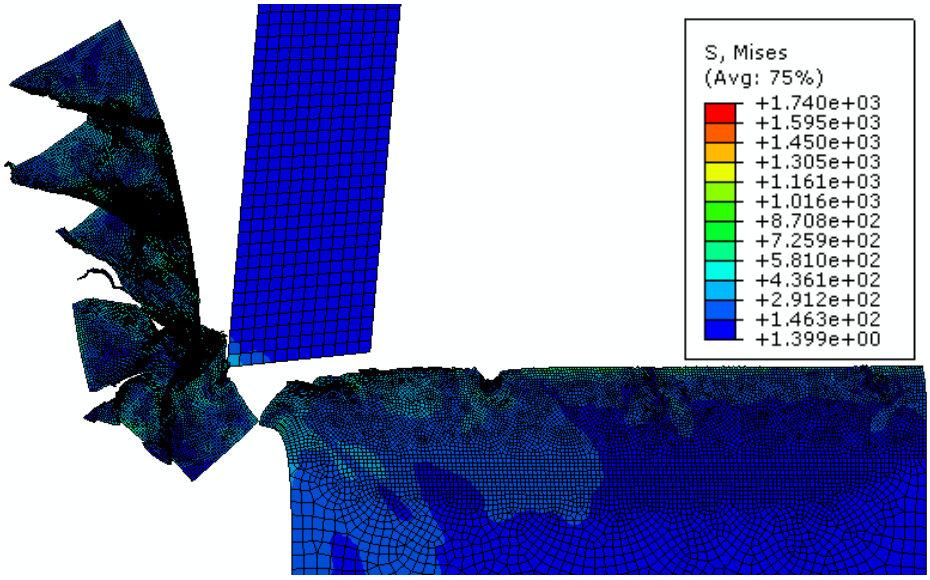

Figure 59 FE simulated segmental chip @ feed rate 0.1 mm/rev. @ 400 m/min

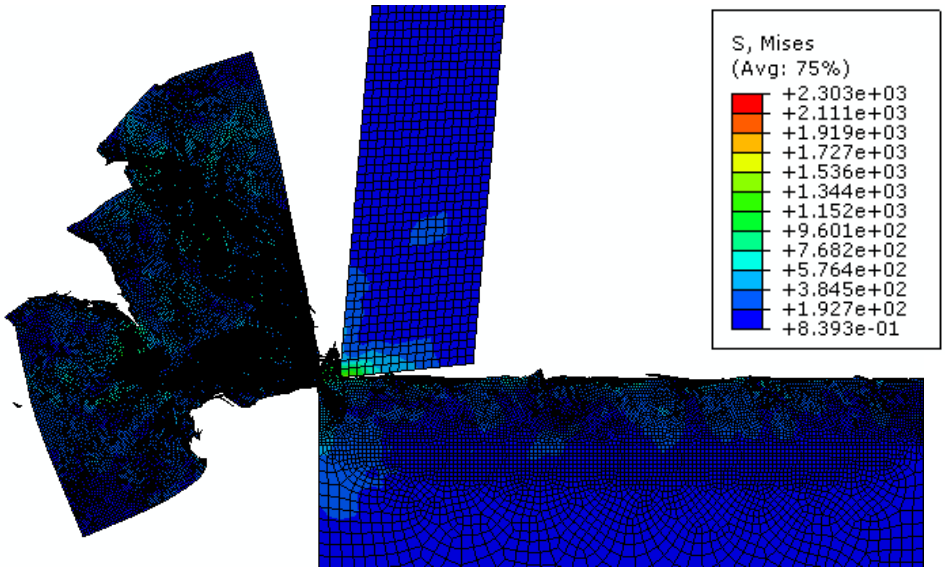

Figure 60 FE simulated segmental chip @ feed rate 0.2 mm/rev. @ 400 m/min

Simulated and machined chip segments are shown in **Figure 61** comparison. Severe plastic deformation is shown in both the finite element model and machined chips at the

chip-tool side (secondary shear zone).

Higher plastic strain is present in the finite element model chip at the secondary shear zone as shown in **Figure 61**. Lower plastic strain at the chip segments front side (in between two successive segments) where fracture is initiated at the graphite particles (white arrows) can be seen in the simulated and real chip images in **Figure 61**. It is also important to indicate the presence of incomplete chip segmentation due to the absence of graphite particle across the chip thickness at several locations in the simulated chip and real chip. To conclude, absence of graphite particles at some regions in the chip and high compressive stress associated with high temperature at the secondary shear zone prevent complete separation of chip segments.

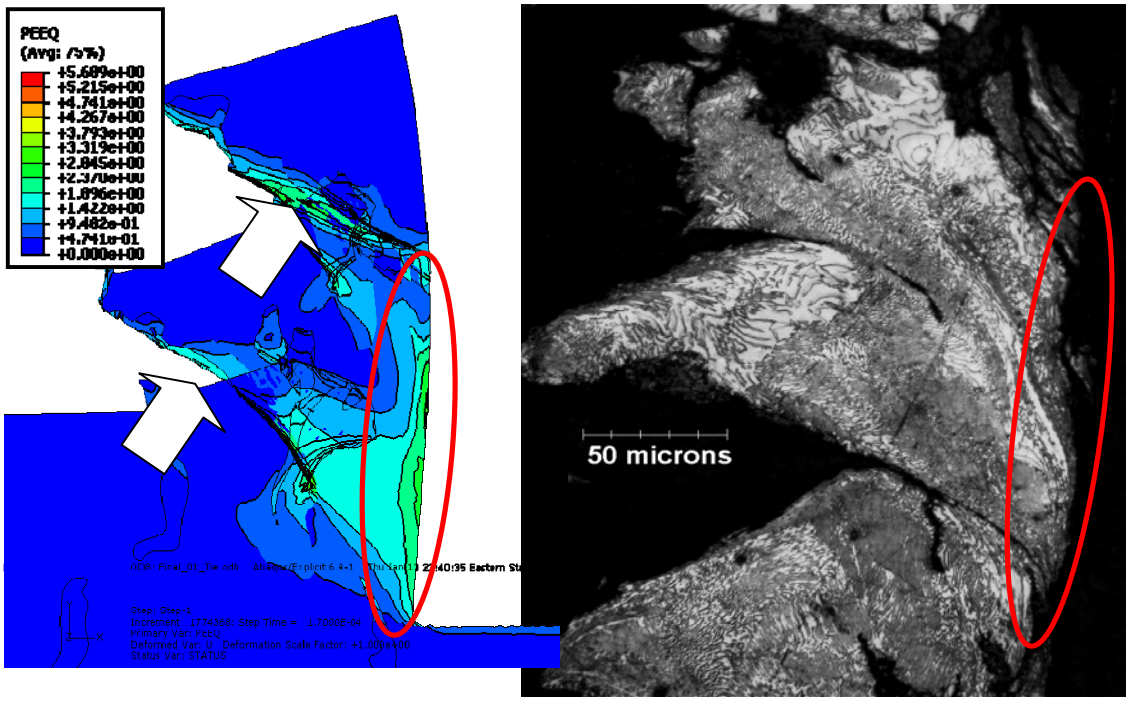

Figure 61 Simulated and real chip segments exhibiting severe plastic strain at the secondary shear zones, white arrows pointing at fracture planes. The real chip segments show the stretched pearlite contours at the SSZ.

7.3.3 The Graphite-Free Simulation

The finite element graphite-free model is used to validate the proposed model on other work material microstructure. The graphite-free model is closest in microstructure to a proposed AISI 1040 steel [207]. The graphite-free FE model does not differ from the proposed model except that the material properties of graphite constituent have been replaced with ferrite mechanical and thermal properties. As the model is initially built to allow crack initiation and propagation at any point in the chip, this is still adopted in the graphite-free model.

The criterion used in validating the proposed model is the consistency of the simulated chip with the actual machined chip. The characteristic segmental chip produced when machining CGI is due to the presence of graphite. Unlike in CGI, AISI 1045 chip is continuous when machined at “normal” cutting conditions. Allowing crack initiation to occur in the finite element model “mimics” the real machined chip. Hence, the main constituents in the graphite-free model are ferrite and pearlite.

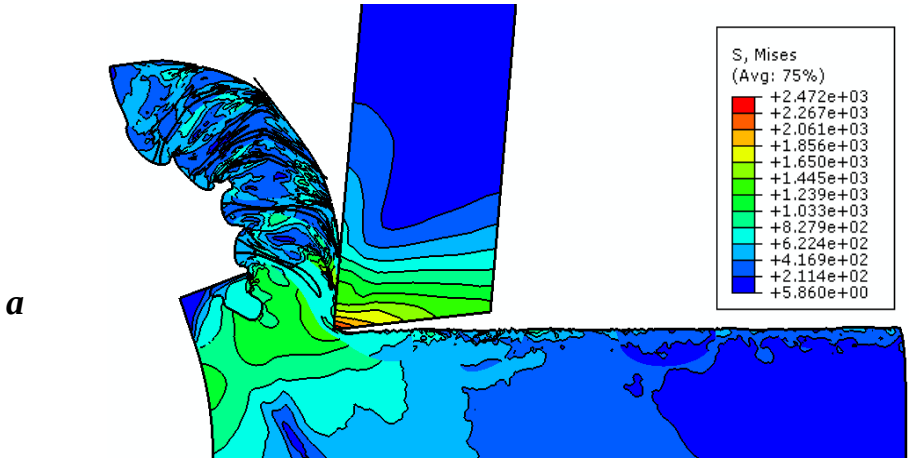

a

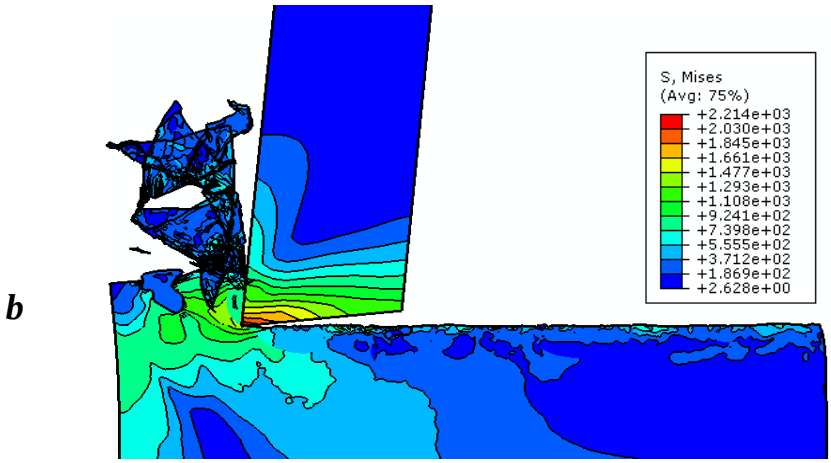

b

Figure 62 FE graphite-free models (a), CGI (b) (0.05 mm/rev @ 100 m/min.)

As shown in **Figure 62**, the FE simulation of the graphite-free material (AISI 1040) produces continuous chip despite the fact that crack initiation in the whole chip region is allowed in the model. As shown in **Figure 62(a),** crack initiation and propagation occur only at the chip-workpiece separation surface allowing only for chip separation. The graphite-free model does not show any crack within the chip body. In addition, the chip follows a characteristic form reported by other researchers [207] simulation as a result of the two constituents (ferrite and pearlite) only in the material. On the other hand, segmental chip is produced in the same finite element model when CGI is simulated due to graphite fracture presence **Figure 62(b).**

In addition to the chip characteristics in each material case, the *von Mises* stress is higher in the graphite-free material. The vulnerability of crack initiation is the reason for the lower *von Mises* and cutting forces predicted by the FE model shown in **Figure 63**.

Absence of segmental chip formation in the graphite-free model leads to less cutting force oscillation as compared to the proposed CGI model, as shown in **Figure 63**. However, the presence of pearlite and ferrite of varying mechanical and physical properties in the graphite-free material is the cause of the oscillation in **Figure 63**. Instantaneous separation between the chip and the tool tip is concurrent with drop in cutting force which occurs when the chip either slips on the tool rake surface or a chip fracture occurs. The extent of oscillation in the CGI simulated forces is basically due to the initiation, formation, and separation of segments as the tool goes through crack initiation and propagation sequence, shown in **Figure 48** .

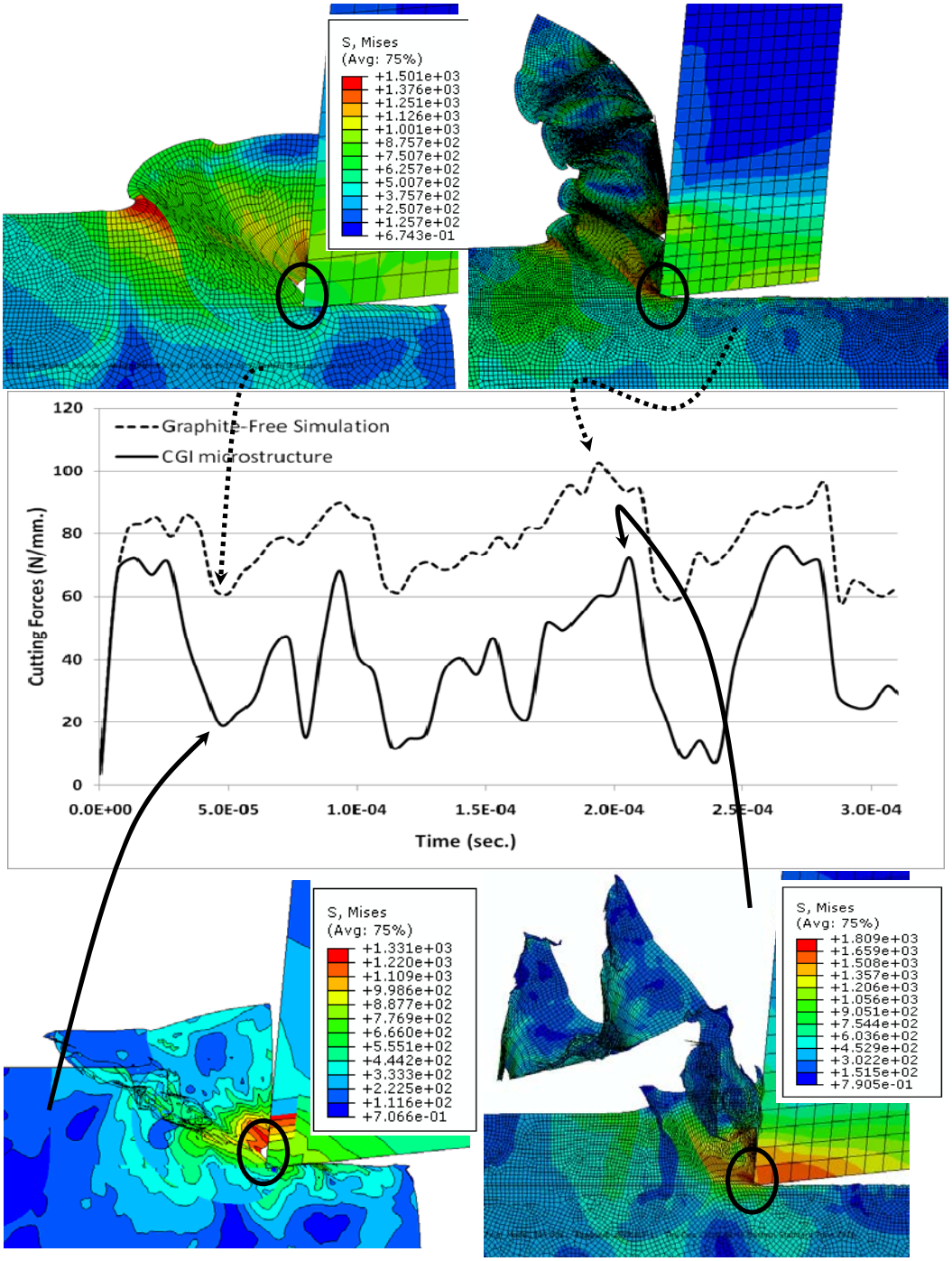

Figure 63 FE simulated graphite-free vs. CGI cutting forces (0.05 mm/rev. @100 m/min)

7.3.4 Effect of the microstructure of Compacted Graphite Iron on Tool Wear (results and Discussion)

7.3.4.1 Introduction

One purpose of tool wear investigation in the current work is to establish a trend which can be used to validate the proposed finite element model. Additionally, to establish a tool wear perception throughout the validation process which can be used (in the future) to optimize CGI machining. This tool wear perception will be based on analyzing the different effects of the machining conditions on the different cutting tool wear mechanisms.

The choice of the current tool configuration and material throughout this work plays a major role in the type and extent of the resulting wear. In addition, the currently used tool material properties, configuration, and machining conditions should be considered in the proposed finite element machining model in order to produce meaningful machining results. All the tool material properties are provided by the tool manufacturer.

7.3.4.2 Tool Wear Investigation

SEM preliminary examination of the cutting inserts reveals significant insert tip chipping at lowest cutting speed (100 m/min.) throughout all cutting feeds (0.05, 0.1, 0.2 mm/rev.). Tool tip chipping is significantly present in the rake face of the inserts. No accurate measurement of the tool tip chipping is performed to give a numerical assessment of its extent. However, the severity of tool tip chipping is most distinguishable at highest feed rate (0.2 mm/rev.) and lowest cutting speed (100 m/min) as shown in **Figure 64 (b)**.

Associated with these machining conditions, the cutting forces reach their maximum (F_c:157.5 N/mm, F_{th}:86.75 N/mm.). No insert tip chipping is found at cutting speed 400 m/min at feed rate 0.05 mm/rev., which is the case of minimal cutting forces (F_c:58.5 N/mm., F_{th}:28 N/mm.), shown in **Figure 64 (a)**. Insert rake chipping is not mainly controlled by the cutting forces alone. A trace of insert rake chipping is found at 200 m/min at 0.05mm/rev, but disappeared at the same cutting speed when the feed rate is increased. This is due to the dependency of the cutting temperature on the feed rate (depth of cut). As previously mentioned, increasing both of the cutting speed and the feed rate will significantly increase the cutting temperature decreasing the cutting forces and leading to less tip chipping.

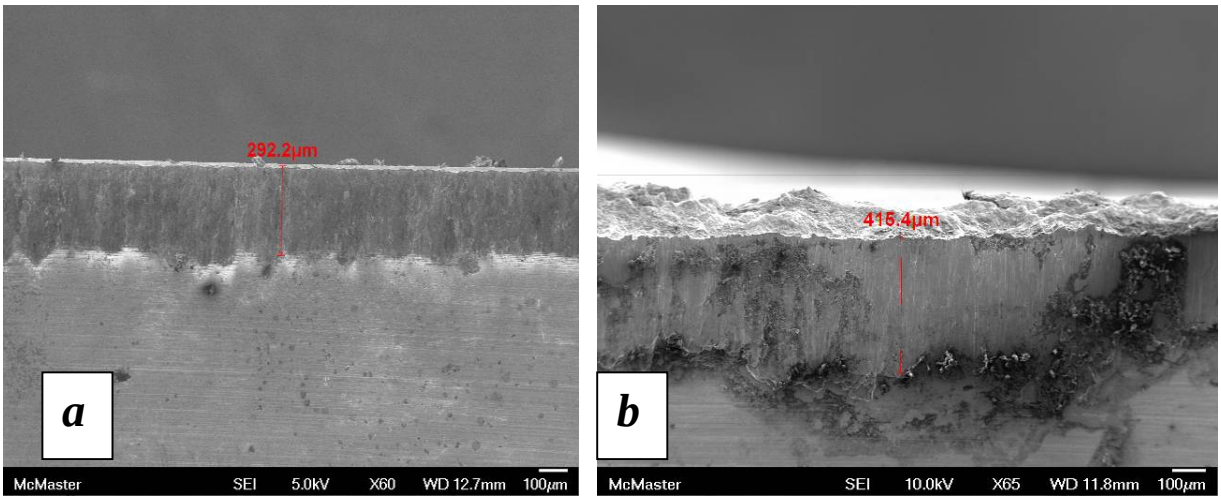

Figure 64 Cutting insert images showing the effect of lowest cutting forces 0.05 mm/rev-400 m/min. (a), highest cutting forces 0.2 mm/rev.-100 m/min. (b) on the tool wear type

Examination of the cutting insert flank surface at different feed rates and cutting speeds reveals varying extents of residual workpiece material attached (welded) to the inserts

flank surface. The extent of the attached residual workpiece material is measured on the SEM and shown in **Figure 65**.

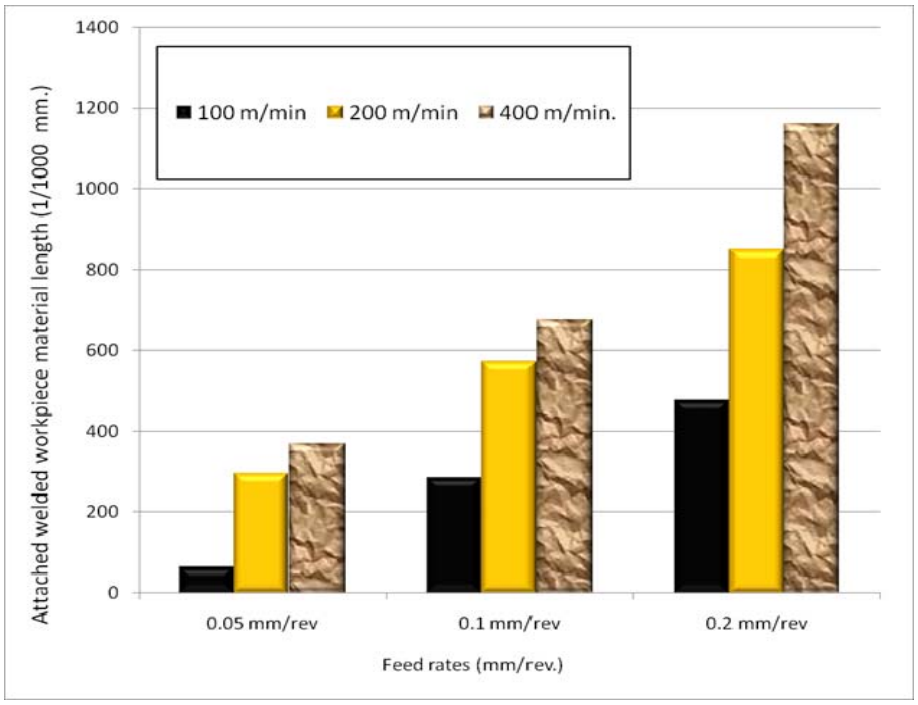

Figure 65 Average heights of workpiece material attached to the insert flank surface measured using SEM

The varying heights of the attached workpiece material are due to the varying cutting temperature at different cutting conditions (speeds and feeds). Naturally, as the cutting speed and feed rate increase, the cutting temperature is increased and more material is susceptible to attach to the insert flank surface, reaching it maximum at 0.2 mm/rev. and 400 m/min. as experimentally determined.

The tool tip chipping and flank surface attached workpiece material images at different cutting speeds and feed rates are shown in **Figure 66**. Visual examination of the tool images show a progressive trend of tip chipping as the feed rate increases from 0.05

mm/rev to 0.2 mm/rev at 100 m/min. Despite the moderate increase in the cutting temperature due to feed rate increase, the increase in cutting forces is more significant to cause the substantial tip chipping.

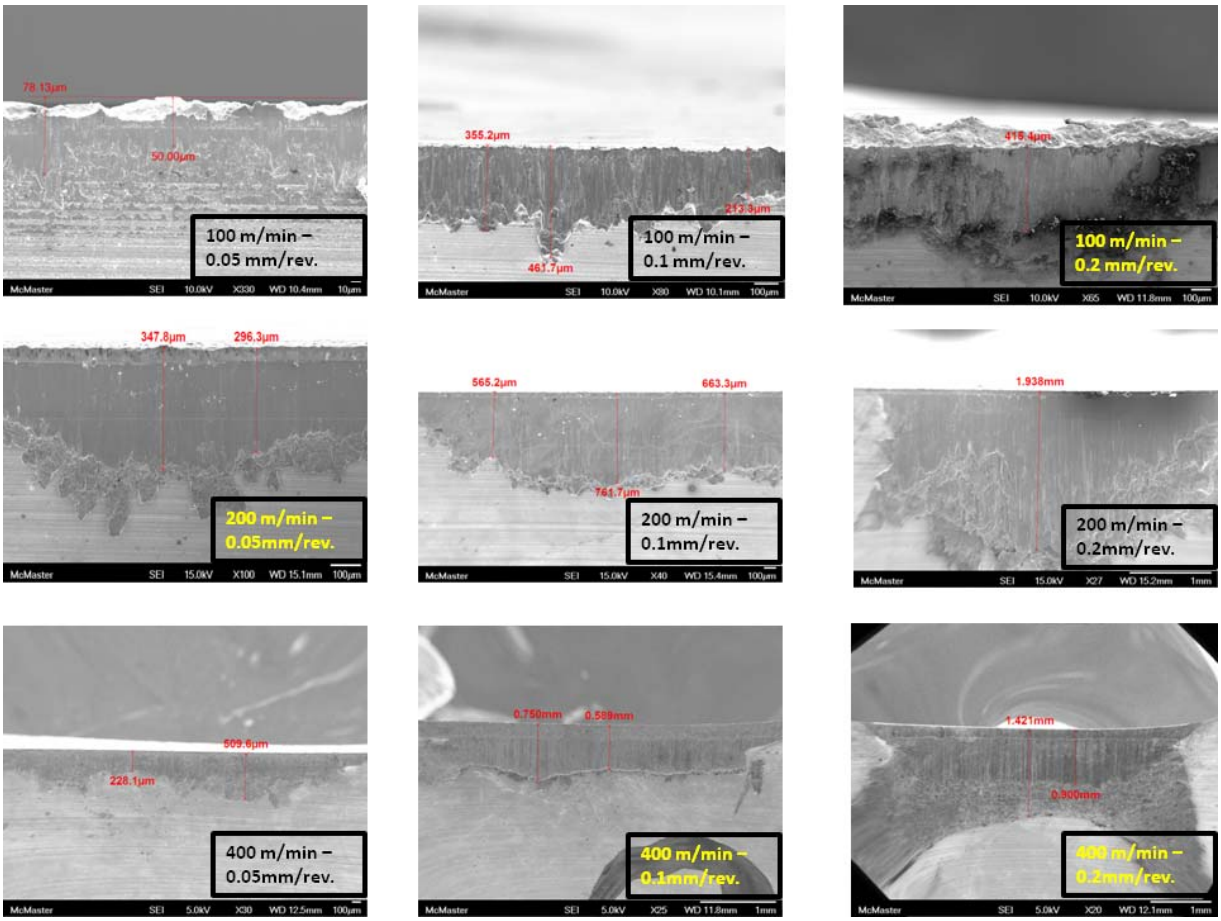

Figure 66 Tool wear images at different cutting speeds and feeds showing rake and flank wear characteristics. White arrows point to wear at the rake surface of the cutting insert.

Figure 67 represents the regions where the different tool wear mechanisms are more dominant based on the machining parameters. As the effect of the feed rate on the cutting

forces is more significant than on cutting temperature, and hence the propensity of tool tip chipping is higher toward higher feed rates and lower cutting speeds.

At cutting speed 200 m/min and feed rate 0.05 mm/rev a trace of tool tip chipping is found where the cutting force is about 70 N/mm. However, no tool tip chipping is present when the feed rate is increased where the cutting force is about 87 N/mm. This can be explained by that increasing the feed rate from 0.05 to 0.1 mm/rev. increases the cutting temperature at the workpiece-tool surface leading to wider chip flow contact area. At 0.05 mm/rev the cutting forces are distributed over a certain tool tip region. At feed rate 0.1 mm/rev. the distribution of the cutting forces occurs over a wider tool edge resulting in a lower applied stress. In conclusion, both cutting forces and cutting temperature together control the tool tip chipping phenomenon, though differently.

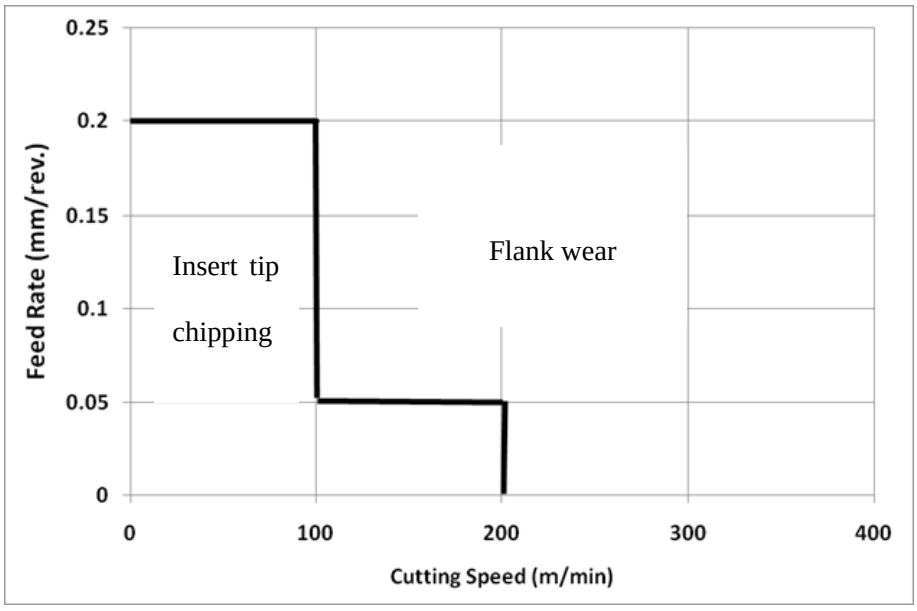

Figure 67 Feed rate vs. cutting speed chart where different tool wear mechanisms are more dominant.

7.3.5 The Finite Element Machining Model and Tool Wear

From the previous sub-section, it can be concluded that the cutting forces and the cutting temperature together control the type of tool wear mechanism at different cutting conditions. The effect of feed rate on the cutting forces is more significant than on the cutting temperature. It is inaccurate to relate the type of tool wear to one factor without considering the other, more specifically it is inaccurate to relate tool tip chipping to the cutting forces alone. Two competing factors (feed rate & cutting speed) are acting together to determine the resulting tool wear.

Despite the lack of tool wear numerical simulation, it is possible to rationalize the tool wear mechanism through the finite element machining model. More specifically, by considering both simulated cutting temperature and cutting forces together, it is possible to predict the tool wear mechanism. Simulated cutting temperature is shown in **Figure 68**.

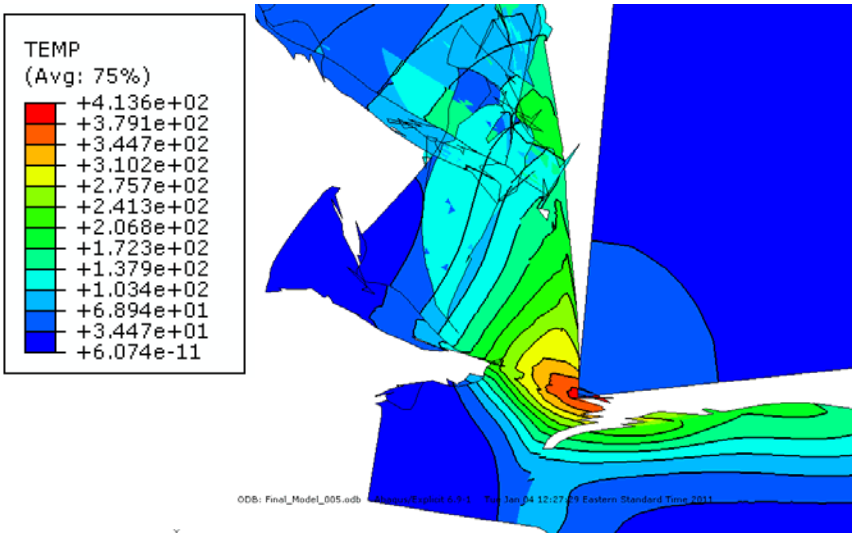

Figure 68 Cutting temperature distribution at 0.05 mm/rev. @ 400 m/min.

The cutting temperatures in the next graphs are the highest recorded simulated temperatures at the chip-tool interface.

From the FE model, at feed rate 0.05 mm/rev., increasing the cutting speed from 100 m/min to 400 m/min drives the cutting temperature from 252°C up to 408°C. The extent of tool flank surface welded material mainly depends on the cutting temperature and the feed rate. The simulated cutting temperature in **Figure 69 (a)** exhibits a steeper increase from 100 m/min to 200 m/min than from 200 m/min. to 400 m/min supporting the measured welded material pattern shown in **Figure 69 (b)**.

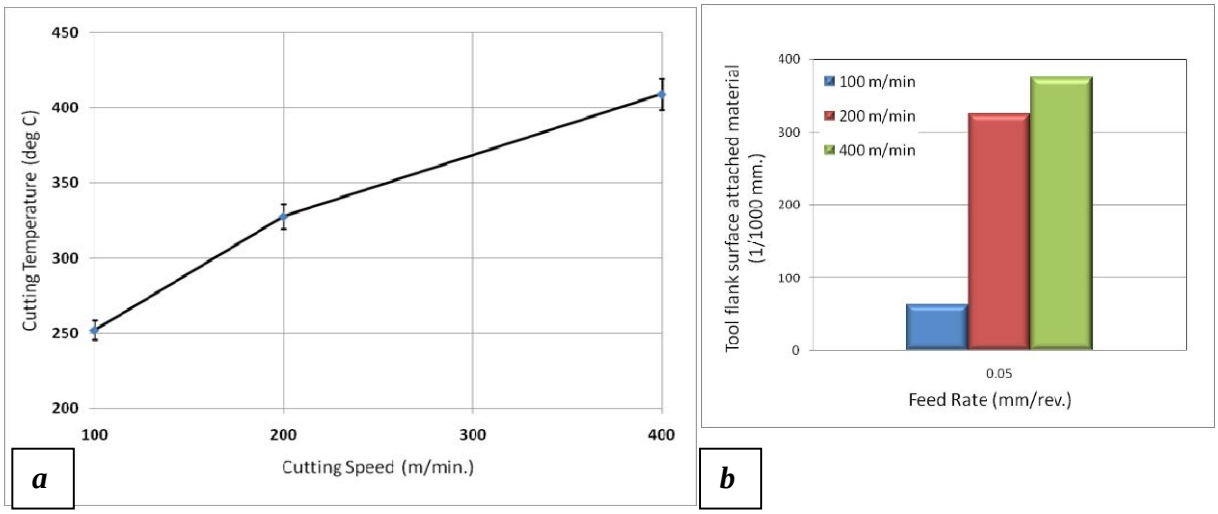

Figure 69 Simulated cutting temperature vs. cutting speed and at feed rate 0.05 mm/rev.(a), measured welded flank surface length (b)

Increasing the feed rate to 0.1 mm/rev. results in an increase in the simulated cutting temperature, as shown in **Figure 70 (a).** The simulated cutting temperature in **Figure 70 (a)** exhibits the same trend of the measured welded material pattern shown in **Figure 70 (b)**.

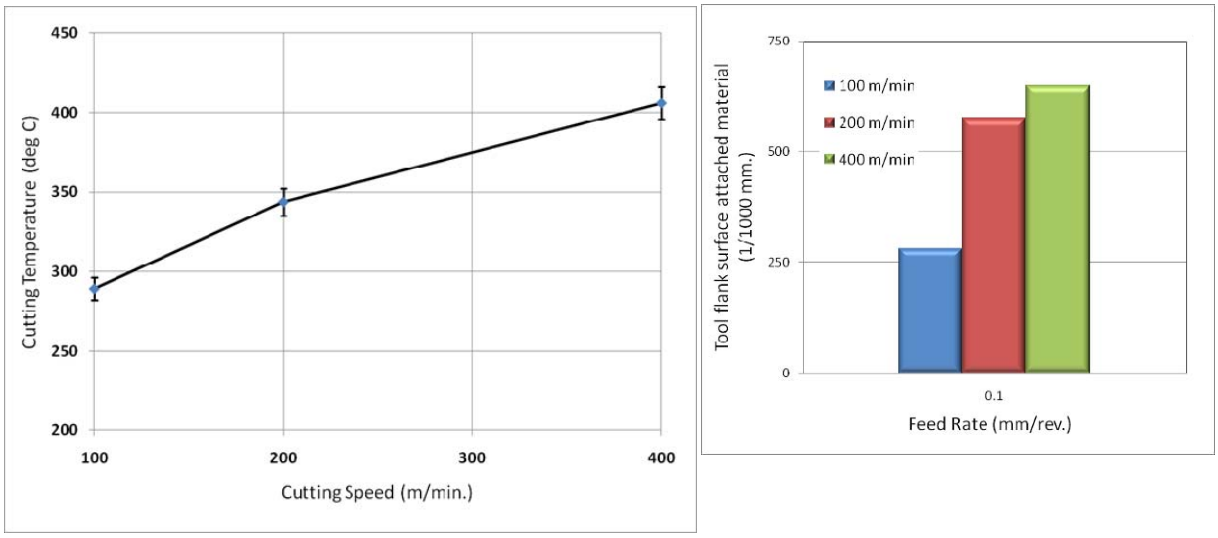

Figure 70 Simulated cutting temperature vs. cutting speed and at feed rate 0.1mm/rev. measured welded flank surface length (b)

Similarly, at feed rate 0.2 mm/rev, both simulated cutting temperatures and the measured tool flank surface attached material charts are shown in **Figure 71.**

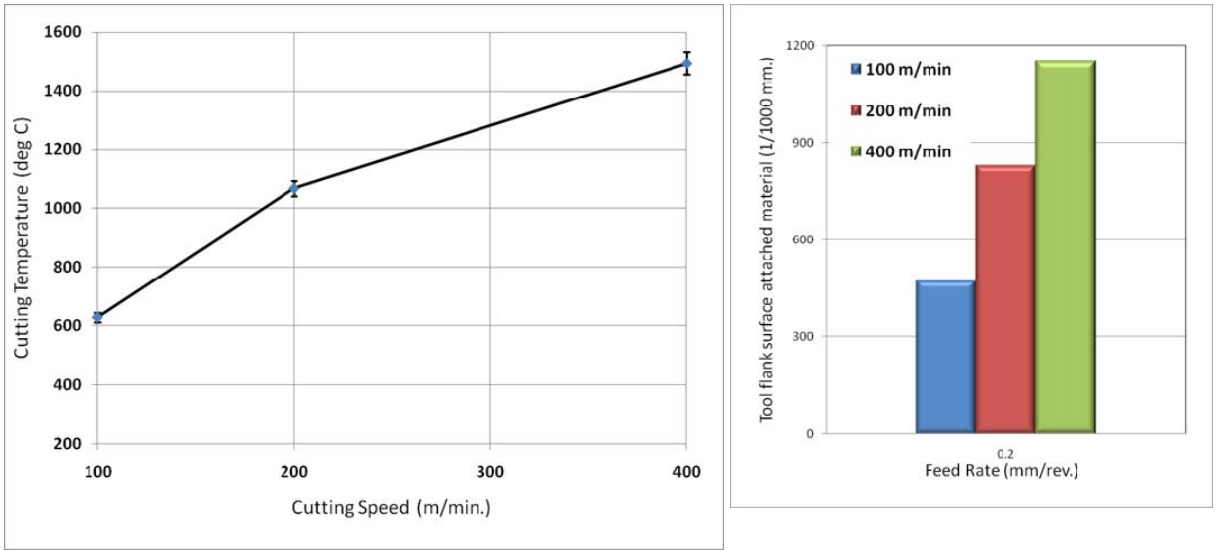

Figure 71 Simulated cutting temperature vs. cutting speed and at feed rate 0.2mm/rev. measured welded flank surface length (b)

CHAPTER 8
Conclusions and Recommendations for Future Work

8.1 Introduction

In the current work, fracture and machining of compacted graphite iron (CGI) have been studied, modeled, simulated, and validated. As it is impossible to experimentally simulate the microstructure behavior of CGI during fracture and machining, the proposed model simulates the microstructure of CGI validated by metallurgical experiments. In addition, the validated proposed model can be used as a fracture prediction tool and an optimization machining in the future.

The current chapter concludes the main findings of the current study. The conclusions are divided into two groups; 1) fracture and 2) machining. Following each group, the main contributions which have been achieved are then presented. As every work is an ongoing effort in pursuit of perfection, recommendations for future work are presented at the end of this chapter.

8.2 Conclusions

8.2.1 Phase 1: Finite Element Fracture Model of the microstructure of CGI

Fracture of compacted graphite iron is modeled using the Lagrangian description of motion. The finite element model simulates the middle section of the tensile test specimen loaded until fracture. The model is able to consider the characteristic morphology of graphite which is the key element to the superior performance of CGI.

The finite element model is able to capture the fracture initiation and propagation in CGI. Fracture initiates at the graphite particles ends and at the compacted graphite particles-matrix interface. The finite element model shows that graphite, which is the weakest material constituent, acts as favorite crack initiation localities in agreement with the experimental findings. The crack initiation at the graphite particles are validated by the real CGI samples through SEM investigation of the river patterns joining directions. The river patterns start at the graphite particles and join outward in the direction of fracture progress.

Introducing the cohesive zone technique into the finite element fracture model generates the bond between the graphite particles and the matrix as well as simulates the correct graphite-matrix decohesion phenomenon during fracture. According to the experimental investigation of the fractured samples, decohesion is found to dominate the nodular shaped graphite particles. On the other hand, intergraphite cracking is more dominant in the compacted graphite particles. This is due to the irregular compacted graphite particles boundaries leading to stronger graphite-matrix cohesion. In the finite element simulation,

decohesion shows to be more dominant in the less irregular graphite boundaries particles. Intergraphite fracture in the finite element simulation is found to be more dominant in the non-nodular graphite particles in a good agreement with the experimental findings.

The finite element model shows that fracture initiation occurs simultaneously at a number of graphite particles rather than progressively from one graphite particle to the next. As cracks initiate, they start to merge in the form of networks further forming the potential paths of failure. Such scenario is validated by the simultaneous fracture initiation and propagation in the real CGI samples.

The FE model is capable of simulating the crack bluntness phenomenon at the ferrite regions. In addition, due to crack tip bluntness, diversion of potential crack path is clearly shown in the finite element model. The characteristic morphology of graphite in the form of round edges of either nodular or compacted graphite particles associated with the extended plasticity of ferrite are the major causes of crack path diversion and crack bluntness. In the real test, as the microcracks initiate, the round compacted graphite particles work as crack arrestors blunting each microcrack tip leading to higher load carrying capacity. Further increase in strain joins the formed microcracks leading to the formation of the potential crack paths. This explains the sudden fracture response after a noticeable extent of plasticity with minimal reduction in cross section area prior to complete fracture in tensile specimen and in the finite element model. Fracture propagates in the direction of critical *Mises* stress as a result of excessive straining.

The finite element model is capable of generating the stress-strain curve until fracture and in a good agreement with the experimental results. The stress-strain curve exhibits the

stress-strain oscillation due to varying load carrying capacity as a result of the crack initiation and propagation in CGI until fracture. The simulated modulus of elasticity is within 0.013% of the experimentally determined modulus. The simulated tensile strength is 640 MPa versus the experimental 530 MPa strength due to strain rate difference justified by *Johnson-Cook* model.

The finite element model simulates the transverse microcracks occurred in the fractured specimens. Such transverse microcracks are present in the true fractured specimen as a result of the simultaneous crack initiation at different regions. Not all initiated cracks will propagate and join the potential crack paths where such transverse microcracks are arrested in the real sample due to either crack bluntness or grain boundaries.

In conclusion, the main causes of the enhanced load carrying capacity of compacted graphite iron are 1) the non-progressive initiation and propagation of cracks which prevent the concentration of failure that can lead to local instability, 2) bluntness of simultaneously initiated microcracks leading to diversion of potential crack paths, and 3) the presence of the ductile ferrite constituent which enhances crack bluntness and extends fracture strain before final failure. This scenario is simulated in the proposed finite element fracture model.

8.2.2 Phase 2: Finite Element Machining Model of the microstructure of CGI

Considering the proposed finite element fracture model as a foundation to the machining model, the machining model of compacted graphite iron is capable of simulating the machining process. Adopting the Lagrangian description of motion, the effect of the microstructure of CGI on cutting forces, chip formation, and cutting temperature is simulated and validated through experimental procedures.

8.2.2.1 Effect of the microstructure of compacted graphite iron on the cutting forces

The proposed finite element machining model is capable of simulating the studied cutting conditions of feed rates and cutting speeds. The simulated and measured cutting forces follow the same trend. Both simulated and measured cutting forces exhibit an acceptable matching steep increase in magnitudes within the same feed rate and cutting speed ranges.

The machining model is able to simulate the effect of the cutting speed and feed rate on the cutting forces. Increasing the cutting speed and the feed rate in the finite element simulation increases the cutting temperature and accordingly the cutting forces are decreased which is in agreement with the experimental measurements. In addition, the significant effect of the cutting speed compared to the feed rate on the cutting forces is simulated particularly at higher cutting speeds (200 – 400 m/min).

Despite the simulation of a perfectly sharp cutting insert tip, variation between the simulated and measured cutting forces is still within reasonable error range (10-15%)

based on the major bulk of relevant literature. The low simulated thrust (feed) forces are due to the simulation of a sharp cutting edge as a common practice in many finite element works. In addition, not considering the tool holder dynamics has an effect on the low simulated thrust forces values.

The finite element machining model is able to simulate the effect of CGI's microstructure on the cutting force oscillation. As CGI is a multiconstituent composition, unsteady cutting forces are experienced in experiment and in simulation. Simulated cutting forces reach their maximum prior to crack initiation in the graphite particles or prior to the graphite-matrix interface decohesion. On the other hand, simulated cutting forces reach their lowest magnitudes when the chip segment is completely separated from the workpiece. This simulation observation may not equally occur in magnitude in the real machining since the finite element model simulates a single plane of the workpiece. In real machining, graphite is randomly distributed within the workpiece in three-dimensional space and accordingly the cutting forces do not reach such low oscillation magnitude. Despite the fact that the finite element simulation is performed in the two-dimensional space, the overall simulated cutting forces are sufficiently comparable to the measure ones and follow the same trend.

8.2.2.2 Effect of the microstructure of compacted graphite iron on the chip characteristics

As the chip characteristics are used as a major validation criterion, the finite element simulated chip matches the machined chip. Firstly, the simulated chip is discontinuous and segmental which is in good agreement with the real chip. The simulated chip proves to be formed by fracture initiation and propagation rather than by adiabatic shear. Investigation of the actual chip shows that chip segmentation occurs at significantly low shear strain within the front free chip side. Severe shear strain is present at the chip-tool side (secondary shear zone) where the temperature significantly. Such chip segment characteristics are simulated by the finite element model. High PEEQ (equivalent plastic strain) values are found at the secondary shear zone in the finite element simulated chip segments due to the severely high temperature leading to extended fracture strain values.

The proposed machining model simulates the effect of the cutting speed on the chip segments characteristics. At lower cutting speed (100 m/min.) more discontinuous segments are produced as the cutting temperature is not high enough to increase the matrix flow strain causing complete fracture and separation of segments in reasonable agreement with the experimental results. The reason that this effect is not typically exhibited in the real chip is due to the inhomogeneous distribution of graphite across the chip. The graphite absence in some regions delays the complete separation of chip segments. Nonetheless, at higher cutting speeds (200 – 400 m/min) more matching chip characteristics are produced in both the simulated and the actual machined chips.

On the other hand, the effect of the feed rate (uncut chip thickness) is clearly simulated.

At lowest feed rate (0.05 mm/rev.) the segments are more disconnected especially at lowest cutting speed. Increasing the feed rate to 0.1 increases the number of connected segments reaching their longest at cutting speed 400 m/min. This is validated by comparison with the experimentally produced chip.

8.2.2.3 The Graphite-Free Model

The proposed finite element machining model is characterized by allowing crack initiation and propagation at any point within the chip region. In other words, cracks are allowed to occur anywhere in the chip region where the plastic strain reaches a critical criterion value based on the *Johnson-Cook* damage model. This is adopted in the current work as it simulates the segmentation of chip in a more realistic way.

The proposed FE model is used to simulate a previously researched material by *Simoneau et al.* [207]; AISI 1045. AISI 1045 machined chip results in continuous chip type. The proposed FE model is able to simulate the continuous AISI 1045-like chip. Separation of the chip occurs only at the workpiece machined surface. No segmentation or cracking within the chip region, as in CGI, occur in the chip region considering that the model allows for such features to take place, validating its applicability on other materials.

8.2.2.4 Effect of the microstructure of compacted graphite iron on the tool wear and cutting temperature

Validation of the proposed finite element machining model is performed through comparison of the cutting forces patterns and the chip formation characteristics. Despite the absence of tool wear simulation by the current model, the proposed finite element

machining model is able to rationalize the experimental tool wear characteristics.

Experimental examination of cutting inserts show that tool wear mechanisms are found to fall between tip chipping and flank wear by attrition, inclusively or exclusively, based on the machining variables. Tool wear by attrition is characterized by the attachment of workpiece material which over time will separate from the insert causing a loss in the tool insert material leading to degeneration in machined workpiece surface and increased cutting forces.

Tool wear by attrition is of thermal nature and increases as the temperature in the vicinity of the tool insert increases. Tool tip chipping is of mechanical nature and is increased as the cutting forces increase. Accurately analyzing the proposed finite element simulated cutting forces and temperature leads to good validation of the model and better understanding of the interacting causes of the different tool degeneration mechanisms.

Experimental assessment of the amount of the workpiece material attached to the tool flank surface shows an increasing trend of such amount as the cutting speed and feed rate increase. Such increase in the amount of the workpiece material is contingent upon the cutting temperature and the amount of workpiece material removed by the cutting insert (feed rate).

Despite the absence of experimental measurement of the cutting temperature, the simulated cutting temperature at the machined surface and the experimentally determined attached workpiece material heights, follow the same trend of relevance to both the cutting speed and the feed rate. Accordingly and based on the aforementioned logic, it can be inferred that the simulated and real cutting temperatures follow the same trend. From

there, it is legitimate to consider the simulated cutting temperatures for the purpose of model validation and to explain other relevant phenomena as will follow next.

Experimental investigation of the tool tip insert shows that tool tip chipping is most significant at cutting speed 100 m/min at all feed rates (0.05, 0.1, 0.2 mm/rev.), which is in good agreement with that highest simulated and measured cutting forces are at such cutting speed and confirming the effect of the cutting forces on tool tip chipping. Lowest simulated cutting temperature is recorded at the lowest cutting speed too. However, at cutting speed 200 m/min, a trace of tool tip chipping is found at feed rate 0.05 mm/rev. No tool tip chipping is observed when the feed rate is increased to 0.1 mm/rev. despite the resulting increase in the simulated and measured cutting forces. This can be reasoned by that the simulated cutting temperature is increased accordingly from 327°C to 343°C leading to an increased area of contact and accordingly lower tool tip stress preventing tip chipping.

The simulated cutting temperature shows a significant increase in magnitude as the simulated cutting speed is increased. In addition, the simulated cutting temperature at the machined surface shows a slight increase in magnitude as the feed rate increases too. On the other hand, simulated feed rates show more significant effect on the cutting forces than on the cutting temperature. Increasing the cutting speed and the feed rate together will encourage the domination of flank wear by attrition as the simulated cutting temperature shows an increasing trend. On the other hand, at lower cutting speeds the feed rate has a dominant effect on the cutting forces encouraging tool tip chipping. Both cutting forces and cutting temperature together control the type of tool wear mechanism.

Considering the lack of cutting temperature measurement, simulated cutting temperature elaborates on the effect of the cutting speed and feed rate on tool wear mechanisms.

8.3 Contributions

The main contributions of the current work can be summarized in the following:

1. Understanding the effect of the different constituents of compacted graphite iron microstructure on plasticity, strength, thermal conductivity, thermal expansion, and other uniquely superior properties. In addition, understanding the role of the characteristic morphology and growth mechanism of compacted graphite in the unique performance of compacted graphite iron.
2. Understanding fracture initiation and propagation mechanisms in compacted graphite iron. As it is impossible to experimentally monitor crack initiation and propagation until failure, the proposed finite element model can simulate the fracture process and serves as a tool for future material performance optimization. Such optimization includes variation of the microstructure constituents' percentages, morphologies, and type of graphite particles.
3. As the main cause of the unique performance of compacted graphite iron is due to its characteristic microstructure, the current work establishes the ability to model the multiphase compound under different loading scenarios. The current work establishes a modeling technique which introduces the cohesive zone elements. Cohesive zone elements present a realistic technique to model interface decohesion of the graphite particles and the matrix. The current work establishes a systematic methodology to

build cohesion/decohesion zone based on metallurgical basis.

4. Developing a machining model which can successfully simulate the machining process of different microstructure materials. The proposed model considers the microstructure of the simulated material and simulates the correct chip formation characteristics, cutting forces, and cutting temperature to a practically accepted accuracy.
5. Understanding the effect of the cutting speed and feed rate on the resulting tool wear mechanisms in compacted graphite machining. The effects of such machining variables are used to elaborate on the underlying controlling factors; cutting forces and cutting temperature on tool wear mechanism.

8.4 Recommendations for Future Work

In light of the current work, following points out possible future research venues:

1. The current work elaborates on the different growth mechanisms of carbon in compacted graphite and nodular graphite particles. As compacted graphite iron mechanical and physical properties change in response to the percentage of each graphite type, it is recommended that each graphite type mechanical and physical properties may be experimentally determined to a reasonable accuracy and included in both fracture and machining models. This will provide a more accurate understanding of the role of each graphite type in fracture and machining.
2. As graphite is one major participant to the performance of compacted graphite iron, determination of the mechanical and physical properties of graphite at high

strain magnitudes, high strain rates, and elevated temperature will introduce new *Johnson-Cook* variables to graphite which will be more physically accurate. The the current work points out to the strengthening of graphite at a certain range of high temperature, such phenomenon may elaborate on the extended strength of compacted graphite iron at elevated temperatures.

3. Extending the machining model to include different cutting tool materials, tool geometries and configurations (angles, edge preparation, etc..), coatings at different machining conditions (cutting speeds, feed rates, dry/coolant condition simulation) to study the effect of all variables on machining outputs.
4. Extend the machining model to include a tool material degeneration model to simulate the tool wear mechanisms at the different machining conditions in recommendation #3.
5. Extend the machining model to consider the effect of hard minor constitutes percentage present in the metal matrix such as titanium carbide, magnesium sulfide, aluminum oxide, on the tool wear progress.

PUBLICATIONS

During the course of this work, the following works have been accepted for publications by the corresponding international scientific journals:

1. Walid M. Mohammed, Eu-Gene Ng, M.A. Elbestawi, (2011), “On stress propagation and fracture in Compacted Graphite Iron”, International Journal of Advanced Manufacturing Technology, volume 56, numbers 1-4, 233-244
2. Walid M. Mohammed, Eu-Gene Ng, M.A. Elbestawi, (2011), “Modeling the Effect of the microstructure of Compacted Graphite Iron on Chip Formation”, International Journal of Machine Tools and Manufacture, volume 51, issue 10-11, 753-765
3. Walid M. Mohammed, Eu-Gene Ng, M.A. Elbestawi, “Modeling The Effect of the Microstructure of Compacted Graphite Iron on Cutting forces and Tool Wear”, CIRP Journal of Manufacturing Science and Technology (revision under review).
4. Walid M. Mohammed, E. Ng, M.A. Elbestawi, (2011)“Effect of the cohesive zone model on the predicted cutting forces and tool wear in compacted graphite iron Machining”, Finite Elements in Analysis and Design (submitted).

REFERENCES

[1] S. Dawson,I. Hollinger,M. Robbins,J. Daeth,U. Reuter, and H. Schults, (2001),"The effect of metallurgical variables on the machinability of compacted graphite iron", Automotive Casting Processes and Materials, SP-1603, Warrendale, PA, USA, Society of Automotive Engineers, 41-59

[2] S. Skvarenina, and Y. C. Shin. (2006), "LASER-assisted machining of compacted graphite iron", International Journal of Machine Tools and Manufacture, **46**, Compendex, 7-17

[3] F. Mocellin,E. Melleras,W.L. Guesser, and L. Boehs. (2004), "Study of the machinability of compacted graphite iron for drilling process", J of the Braz Soc of Mech Sci & Eng, **XXVI, No. 1**, 22-27

[4] A. Needleman. (1987), "A continuum model for void nucleation by inclusion debonding", J Appl Mech-Trans ASME, **54**, 3, 525-531

[5] D. M. Stefanescu. (2005), "Solidification and modeling of cast iron - A short history of the defining moments", Mater Sci Eng A, Struct Mater, Prop Microstruct Process (Switzerland), **413-414**, 322-333

[6] William D. Callister. (2007),"Materiais science and engineering: an introduction ", 7th ed. New York, John Wiley and Sons.

[7] J.R. Davis, (1998), "Metals Handbook, Desk Edition - ASM International Handbook Committee", 2nd edition CRC Press, West Conshohocken, PA, 1535

[8] ASTM Standards A247-67, (1971), "Standard test method for evaluating the microstructure of graphite in iron castings", ASTM International, West Conshohocken, PA, www.astm.org

[9] J.C. Hamaker,W.P. Woods, and F.B. Rote. (1952), "Internal porosity in gray iron", **60**, 401-427

[10] British Cast Iron Research Association (BCIRA), (1981), "Effect of some residual or trace elements on cast iron", Broadsheet 192, BCIRA, Alvechurch, Birmingham, England,

[11] T. SJÖGREN. (2007), "Influences of the graphite phase on elastic and plastic deformation behavior of cast iron", Department of Mechanical Engineering Component Technology - Castings, Linkoping University, Jönköping, Sweden

[12] I.C.H. Hughes. (1978), "Ductile Iron".ASM International, ASM Handbook, Casting. West Conshohocken, PA, **15**, 1405

[13] A.G. Fuller. (1977), "Evaluation of the graphite form in pearlitic ductile Iron by ultrasonic and sonic testing and the effect of graphite form on mechanical properties", Trans AFS, **85**, 509-526

[14] B. Lux,W. Bollmann, and M. Grages. (1969), "On the structure of graphite in pure Fe-C-Si alloys", Praktische Metallographie, **6**, 530-535

[15] British Cast Iron Research Association (BCIRA), (1976), "Principal forms of graphite in cast Irons, Figure 4", Broadsheet No 138, BCIRA, Alvechurch, Birmingham, England,

[16] H. Morrogh, and W.J. Williams. (1946-47), "Graphite formation in gray cast iron", Proceedings of the Institute of British Foundrymen, **40**, A47-63
[17] D.K. Millis,A.P. Gagnebin, and N.B. Pilling. "Grey cast iron having improved properties". US(1949)
[18] R.W. Lindsay, and A. Shames. (1952), "Effect of percentage of nodular graphite on certain mechanical properties of magnesium-treated cast iron", American Foundrymen's Society Transactions, **60**, 650-654
[19] J.V. Dawson,L.W. Smith, and B.B. Bach. (1953), "Some effects of Nitrogen in Cast Iron", BCIRA Journal of R & D, **4, No. 12**, 540-552
[20] F.A. Mountford. (1966), "The influence of nitrogen on strength, soundness and structure of grey cast iron", The British Foundryman, **69**, 141-151
[21] R.D. Shelleng. "Cast Iron with at least 50% of the Graphite in Vermicular Form and a Process for Making Same". USA(1969)
[22] R.D. Schelleng. (1966), "Effect of certain elements on the form of graphite in cast iron", AFS Transactions, **74**, 700-708
[23] J.V. Dawson, and E.R. Evans. (1974), "Compacted graphite irons produced by magnesium additions", BCIRA Journal, **22**, 136-144
[24] Yih-Hsun Shy,Cheng-Hsun Hsu,Shen-Chih Lee, and Chih-Yuan Hou. (2000), "Effects of titanium addition and section size on microstructure and mechanical properties of compacted graphite cast iron", Materials Science and Engineering A, **278**, Compendex, 54-60
[25] E.R. Evans,J.V. Dawson, and M.J. Lalich. (1977), "Compacted graphite cast Irons and their production by a single alloy addition", Transactions of the American Foundrymen's Society, **84**, 215-220
[26] Elkem Foundary Products. Oslo, Norway(2010) http://www.foundry.elkem.com/
[27] J. Warrick Robert,G. Ellis Gerald,C. Grupke Clifford,R. Khamseh Amir,H. McLachlan Theodore, and Gerkits Carrie. "Development and application of enhanced compacted graphite Iron for the bedplate of the new Chrysler 4.7 liter V-8 engine",
[28] K.P. Cooper, and C.R. Loper. (1978), "A critical evaluation of the production of compacted graphite cast iron", American Foundary Society, **86**, 267-272
[29] E. Campomanes, and R. Goller. (1975), "Production of cast iron containing intermediate forms of graphite", Transactions of the American Foundrymen's Society, **83**, Compendex, 55-62
[30] G. F. Ruff, and T. C. Vert. (1979), "Investigation of compacted graphite Iron using a high sulfur gray iron base", AFS Transactions, **87**, 459-464
[31] V.S.R. Murthy,Kishore, and S. Seshan. (1985), "Vermicular graphite cast Iron - current state of the art", Sadhana - Academy Proceedings in Engineering Sciences, **8-Part 4**, 361-372
[32] F. Martinez, and D. M. Stefanescu, (1983),"Properties of compacted/vermicular graphite cast irons in the Fe-C-Al system produced by ladle and in-mold treatment", Transactions of the American Foundrymen's Society, Proceedings of the Eighty-seventh Annual Meeting, Rosemont, IL, USA, AFS, **91**, 593-606
[33] D. M. Stefanescu. (1990), "Compacted graphite iron".ASM International, ASM

Handbook, Properties and selection: irons, steel, and high performance alloys. **01**, 102-129

[34] Sugwon Kim,S. L. Cockcroft,A. M. Omran, and Honam Hwang. (2009), "Mechanical, wear and heat exposure properties of compacted graphite cast iron at elevated temperatures", Journal of Alloys and Compounds, **487**, 1-2, 253-257

[35] C.R. Loper,M.J. Lalich,H.K. Park, and A.M. Gyarmaty, (1979), "Microstructure-mechanical property relationship in compacted/vermicular graphite cast iron", 46th International Foundary Congress, Madrid, Spain, **35**.

[36] D.M. Stefanescu,L. Dinescu,St. Craciun, and M. Poscu, (1979),"Production of vermicular graphite cast irons by operative control and correction of graphite shape", 46th International Foundary Congress, Madrid, Spain, **46**,

[37] N. P. Lillybeck,M.G. McKimpson,R.T. Wimber, and D.W. Donis. (1977), "An evlatuation of graphite-shape consistency in compact-flake-graphite iron from mechanical property data", AFS Transactions, **85**, 129-132

[38] Martin Selin,Daniel Holmgren, and Ingvar L. Svensson, (2010),"Effect of alloying elements on graphite morphology in CGI", 5th International Conference on Solidification and Gravity, September 4, 2008 - September 5, 2008, Miskolc-Lillafured, Hungary, Trans Tech Publications Ltd, **649**, 171-176

[39] D. Holmgren,R. Kallbom, and I. Svensson. (2007), "Influences of the graphite growth direction on the thermal conductivity of cast iron", Metallurgical and Materials Transactions A: Physical Metallurgy and Materials Science, **38A**, 2, 268-275

[40] M. Konig, and M. Wessen. (2010), "Influence of alloying elements on microstructure and mechanical properties of CGI", International Journal of Cast Metals Research, **23**, Copyright 2010, The Institution of Engineering and Technology, 97-110

[41] J. F. Wallace. (1975), "Effects of minor elements on the structure of cast irons", Transactions of the American Foundrymen's Society, **83**, Compendex, 363-378

[42] D.M. Stefanescu. (2009),"Science and engineering of casting solidification". New York, USA, Kluwer Academic/Plenum Publishers.

[43] D. D. Double, and A. Hellawell. (1995), "The nucleation and growth of graphite--the modification of cast iron", Acta Metallurgica et Materialia, **43**, 6, 2435-2442

[44] S.V. Subramanian,D.A.R. Kay, and G.R. Purdy. (1982), "Compacted graphite morphology control", Transactions of the American Foundrymen's Society, **90**, 589-603

[45] M. Konig. (2010), "Literature review of microstructure formation in compacted graphite Iron", International Journal of Cast Metals Research, **23**, 3, 185-192

[46] A. Velichko,C. Holzapfel, and F. Mucklich. (2007), "3D characterization of graphite morphologies in cast iron", Advanced Engineering Materials, **9**, 1-2, 39-45

[47] D Jedrzejczyk, and C Podrzucki. (1993), "Influence of sulphur on crystallization of the vermicular graphite in cast iron treated With cerium-alloy", Metall Foundry Eng, **19**, 1, 71-79

[48] P.C. Liu,C.R. Loper Jr,T. Kimura, and E.N. Pan. (1980), "Observations on the

graphite morphology of compacted graphite cast iron", AFS Transactions, **41**, 97-118

[49] P. Zhu,R. Sha, and Y. Li, (1984),"The physical metallurgy of Cast Iron", Stockholm, Sweden, 3-11

[50] I. Minkoff, and B. Lux. (1975), "Graphite growth from metallic solution", Compendex, 473-493

[51] A.N. Roviglione, and J.D. Hermida. (2004), "From flake to nodular: A new theory of morphological modification in gray cast iron", Metallurgical And Materials Transactions B, **35B**, 313-330

[52] I. Minkoff. (1979),"Graphite crystallization, chapter 1 in preparation and properties of solid state materials". New York, NY, Marcel Dekker Inc., **4**, 1-46.

[53] R.M. Bushong, and E.A. Neel, (1961),"Proceedings of the 5-th Conf. on Carbon", Oxford: Pergamon Press, **1**,

[54] E. Fitzer, and L.M. Manocha. (1998),"Carbon reinforcements and carbon/carbon composites", Christiane Messerschmidt R. Germany, Springer - Verlag Berlin Heidelberg.

[55] J.R. Dryden, and G.R. Purdy. (1989), "The effect of graphite on the mechanical properties of cast irons", Acta Metall, **37**, 7, 1999-2006

[56] J.P. Hirth, and J. Lothe. (1982),"Theory of dislocations", 2nd. edition ed. New York, NY, USA, John Wiley & Sons.

[57] P. C. Liu, and C. R. Loper, Jr., (1980), "Scanning electron microscope study of the graphite morphology in cast iron", Scanning Electron Microscopy, Copyright 1981, IEE, 407-418

[58] Y.S. Touloukian. (1970),"Thermophysical properties of matter". New York, NY, USA, IFI/Plenum, **2**.

[59] D. M. Holmgren,A. Dioszegi, and I. L. Svensson. (2006), "Effects of transition from lamellar to compacted graphite on thermal conductivity of cast iron", International Journal of Cast Metals Research, **19**, Copyright 2008, The Institution of Engineering and Technology, 303-313

[60] K.P. Cooper, and C.R. Loper. (1978), "Some properties of compacted graphite cast iron", Transactions of the American Foundrymen's Society, **86**, 241-248

[61] D.M. Stefanescu, and C.R. Loper Jr. "Recent progress in compacted/vermicular graphite cast iron field". Giesserei-praxis(1981),73-96,

[62] E. Nechtelberger,H. Puhr,J.B. van Nesselrode, and A. Nakayasu, (1982),"Cast iron with vermicular/compacted graphite-State of the art, development, production, properties, applications", 49th International Foundary Congress, Chicago, IL, USA, 1-39

[63] T. Sjogren,Peter Vomacka, and Ingvar L. Svensson. (2004), "Comparison of mechanical properties in flake graphite and compacted graphite cast irons for piston rings", International Journal of Cast Metals Research, **17**, Compendex, 65-71

[64] S. Dawson, (1999), "Compacted graphite Iron: mechanical and physical properties for engine design", Based on paper presented at: Werkstoff und Automobilantrieb (Materials in Powertrain VDI (Verein Deutscher Ingenieure),

Dresedn, Germany, Sintercast Inc., 1-20.

[65] S. Shao,S. Dawson, and M. Lampic. (1998), "The mechanical and physical properties of compacted graphite iron", Materialwissenschaft und Werkstofftechnik, **29**, Copyright 1998, FIZ Karlsruhe, 397-411

[66] L. Fang,K.E. Metzloff,R.C. Voigt, and C.R. Loper. (1995), "Factors affecting Measurement of Modulus of Elasticity of Ductile Irons", Transactions of the American Foundrymen's Society, **103**, 31-39

[67] G.F. Sergeant, and E.R. Evans. (1978), "The production and properties of compacted graphite irons", British Foundryman, **71(5)**, 115-124

[68] A. Spinner, and W.E. Teft, (1961),"A method for determining mechanical resonance frequencies and for calculating elastic moduli from these frequencies", Proceedings of the American Society for Testing & Matrials, **61**, 1221-1239

[69] J. D. Altstetter, and R. M. Nowicki, (1982),"Compacted graphite iron: Its properties and automotive applications", Transactions of the American Foundrymen's Society, Proceedings of the 86th Annual Meeting, Chicago, IL, USA, AFS, **90**, 959-970

[70] J. Sissener,W. Thury,R. Hummer, and E. Nechtelberger. (1972), "Cast iron with vermicular graphite", AFS Cast Metals Research Journal, 178

[71] E. Nechtelberger,H. Puhr,J.B. von Nesselrode, and A. Nakayasu, (1982), "Paper 1 presented at the 49th International Foundry Congress", International Committee of Foundry Technical Associations, Chicago, IL, USA.

[72] Lee Shen-Chih, and Chang Yin-Bean. (1991), "Fracture toughness and crack growth rate of ferritic and pearlitic compacted graphite cast irons at 25C and 150C", Metallurgical Transactions A (Physical Metallurgy and Materials Science), **22A**, Copyright 1992, IEE, 2645-2653

[73] J.P. Hrusovsky. (1982), "Formation, production and properties of compacted graphite iron", Ph.D. Thesis, Case western Reserve University, Cleveland

[74] I. Riposan,M. Chisamera,L. Sofroni, and V. Brabie, (1985),"Contributions to the study of the solidification mechanism and of the influence of structure on the properties of compacted/vermicular graphite cast iron", Physical Metallurgy of Cast Iron Proceedings of the Third International Symposium, 29-31 Aug 1984, New York, NY, USA, North-Holland, 131-140

[75] S. Hogmark, and J. Alander, (1983),"Wear of cylinder liners and piston rings", Wear of Materials 1983, Presented at the International Conference, Reston, VA, USA, ASME, 38-44

[76] M. Selin. (2010), "Tensile and thermal properties in compacted graphite irons at elevated temperatures", Metallurgical and Materials Transactions a-Physical Metallurgy and Materials Science, **41A**, 12, 3100-3109

[77] H.T. Angus. (1976),"Cast irons, physical and engineering properties", 2nd ed. London, UK, Butterworths.

[78] P. A. Blackmore, and K. Morton. (1982), "Structure-property relationships in graphitic cast irons", International Journal of Fatigue, **4**, 3, 149-155

[79] Young-Shin Lee,Jae-Ok Lee,Young-Jin Choi,Se-Hoon Lee,Hyun-Seung Lee,Joon-Tak Jun, and Jae-Hoon Kim. (2007), "Stress analysis of the heavy duty

diesel engine with compacted graphite iron", Key Engineering Materials, **345-346 II,** , 897-900

[80] E. Abele,A. Sahm, and H. Schulz. (2002), "Wear mechanism when machining compacted graphite iron", CIRP Annals - Manufacturing Technology, **51**, Compendex, 53-56

[81] M. Gastel,C. Konetschny,U. Reuter,C. Fasel,H. Schulz,R. Riedel, and H. M. Ortner. (2000), "Investigation of the wear mechanism of cubic boron nitride tools used for the machining of compacted graphite iron and grey cast iron", International Journal of Refractory Metals and Hard Materials, **18**, Compendex, 287-296

[82] A. Sahm,E. Abele, and H. Schulz. (2002), "Machining of compacted graphite iron (CGI)", Materialwissenschaft Und Werkstofftechnik, **33**, 9, 501-506

[83] J. V. C. Souza,M. C. A. Nono,O. M. M. Silva, and M. V. Ribeiro. (2008), "Comparative study on turning CI and CGI using silicon nitride cutting tools".Salgado L., filho F.A.Advanced Powder Technology Vi. Stafa-Zurich, Trans Tech Publications Ltd,**591-593**, 572-577

[84] N. Pretorius, and T. Toomey. (2007), "Evaluation of different cutting tool materials for the interrupted machining of compacted graphite cast iron", Industrial Diamond Review, **67**, Compendex, 41-44+47-48

[85] C.W. Phillip, (1982), "Machinability of compacted graphite iron", Transactions of the American Foundrymen's Society, Proceedings of the 86th Annual Meeting, Chicago, IL, AFS, Des Plaines, IL, USA,**90**, 47-52.

[86] D Sahm, (1997),"CGI-machining requirements in large-scale production", Proceedings of CGI design & manufacturing workshop, Bad Homburg, Germany,

[87] S. D. Rosa,A. E. Diniz,C. L. F. Andrade, and W. L. Guesser. (2010), "Analysis of tool wear, surface roughness and cutting power in the turning process of compact graphite irons with different titanium content", Journal of the Brazilian Society of Mechanical Sciences and Engineering, **32**, 3, 234-240

[88] R. O. Marwanga,R. C. Voigt, and P. H. Cohen. (1999), "Influence of graphite morphology and matrix structure on chip formation during machining of gray irons", Transactions of the American Foundrymen's Society, **107**, 595-607

[89] V. I. Izotov,V. A. Pozdnyakov,E. V. Luk'yanenko,O. Yu Usanova, and G. A. Filippov. (2007), "Influence of the pearlite fineness on the mechanical properties, deformation behavior, and fracture characteristics of carbon steel", Physics of Metals and Metallography, **103**, Compendex, 519-529

[90] E. R. Evans,J. V. Dawson, and M. J. Lalich. (1977), "Compacted graphite cast irons and their production by a single alloy addition", Transactions of the American Foundrymen's Society, **84**, Compendex, 215-220

[91] C. E. Bates. (1996), "Study examines influences on machinability of iron castings", Modern Casting, **86**, Compendex, 36-39

[92] R. C. Voigt,R. O. Marwanga, and P. H. Cohen. (1999), "Machinability of gray iron - Mechanics of chip formation", International Journal of Cast Metals Research, **11**, 6, 567-572

[93] D. Holmgren,A. Dioszegi, and I. L. Svensson. (2007), "Effects of nodularity on

thermal conductivity of cast iron", International Journal of Cast Metals Research, **20**, 1, 30-40

[94] A. Sahm,E. Abele, and H. Schults, (2002),"State of the art in CGI machining", Proceedings of the CGI Machining Workshop, Darmstadt, Germany,

[95] S. Dawson, and T. Schroeder. (2004), "Practical applications for compacted graphite iron", American Foundary Society transactions, **05**, 1-9

[96] S. Gabaldo,A. E. Diniz,C. L. F. Andrade, and W. L. Guesser. (2010), "Performance of carbide and ceramic tools in the milling of compact graphite iron - CGI", Journal of the Brazilian Society of Mechanical Sciences and Engineering, **32**, 5, 511-517

[97] E. Trent, and P. Wright. (2000),"Metal cutting". Woburn, Butterworth-Heinemann, 446.

[98] L. Scheidtweiler, (2000),"CGI machining with carbide tools", Proceedings of the machining workshop 2000 for compacted graphite iron, Institute of production engineering and machine tools, Darmstadt University of Technology, Contribution 1, Darmstadt, Germany,

[99] P. Ettmayer,H. Kolaska,W. Lengauer, and K. Dreyer. (1995), "Ti(C,N) cermets -- metallurgy and properties", International Journal of Refractory Metals and Hard Materials, **13**, 6, 343-351

[100] J. V. C. Souza,M. C. A. Nono,M. V. Ribeiro,O. M. M. Silva, and M. A. Lanna. (2008), "Turning of compacted graphite iron using commercial TiN coated Si3N4 under dry machining conditions", Advanced Powder Technology Vi, **591-593**, 604-609

[101] Niniza S. P. Diamini,Iakovos Sigalas, and Andreas Koursaris, (2008),"Cutting tool wear and mechanisms of chip formation during high-speed machining of compacted graphite iron", 2007 ASME/STLE International Joint Tribology Conference, IJTC 2007, October 22, 2007 - October 24, 2007, San Diego, CA, United states, American Society of Mechanical Engineers, **PART B**, 701-703

[102] Z. N. Farhat. (2003), "Wear mechanism of CBN cutting tool during high-speed machining of mold steel", Mater Sci Eng A-Struct Mater Prop Microstruct Process, **361**, 1-2, 100-110

[103] K. P. Varghese, and A. K. Balaji. (2007), "Effects of tool material, tool topography and minimal quantity lubrication (MQL) on machining performance of compacted graphite iron (CGI)", International Journal of Cast Metals Research, **20**, 6, 347-358

[104] H. Ernst, and M.E. Merchant. (1941), "Chip formation, friction, and high quality machined surfaces, surface treatment of metals", American Society of Metals, 299-378

[105] W.S. Lau, and C. Rubenstein. (1983), "The mechanics of continuous chip formation in oblique cutting in the absence of chip distortion, part 2 - comparison of experimental data with the deductions from theory", International Journal of Machine Tool Design and Research, **23**, 1, 21-37

[106] M. Merchant. (1945), "Mechanics of the metal cutting process II. plasticity conditions in orthogonal cutting", Journal of Applied Physics, **16**, 318-324

[107] C. Rubenstein. (1983), "The mechanics of continuous chip formation in oblique cutting in the absence of chip distortion, part 1- theory", Internation Journal of Machine Tool Design and Research, **23**, 1, 11-20

[108] M. EuGene Merchant. (1945), "Mechanics of the metal cutting process, I. orthogonal cutting and a type 2 chip", Journal of Applied Physics, **16, No. 5**, 267-275

[109] H. Ernst. (1937), "Physics of metal cutting", Machining of Metals, American Society for Metals, 24

[110] P.L.B Oxley. (1961), "A strain-hardening solution for the "shear angle" in orthogonal metal cutting", Int J Mech Sci, **3**, 68-79

[111] W.B. Palmer, and P.L.B. Oxley. (1959), "Mechanics of orthogonal machining", Proc Instn Mech Engrs, **173, No. 24**, 623-637

[112] W. Johnson. (1962), "Some slip-line fields for swaging or expanding, indenting, extruding and machining with curved dies", Int J of Mech Sci, **4**, 323-347

[113] P.L.B. Oxley, and M.J.M. Welsh, (1963), "Calculating the shear angle in orthogonal metal cutting from fundamental stress, strain, strain-rate properties of the work material", Proceedings 4th International Machine Tool Design and Research Conference, Pergamon, Oxford, 73-86.

[114] W.F. Hastings,P. Mathew, and P.L.B. Oxley. (1981), "A machining theory for predicting chip geometry, cutting forces, etc., from work material properties and cutting conditions", Proceedings of the Royal Society of London, **A371**, 569-587

[115] P.L.B. Oxley, and W.F. Hastings. (1976), "Minimum work as a possible criterion for determining the frictional conditions at the tool/chip interface in machining", Philosophical Transactions of the Royal Society of London, **282**, 565-584

[116] P.L.B. Oxley. (1961), "Mechanics of metal cutting", Int J Mach Tool Des Res, **1**, 89-97

[117] E.H. Lee, and B.W. Shaffer. (1951), "The theory of plasticity applied to a problem of machining", Trans ASME, Journal of Applied Mechanics, **18**, 405-413

[118] P.L.B Oxley, and A.P. Hatton. (1963), "Shear angle solution based on experimental shear zone and tool-chip interface stress distributions", Int J Mech Sci, **5**, 41-55

[119] K. Nakayama,M. Arai, and K. Takei. (1983), "Semi-empirical equations for three components of resultant cutting force", Annals of CIRPS, **30, No. 1**, 33-35

[120] H.J. Fu,R.E. DeVor, and S.G. Kapoor. (1984), "A mechanistic model fot the prediction of the force system in face milling operations", ASME Journal of Engineeing for Industry, **106**, 81-88

[121] G.R. Subramani,R. Suvada, and S.G. Kapoor. (1987), "A model for the prediction of force system for cylinder boring process", Proc NAMRC, **15**, 439-446

[122] W.J. Endres,R.E. DeVor, and S.G. Kapoor. (1993), "A dual-mechanism approach to the prediction of machining forces, Part 1 and Part 2", Proc, ASME Sym on Modeling, Monitoring and Control Issues in Manufac, , **64**, 563-593

[123] C.E. Becze. (2002), "A thermo-mechanical force model for machining hardened steel", Ph.D. Thesis, Mech Eng Dept, McMaster University, Hamilton

[124] V. Chandrasekharan,S.G. Kapoor, and R.E. DeVor. (1993), "A mechanistic

approach to predicting the cuttin forces in drilling: with application to fiber-reinforced composite materials", Proc Machining of Advanced Composites, **45**, 33-51

[125] B.E. Klamecki. (1973), "Incipient chip formation in metal cutting", Ph.D. Thesis, University of Illinois at Urbana Champaign, Urbana Champaign

[126] E. Usui, and T. Shirakashi, (1982),"Mechanics of machining - from descriptive to predictive theory", On the Art of Cutting Metals - 75 Years Later, A Tribute to F W Taylor Presented at the Winter Annual Meeting of the American Society of Mechanical Engineers, Phoenix, AZ, USA, ASME, **7**, 13-35

[127] T. Shirakashi, and E. Usui, (1974),"Simulation of orthogonal cutting mechanism", Proceedings of International Conference of Production Engineering, Tokyo, Japan, 535

[128] K. Iwata,K. Osakada, and Y. Terasaka. (1984), "Process modeling of orthogonal cutting by rigid-plastic finite element method", ASME Journal of Engineering Material and Technology, **106**, 132-138

[129] M. G. Stevenson,P. K. Wright, and J. G. Chow. (1983), "Further developments in applying the finite element method to the calculation of temperature distribution in machining and comparison with experiment", Journal of engineering for industry, **104**, Compendex, 149-154

[130] A. O. Tay,M. G. Stevenson, and G. de Vahl Davis. (1974), "Using the finite element method to determine temperature distribution in orthogonal machining", Proceedings of the Institution of Mechanical Engineers (London), **188**, Compendex, 627-638

[131] M.R. Lajczok. (1980), "A Study of some aspects of metal machining using finite element method", Ph.D. Thesis, North Carolina State University,

[132] K. Okushima, and Y. Kakino. (1971), "The residual stress produced by metal cutting", Annals of CIRP, **20**, 1, 13

[133] K. Okushima, and Y. Kakino. (1972), "A study on the residual stress produced by metal cutting", Memoirs of the Faculty of Engineering, Kyoto University, **34**, Copyright 1973, IEE, 234-248

[134] R. Natarajan, and S. Jeelani, (1983),"Residual stresses in machining using finite element method", Computers in Engineering 1983, Proceedings of the 1983 International Computers in Engineering Conference and Exhibit, Chicago, IL, USA, ASME, **3**, 79-80

[135] John S. Strenkowski, and J.T. Carroll III, (1986),"An orthogonal metal cutting model based on an Eulerian finite element method.", Proceedings of the 13th NSF Conference on Production Research and Technology, Manufacturing Processes, Machines and Systems,

[136] J.T. Carroll III. (1986), "A numerical and experimental study of single point diamond machining", Ph.D. Thesis, North Carolina State University,

[137] J. S. Strenkowski, and J. T. Caroll III, (1984),"Finite element model of orthogonal metal cutting", High Speed Machining Presented at the Winter Annual Meeting of the American Society of Mechanical Engineers, New Orleans, LA, USA, ASME, **12**, 157-166

[138] E.A Ceretti,P.B Fallböhmer,W.T.C Wu, and T.b Altan. (1996), "Application of 2D FEM to chip formation in orthogonal cutting", Journal of Materials Processing Technology **59**, 1-2, 169-180

[139] T.D. Marusich, and M. Ortiz. (1995), "Modeling and simulation of high-speed machining", International journal for numerical methods in Engineering, **38**, 3675-3694

[140] K. Maekawa, (1999),"Application of 3D machining modeling to cutting tool design", Proceedings of IInd CIRP Int'l workshop modeling of machining operations, Nantes, France,

[141] S.F. Wayne,C. Zimmerman, and D.A. O'Niel, (1993),"Aspects of advanced cutting tool and chip-flow modeling ", Proceedings of the 13th International Plansee Seminar, Reutte, Metallwerk Plansee, **2**, 64

[142] John S. Strenkowski, and K.J Moon. (1990), "Finite element prediction of chip geometry and tool/workpiece temperature distribution in orthogonal cutting", ASME Journal of Engineering for Industry, **112**, 313-318

[143] J. S. Strenkowski, and M. Kyoung-Jin, (1988), "A thermo-viscoplastic model of the cutting process including chip geometry and temperature prediction", North American Manufacturing Research Conference (NAMRX-XV), Bethlehem, Pennsylvania, SME, 197-205.

[144] J. S. Strenkowski, and G.L. Mitchum, (1987), "An improved finite element model of orthogonal metal cutting", Proceedings of North American Manufacturing Research Conference, SME, Bethlehem, Pennsylvania.

[145] O.C. Zienkiewicz, and P.N. Godbole. (1974), "Flow of plastic and visco-plastic solids with special reference to extrusion and forming processes", International journal for numerical methods in Engineering, **8**, 3-16

[146] O.C. Zienkiewicz, and I.C. Cormeau. (1974), "Visco-plasticity-plasticity and creep in elastic solids - a unified numerical solution approach", International journal for numerical methods in Engineering, **8**, 821-845

[147] O.C. Zienkiewicz, and P.N. Godbole. (1975), "A penalty function approach to problems of plastic flow of metals with large surface deformations", Journal of strain analysis for engineering design, **10**, 180-186

[148] O.C. Zienkiewicz,P.C. Jain, and E. Onate. (1978), "Flow of solids during forming and extrusion: some aspects of numerical solutions", International Journal of Solids and Structures, **14**, 15-38

[149] O.C. Zienkiewicz, and P.N. Godbole. (1975), "A penalty function approach to problems of plastic flow metals with large surface deformations", Journal of strain analysis for engineering design, **10**, 180-186

[150] Liu Wing Kam,Chang Herman,Chen Jiun-Shyan, and Belytschko Ted. (1988), "Arbitrary lagrangian-eulerian petrov-galerkin finite elements for nonlinear continua", Computer Methods in Applied Mechanics and Engineering, **68**, 3, 259-310

[151] M. Movahhedy,M. S. Gadala, and Y. Altintas. (2000), "Simulation of the orthogonal metal cutting process using an arbitrary Lagrangian-Eulerian finite-element method", Journal of Materials Processing Technology, **103**, 2, 267-275

[152] M. S. Gadala, and J. Wang. (1998), "ALE formulation and its application in solid mechanics", Computer Methods in Applied Mechanics and Engineering, **167**, 1-2, 33-55

[153] J. Donea,D.P. Fasoli-Stella, and S. Giuliani, (1977), "Lagrangian and eulerian finite element techniques for transient fluid-structure interaction problems", Trans SMiRT-4, Paper, San Fransisco, **B1/2**, 15-19.

[154] W.F. Noh. (1964),"A time dependent two space dimensional coupled Eulerian Lagrangian code", Alder B., Fernbach S., Rotenberg M. New York, Academic Press, **3**, 117-179.

[155] J. M. Huang, and J. T. Black. (1996), "An evaluation of chip separation criteria for the FEM simulation of machining", Transactions of the ASME Journal of Manufacturing Science and Engineering, **118**, Copyright 1997, IEE, 545-554

[156] Albert J. M. Shih,S. Chandrasekar, and Henry T. Y. Yang, (1990),"Finite element simulation of metal cutting process with strain-rate and temperature effects", Winter Annual Meeting of the American Society of Mechanical Engineers, November 25, 1990 - November 30, 1990, Dallas, TX, USA, Publ by ASME, **43**, 11-24

[157] K. Komvopoulos, and S.A. Erpenbeck. (1991), "Finite element modeling of orthogonal metal cutting", ASME Journal of Engineering for Industry, **113**, 253-267

[158] B. Zhang, and A. Bagchi. (1004), "Finite element simulation of chip formation and compacrison with machining experiment", Journal of engineering for industry, **3**, 289-297

[159] B. Zhang, and A. Bagchi, (1994), "A study of chip separation and its approximation in finite element simulation of continuous chip formation", Materials Issues in Machining - II and the Physicas of Machining Processes - II, Chicago, IL, USA, Winter Annual Meeting of the ASME, 157-174.

[160] A. G. Mamalis,M. Horvath,A. S. Branis, and D. E. Manolakos. (2001), "Finite element simulation of chip formation in orthogonal metal cutting", Journal of Materials Processing Technology, **110**, Compendex, 19-27

[161] Zone-Chin Lin, and Ship-Peng Lo. (1997), "Ultra-precision orthogonal cutting simulation for oxygen-free high-conductivity copper", Journal of Materials Processing Technology, **65**, 1-3, 281-291

[162] C. Hortig, and B. Svendsen. (2007), "Simulation of chip formation during high-speed cutting", Journal of Materials Processing Technology, **186**, 1-3, 66-76

[163] C. R. Liu, and Y. B. Guo. (2000), "Finite element analysis of the effect of sequential cuts and tool-chip friction on residual stresses in a machined layer", Int J Mech Sci, **42**, 6, 1069-1086

[164] X. P. Yang, and C. R. Liu. (2002), "A new stress-based model of friction behavior in machining and its significant impact on residual stresses computed by finite element method", Int J Mech Sci, **44**, 4, 703-723

[165] John T. Carroll, and John S. Strenkowski. (1988), "Finite element models of orthogonal cutting with application to single point diamond turning", Int J Mech Sci, **30**, 12, 899-920

[166] Z. C. Lin, and S. P. Lo. (1998), "A study of deformation of the machined workpiece and tool under different low cutting velocities with an elastic cutting tool", Int J Mech Sci, **40**, 7, 663-681
[167] A. G. Atkins. (2003), "Modelling metal cutting using modern ductile fracture mechanics: quantitative explanations for some longstanding problems", Int J Mech Sci, **45**, 2, 373-396
[168] M.G. Cockroft, and D.J Latham. (1968), "Ductility and the workability of metals", Journal of the institute of metals, **96**, 33-39
[169] E. Ceretti,M. Lucchi, and T. Altan. (1999), "FEM simulation of orthogonal cutting: serrated chip formation", Journal of Materials Processing Technology, **95**, 1-3, 17-26
[170] M. Calamaz,D. Coupard, and F. Girot. (2008), "A new material model for 2D numerical simulation of serrated chip formation when machining titanium alloy Ti-6Al-4V", Int J Mach Tools Manuf, **48**, 3-4, 275-288
[171] Z. C. Lin, and S. Y. Lin. (1992), "Coupled finite element model of thermo-elastic-plastic large deformation for orthogonal cutting", Journal of Engineering Materials and Technology, Transactions of the ASME, **114**, Compendex, 218-226
[172] E. G. Ng,T. I. El-Wardany,M. Dumitrescu, and M. A. Elbestawi. (2002), "Physics-based simulation of high speed machining", Machining Science and Technology, **6**, 3, 301-329
[173] G.R. Johnson, and W.H. Cook. (1985), "Fracture characteristics of three metals subjected to various strains, strain rates, temperatures and pressures.", Engineering Fracture Mechanics, **21**, 1, 31-48
[174] V. Piispanen. (1937), " "Lastunmuodostumisen Teoriaa" (Theory of. Chip Formation)", Teknillinen Aikakauslehti, **27**, 315-322
[175] M.C. Shaw. (2005),"Metal cutting principles". USA, Oxford University Press.
[176] Väinö Piispanen. (1948), "Theory of formation of metal chips", Journal of Applied Physics, **19**, 10, 876-881
[177] M.C. Shaw,N.H. Cook, and I Finnie. (1953), "The shear-angle relationship in metal cutting ", Transactions of ASME, **75**, 273-288
[178] H. El-Hofy. (2007),"Fundamentals of machining processes - conventional and nonconventional processes". Boca Ranton, FL, USA, CRC Press - Taylor & Francis Group.
[179] A. Mallock. (1881), "The action of cutting tools", Poceedings of the Royal Society of London, **33**, 127-139
[180] Frederick Winslow Taylor. (1901),"On the art of cutting metals", 3d ed. New York, USA, The American society of mechanical engineers.
[181] R.F. Recht. (1964), "Catastrophic thermoplastic shear", J Appl Mech-Trans ASME, **86**, 189-193
[182] W.C. Rice, (1961),"The formation of continuous chips in metal cutting", Proc Inst Mech Engrs, London, **114**, 141-174
[183] M.A. Davies, and T.J. Burns. (2001), "Thermomechanical oscillations in material flow during high-speed machining", Philosophical transactions of the royal society of London series A-mathematical physical and engineering, **359**, 1781,

821-846
[184] M.A. Davies,T. Chou, and C.J. Evans. (1996), "On chip morphology, tool wear and cutting mechanics in finish hard turning", Annals of CIRP, **14**, 1, 77-82
[185] R. Kamanduri. (1993), "Machining and grinding: a historical review of the classical papers", Applied Mechanics Review, **46**, 80-132
[186] Agapiou J.S. Stephenson D.A., (1996),"Metal cutting - theory and practice". New York, NY, USA, Marcel Dekker, INC.
[187] R. Komanduri,T. Schroeder,J. Hazra,B. F. von Turkovich, and D. G. Flom, (1982),"On the catastrophic shear instability in high-speed machining of an AISI 4340 steel", Design and Production Engineering Technical Conference, Washington, DC, USA, ASME, ASME, New York, NY, USA
[188] A. Vyas, and M. C. Shaw. (1999), "Mechanics of saw-tooth chip formation in metal cutting", Journal of Manufacturing Science and Engineering-Transactions of the Asme, **121**, 2, 163-172
[189] E. G. Ng, and D. K. Aspinwall. (1999), "Evaluation of cutting force and temperature when turning hardened die steel with AMBORITE AMB90 and DBC50 tooling", Industrial Diamond Review, **59**, Compendex, 183-195+240
[190] M. C. Shaw, and A. Vyas. (1993), "Chip formation in the machining of hardened steel", CIRP Annals - Manufacturing Technology, **42**, Compendex, 29-33
[191] N.H. Cook,L. Finnie, and M. C. Shaw. (1954), "Discontinuous chip formation", Trans ASME, **76**, 153-162
[192] W.B. Palmer. (1967), "Plastic deformation when cutting into an inclined plane", Journal of Mechanical Engineering Sciences, **9**, 1, 1-9
[193] M. Field, and M.E. Merchant. (1949), "Mechanics of formation of the discontinuous chip in metal cutting", Trans ASME, **71**, 421-430
[194] K. Iwata, and K. Ueda. (1977), "Study on micro-machining mechanics based on direct SEM observation-dynamic crack behavior in shear type chip formation", Journal of the Japan Society of Precision Engineering, **43 (8)**, 932-937
[195] R. Komanduri, and R. H. Brown. (1981), "On the mechanics of chip segmentation in machining", Journal of Engineering for Industry-Transactions of the Asme, **103**, 1, 33-51
[196] R.N. Arnold. (1946), "The mechanism of tool vibration in cutting steel", Proceedings of the Institution of Mechanical Engineers (London), **154**, 261-276
[197] R.L. Kegg. (1965), "Cutting dynamics in machine tool chatter contribution to machine tool chatter", Trans ASME Journal of Engineering Industry, **87**, 464-470
[198] V.A. Stewart, and R.H. Brown. (1969), "A study of the metal cutting process under dynamic conditions", Transactions of the Institution of Engineers, Australia: Mechanical Engineering, 51
[199] J. Tlusty, and M Polacek, (1963), "The stability of machine tools against self-excited vibration in machining", Proc of the International Research in Production Engineering Cons, Pittsburgh, PA, USA, **41**, 465-474.
[200] S.A. Tobias, and W. Fishwick. (1958), "The chatter of lathe tools under orthogonal cutting conditions", Trans ASME, **80**, 1078-1088
[201] P.W. Wallace, and C. Andrew. (1965), "Machining forces: Some effects of tool

vibration", Journal of Mechanical Engineering Science, **7**, 152-162
[202] M.C. Shaw, (1967), "Assessment of machinability", Machinability, ISI Special Report 94, The Iorn and Steel Institute, London, UK,
[203] R. Komanduri, and B. F. Von Turkovich. (1981), "New observations on the mechanism of chip formation when machining titanium alloys", Wear, **69**, 179-188
[204] R. Sowerby, and N Chandrasekaran. (1989), "A proposal for the onset of chip segmentation in machining", Materials Science and Engineering, **A119**, 219-229
[205] K. Nakayama, (1957), "A study on the built-up edge", Bulletin of the faculty of engineering, Yokohama National University, **6**, 1-10
[206] "Abaqus 6.9 CAE/Explicit User's Manual". Providence, RI, USA: "Habbit and Sorenson Inc.", (2010)
[207] A. Simoneau. (2007), "The effect of workpiece microstructure on the mechanics of microscale cutting of 1045 steel", Ph.D. Thesis, Mechanical Engineering Department, McMaster University, Hamilton
[208] S.P.F.C Jaspers, and J.H. Dautzenberg. (2002), "Material behaviour in conditions similar to metal cutting: flow stress in the primary shear zone", Journal of Materials Processing Technology, **122**, 322-330
[209] M.R. Vaziri,M. Salimi, and M. Mashayekhi. (2010), "A new calibration method for ductile fracture meodels as chip separation criteria in machining", Simulation Modelling Practice and Theory, **18**, 1286-1296
[210] R.G. Fenton,P.L.B Oxley, and M.I Mech, (1968/68),"Mechanics of orthogonal machining allowing for the effects of strain rate and temperature on tool-chip friction", Proc Instn Mech Engrs, Sage Publications, **183**, 417-438
[211] ASTM Standard E8/E8M, (2009), "Physical testing standards and mechanical testing standards", ASTM International, West Conshohocken, PA, 10.1520/E0008_E0008M-09 www.astm.org